COLLECTIVE PHENOMENA IN STRONGLY CORRELATED FRUSTRATED QUANTUM SYSTEMS

Leonid Isaev

Accepted by the Graduate Faculty, Indiana University, in partial fulfillment of the requirements for the degree of Doctor of Philosophy.

Doctoral Committee

_____

G. Ortiz, Ph.D.

_____

H. Fertig, Ph.D.

_____

W. M. Snow, Ph.D.

_____

P. Sokol, Ph.D.

Date of Oral Examination

June 24, 2011

Acknowledgements

I am indebted to my advisor, Prof. G. Ortiz for his guidance, wisdom and patience, and to C. D. Batista for providing inspiration and continuing support for my research. This work wouldn't be possible without many fruitful and stimulating collaborations with J. Dukelsky, which are much appreciated.

I greately acknowledge countless illuminating discussions with D. Solenov and K. Velizhanin regarding all aspects of physics.

Finally, I am grateful to my committee members, Profs. H. Fertig, P. Sokol and W. M. Snow, for contributing valuable insights to my thesis work.

Leonid Isaev

COLLECTIVE PHENOMENA IN STRONGLY CORRELATED FRUSTRATED

QUANTUM SYSTEMS

We study the role of lattice frustration, competing interactions and quantum fluctuations in stabilizing non-trivial states of matter in strongly correlated systems. Our analysis focuses on three types of physical phenomena: magnetism in Mott insulators, superconductivity in repulsive fermion systems and multiferroicity in complex oxides.

In the context of frustrated magnets, we propose a real-space mean-field framework, which combines exact diagonalization in finite clusters and variational calculation of the state of an infinite system, thus capturing local correlations and providing a controlled and unbiased approximation scheme. This method is applied to several models of quantum magnetism, such as the square-lattice Heisenberg antiferromagnet with competing first and second neighbor exchange interactions. Using a *single* variational ansatz for the ground state, we compute the zero-temperature phase diagram of this model, which includes a quantum paramagnetic state. We show that this state has a correlated plaquette nature and breaks translational invariance, but preserves lattice point-group symmetries. Next, we study the phenomenon of magnetization plateaux in the orthogonal dimer compound $SrCu_2(BO_3)_2$, described by the Shastry-Sutherland model. We demonstrate that plateaux are stabilized in certain spin patterns, satisfying *local* commensurability conditions, which we also derive.

Lattice frustration usually hinders the existence of a long-range order. However, in some cases frustration can be beneficial for stabilizing an ordered state, even in a strongly interacting system. We illustrate this mechanism, by considering the Hubbard model with modulated electron hoppings. Within a controlled approximation, we demonstrate how magnetic fluctuations lead to a d-wave superconducting state for *arbitrarily* strong fermion repulsion. We also discuss the possibility to observe this

phenomenon in cold atom experiments.

Another class of systems, where frustration and quantum fluctuations serve as prerequisites for a complex ordered state, are multiferroics with ferroelectricity due to charge ordering. Using the rare-earth oxide $LuFe_2O_4$ as an example, we present a theory of multiferroic behavior, caused by the lattice frustration and order-from-disorder physics. Using this theory we explicitly demonstrate that the double exchange mechanism leads to a significant coupling between electric and magnetic orders.

_____

G. Ortiz, Ph.D.

_____

W. M. Snow, Ph.D.

_____

H. Fertig, Ph.D.

_____

P. Sokol, Ph.D.

Contents

List of Tables

List of Figures

Chapter 1

Introduction

One of main challenges of modern condensed matter physics is the characterization of strongly correlated quantum matter, where interactions between degrees of freedom, such as individual electrons or localized magnetic moments, is dominant compared to single-particle energy scales, like the bandwidth or single-ion anisotropy. Contrary to their classical counterparts, the ground state in these systems is determined by quantum fluctuations, which are the manifetation of the Heisenberg uncertainty principle. As a result, one is usually confronted with a variety of exotic phases and non-perturbative behavior, which cannot be described in terms of non-interacting entities.

Low-temperature and condensed matter examples include high-T_c superconductors, frustrated magnetic insulators, heavy-fermion materials, complex oxides, liquid helium mixtures, etc. The state of these systems and their response to external probes are determined by an interplay of quantum orders, such as superconductivity, Bose-Einstein condensation and various ferroic orders. As a result rich phase diagrams emerge, comprised of many different states of matter, when a certain control parameter is varied. For instance, it is well-known that high-T_c materials, such as $La_{1-x}Sr_xCuO_4$, are antiferromagnetic at small composition x and superconducting for

$x \sim 0.1$.

Such complex behavior, on the one hand, opens a door for technological applications. For example, high-T_c materials are extensively used in magnetic sensing (SQUIDs), in accelerometer magnets and even in cell phone towers. Multiferroics, characterized by a strong magneto-electric coupling, are usually proposed as a next-generation RAM devices. On the other hand, this complexity challenges our understanding of basic principles of Nature. It is the presence of non-linear couplings and competing quantum orders, what significantly complicates theoretical description of the strongly correlated systems, simply because there is usually no obvious ground state which one could take as a starting point and build an expansion around. In order to advance our theoretical understanding of strongly correlated systems, new non-perturbative methods and simple (yet illustrative) models have to be developed.

These observations serve as a general motivation for our work. In the following chapters we are going to describe our research in several closely related areas, including quantum phase transitions (i.e. phase transitions which occur at zero temperature as a function of some parameters of the Hamiltonian) in frustrated magnetic insulators, superconductivity in strongly repulsive fermionic systems, and mangeto-electric coupling in charge-frustrated multiferroic materials.

The key theoretical concepts of strong correlations, frustration and the quantum order-from-disorder mechanism, which will pervade the work, are summarized in the following sections. We shall also briefly present basic ideas of the theory of superfluidity in a repulsive Fermi gas at $T = 0$. This chapter concludes with a "roadmap" of research directions, which were worked out during the completion of this work, and a summary of results.

1.1 Basic theoretical concepts

1.1.1 Electronic origin of magnetism: Mott physics

In its simplest form the Hubbard model describes a single band of electrons propagating in the crystal and interacting via screened (i.e. short-range) Coulomb forces. It was originally proposed as a minimal model of narrow-band magnetic conductors, where the same electronic degree of freedom is responsible for both charge and spin–related phenomena [1, 2, 3]. Physically this model is relevant for describing transition metals and transition metal oxides, which include magnetic and non-magnetic Mott insulators, as well as high-T_c superconductors. Transition elements occupy several rows in the periodic table and include Cr, Ni, Fe and Cu. Properties of these elements and materials based on them are mainly determined by the electrons living in the $3d$ orbital.

Let us consider a simple crystal having one atom per unit cell and one delocalized electron band. In second quantization, the Hamiltonian which describes a system of electrons moving in this lattice and interacting with each other via Coulomb forces is given by [4]:

$$
H = \int d\boldsymbol{x} \sum_{\sigma} \psi_{\sigma}^{\dagger}(\boldsymbol{x}) \left(\frac{\hat{\boldsymbol{p}}^2}{2m} + V(\boldsymbol{x}) \right) \psi_{\sigma}(\boldsymbol{x}) +
$$
$$
+ \frac{1}{2} \int d\boldsymbol{x}_1 d\boldsymbol{x}_2 \sum_{\sigma_1 \sigma_2} \psi_{\sigma_1}^{\dagger}(\boldsymbol{x}_1) \psi_{\sigma_2}^{\dagger}(\boldsymbol{x}_2) \frac{e^2}{|\boldsymbol{x}_1 - \boldsymbol{x}_2|} \psi_{\sigma_2}(\boldsymbol{x}_2) \psi_{\sigma_1}(\boldsymbol{x}_1), \qquad (1.1)
$$

where $\boldsymbol{p} = -i\nabla$ is the momentum operator, e and m is the electron charge and mass, $\sigma = \uparrow, \downarrow$ is the electron spin projection, $d\boldsymbol{x}$ is the volume element, $V(x)$ is the periodic potential of the crystal lattice, and we also adopt the units $\hbar = 1$. The fermion field operator [4] $\psi_{\sigma}(\boldsymbol{x})$ satisfies the usual anticommutation relation:

$$
\left\{ \psi_{\sigma_1}(\boldsymbol{x}_1), \psi_{\sigma_2}^{\dagger}(\boldsymbol{x}_2) \right\} = \delta_{\sigma_1 \sigma_2} \delta(\boldsymbol{x}_1 - \boldsymbol{x}_2).
$$

An essential property of the $3d$ orbital is its strong localization around the ion core. This fact allows us to treat the dynamics of electrons within the tight-binding approximation [5]. The fermion field operator can be expanded in terms of the lowest energy Wannier orbitals [6]:

$$\psi_\sigma(\boldsymbol{x}) = \sum_i \phi_0(\boldsymbol{x} - \boldsymbol{x}_i)c_{i\sigma},$$

where $\phi_0(\boldsymbol{x} - \boldsymbol{x}_i)$ is the ground-state Wannier function, centered around an atom with coordinate $\boldsymbol{x}_i \equiv i$. Anticommutation relations for the fermion amplitudes $c_{i\sigma}$ follow from those for $\psi_\sigma(\boldsymbol{x})$:

$$\left\{ c_{i\sigma}, c_{j\sigma'}^\dagger \right\} = \delta_{ij}\delta_{\sigma\sigma'}.$$

In terms of the c-operators the original Hamiltonian can be written as:

$$T = -t \sum_{\langle ij \rangle, \sigma} \left(c_{i\sigma}^\dagger c_{j\sigma} + \text{h.c.} \right) + U \sum_i n_{i\uparrow}n_{i\downarrow}. \tag{1.2}$$

Derivation of this expression involves several approximations: (i) The summation in the first term extends only over *nearest-neighbor* links $\langle ij \rangle$ (see panel (a) in Fig. 1.1). This assumption is justified by the localized nature of the Wannier orbitals. The quantity t, called the hopping amplitude, is defined as:

$$t = -\frac{1}{N} \sum_{\boldsymbol{k}} \mathrm{e}^{-\mathrm{i}\boldsymbol{k}(\boldsymbol{x}_i - \boldsymbol{x}_j)}\epsilon_0(\boldsymbol{k}),$$

where N is the number of atoms, the sum goes over the Brillouin zone, and $\epsilon_0(\boldsymbol{k})$ is the dispersion relation in the lowest band. The last equation is easy to obtain, if one recalls the definition of the Wannier functions in terms of the Bloch states $\varphi_{n\boldsymbol{k}}$:

$$\phi_n(\boldsymbol{x} - \boldsymbol{x}_i) = \frac{1}{\sqrt{N}} \sum_{\boldsymbol{k}} \mathrm{e}^{-\mathrm{i}\boldsymbol{k}\boldsymbol{x}_i}\varphi_{n\boldsymbol{k}}(\boldsymbol{x}).$$

(ii) The long-range part of the Coulomb interaction is assumed to be screened [1], so that only the *on-site* repulsion remains. This local interaction is described by the second term in Eq. (1.2), with U being the corresponding interaction strength. Eq. (1.2) is known as the Hubbard model. Its basic physical picture lays in the competition between the local repulsion U, which tends to localize electrons, and the kinetic energy t (quantum fluctuations).

A lot of effort was dedicated to studying this competition in condensed matter [6, 7] and cold atoms [8]. Here we only consider a conceptually important situation, when the on-site Coulomb repulsion U is large compared to the bandwidth t, and the number of electrons equals the number of lattice sites N (the half-filled case; remember that the maximum number of electrons which can be accomodated is $2N$).

In the zeroth approximation the kinetic energy term in (1.2) can be ignored. The resulting classical model has an obvious ground state with one electron per lattice site and 2^N-fold spin degeneracy. Any excited state has at least one doubly occupied site, and is separated by the gap $\Delta E \geqslant U$ from the ground state manifold. The macroscopic ground state degeneracy is partially lifted by quantum fluctuations via the second order ($\sim t^2/U$) processes, shown in panel (b) of Fig. 1.1. This fluctuation channel is open only if in the initial and final states the two electrons have opposite spin projections. When electrons have parallel spins, the doubly occupied intermediate state is prohibited by the Pauli principle.

Using the second-order degenerate perturbation theory, one can show [6] that the low-energy effective Hamiltonian involves only spin degrees of freedom and has the Heisenberg–Dirac form:
$$H_{\text{ef}} = J \sum_{\langle ij \rangle} \left(\boldsymbol{S}_i \boldsymbol{S}_j - \frac{1}{4} \right), \tag{1.3}$$
where $J = 4t^2/U > 0$ is the exchange interaction and $\boldsymbol{S}_i = \frac{1}{2}c_{i\alpha}^{\dagger}\boldsymbol{\sigma}_{\alpha\beta}c_{i\beta}$ are electron
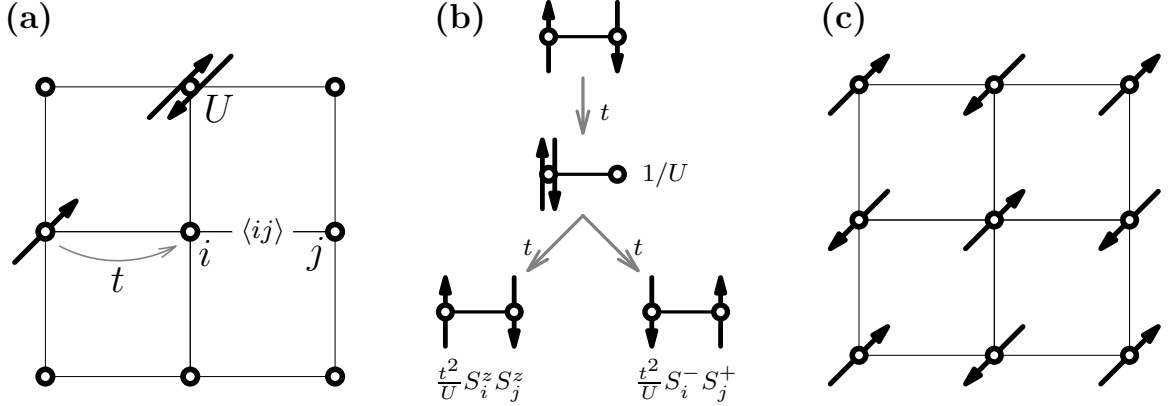
Figure 1.1: (a) Energy scales and site notations in the Hubbard model (1.2). (b) Virtual processes which lead to the Heisenberg model. An initial state (on the top), can transform into itself, leading to the Ising terms $\sim S_i^z Z_j^z$ in (1.3); or have its spins interchanged. The latter process gives the XY terms $S_i^x S_j^x + S_i^y S_j^y = \frac{1}{2}\big(S_i^+ S_j^- + \text{h.c.}\big)$ with $S_i^\pm = S_i^x \pm S_i^y$.

spin-$\frac{1}{2}$ operators with $\boldsymbol{\sigma}_{\alpha\beta}$ being the Pauli matrices [1].

The model of Eq. (1.3), known as the Heisenberg model, represents one of the most fundamental approximations in condensed matter physics. It is usually used to describe magnetic insulators, e.g. undoped high-T_c materials. Note that so far we made no assumptions regarding the lattice on which the Hamiltonians (1.2) and (1.3) are defined. In the simplest case of a square lattice, the Heisenberg model has an *antiferromagnetically* (long-range) ordered Néel ground state [9], shown in panel (c) of Fig. 1.1. However, as we shall discuss in Sec. 1.1.2, the lattice topology has a profound effect on the variety of phases exhibited by the Heisenberg model.

The above discussion demonstrates that low-energy properties of the large-U Hubbard model at half-filling are mainly determined by the spin degree of freedom, at least in non-frustrated lattices[2]. The charge is completely "locked", i.e. there is a gap

---

[1]Recall their canonical form:

$$\sigma^x = \begin{pmatrix} 0 & 1 \\ 1 & 0 \end{pmatrix}; \quad \sigma^y = \begin{pmatrix} 0 & -i \\ i & 0 \end{pmatrix}; \quad \sigma^z = \begin{pmatrix} 1 & 0 \\ 0 & -1 \end{pmatrix}.$$

[2]For peculiar charge effects associated with lattice frustration see [10].

$\sim U$ to charge excitations. Thus, the system is an insulator, not because of a band gap (in fact, according to the usual theory of solids, the system should be metallic), but rather due to electron correlations. Such materials were termed *Mott insulators*, as opposed to non-interacting *band* insulators.

For densities slightly below half-filling the system is a "diluted antiferromagnet", with positively charged holes propagating in the antiferromagnetic background. This background is usually believed to lead to an attractive interaction between holes [11], which is why the two-dimensional Hubbard model is commonly considered a minimal model for high-T_c copper oxides. However, these arguments were later found to be misleading [12]. Thus, the question of whether or not the Hubbard model (1.2) can support a superconducting phase remains open. We shall return to this problem in Chap. 3.

1.1.2 Frustration and the order-from-disorder mechanism

The Hamiltonian of a lattice spin system is usually represented a sum of *local* interaction terms, e.g. links. In general, we say that such system is frustrated, if its ground state (GS) wavefunction does not simultaneously minimize all local spin interactions in the Hamiltonian. A ubiquitous consequence of the frustration is degeneracy of the classical GS of a spin system. Out of this GS manifold, quantum or thermal fluctuations will often select a particular state, which is unique up to trivial degeneracies, associated with global spin or spatial symmetry transformations. This mechanism, called "order-from-disorder", is one of the most fundamental concepts of condensed matter physics.

Examples of non-frustrated systems include the antiferromagnetic (AF) nearest-heighbor (NN) Heisenberg model (1.3), defined on a bipartite lattice, such as square, honeycomb (panel (a) in Fig. 1.2) or simple cubic, and the ferromagnetic Heisenberg model on any lattice. In the first case a Néel–like state always minimizes interaction
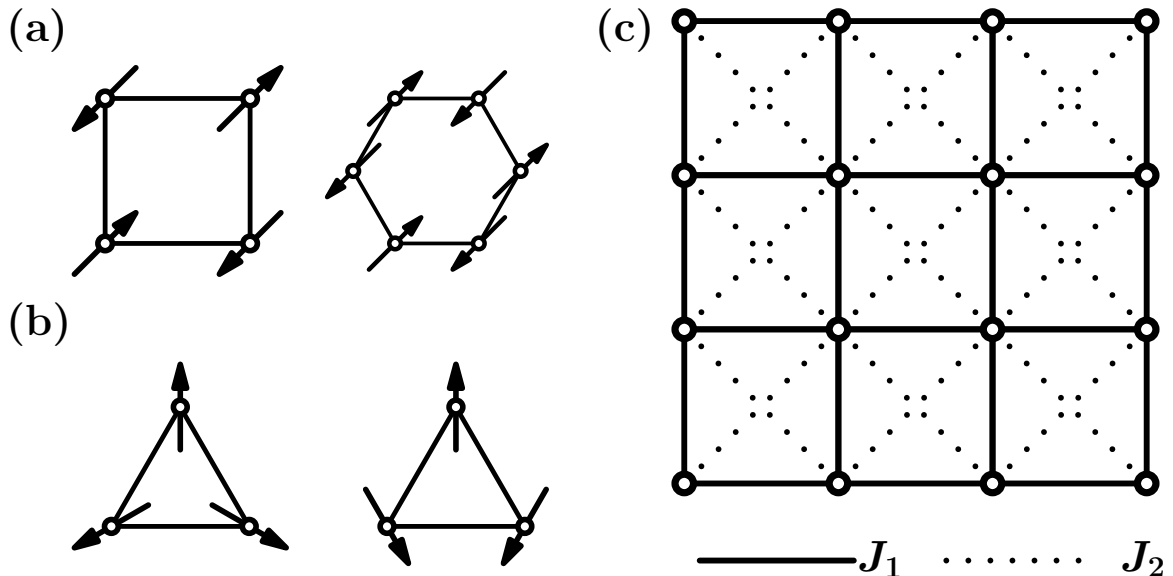
Figure 1.2: Examples of non-frustrated and frustrated lattices. Solid (dotted) lines denote (next-) nearest neighbor antiferromagnetic exchange couplings. (a) Non-frustrated bipartite lattices: square and honeycomb. (b) Two possible 120° classical ground states on a frustrated triangular lattice. (c) Interactions in the square-lattice J_1-J_2 model (1.4).

energy between every pair of spins. In the ferromagnetic case a configuration with all spins parallel is a unique exact GS. On the other hand, if the lattice contains elementary triangles – a situation realized by triangular, FCC and HCP lattices – one can not find a classical spin configuration which satisfies every link in the Heisenberg model. In Fig. 1.2 panel (b) we show two possible 120° GS's of the AF Heisenberg model with NN interactions on a triangular lattice.

Another situation when a spin system can be frustrated is realized if the Hamiltonian involves different kinds of conflicting interactions, and the GS does not correspond to a minimimum of either kind of interaction. A typical example of a magnet with frustrating couplings is the so-called J_1-J_2 model, defined on a square lattice and represented by the Heisenberg Hamiltonian, which in addition to NN AF interactions (J_1) also includes frustrating next-NN AF exchange couplings (J_2), see panel (c) in Fig. 1.2. In the rest of the section, we shall use this model to illustrate the effects of

frustration and the order-from-disorder physics. An interested reader is referred to the review [13] for a detailed discussion.

The J_1-J_2 Hamiltonian has the form:

$$H = J_1 \sum_{\langle i,j \rangle} \boldsymbol{S}_i \boldsymbol{S}_j + J_2 \sum_{\langle\langle i,j \rangle\rangle} \boldsymbol{S}_i \boldsymbol{S}_j, \tag{1.4}$$

where i, $j = 1 \ldots N$ enumerate lattice sites, the symbol $\langle\langle i,j \rangle\rangle$ denotes next-NN links (Fig. 1.2, panel (c)), $J_{1,2} > 0$, and $\boldsymbol{S}_i$ describes the localized spin-1/2 degree of freedom. In order to determine possible classical GS's we follow the method of Luttinger and Tisza [14], which amounts to minimizing the Fourier transform $J(\boldsymbol{k})$ of the exchange interaction as a funtion of $\boldsymbol{k}$. In the momentum representation we have:

$$S_i = \frac{1}{\sqrt{N}} \sum_{\boldsymbol{k}} e^{i\boldsymbol{k}\boldsymbol{x}_i} \boldsymbol{S}_{\boldsymbol{k}}$$

and

$$H = \sum_{\boldsymbol{k}} J(\boldsymbol{k}) |\boldsymbol{S}_{\boldsymbol{k}}|^2,$$

where $\boldsymbol{S}_{-\boldsymbol{k}} = \boldsymbol{S}_{\boldsymbol{k}}^*$, because of the reality of the vector $\boldsymbol{S}_i$. The function $J(\boldsymbol{k})$ is defined as:

$$J(\boldsymbol{k}) = 2\big[J_1\big(\cos k_x + \cos k_y\big) + J_2 \cos k_x \cos k_y\big].$$

Minimization of this function yields the "phase diagram" shown in Fig. 1.3. Depending on the value of J_2/J_1 there exist two distinct phases, separated by a 1st order phase transition (level crossing): (i) For $J_2/J_1 < 1/2$, $J(\boldsymbol{k})$ has a single minimum at $\boldsymbol{k} = (\pi, \pi)$, which corresponds to the usual Néel state. (ii) When $J_2/J_1 > 1/2$, there exist two equivalent degenerate minima at $\boldsymbol{k} = (0, \pi)$ and $\boldsymbol{k} = (\pi, 0)$. In the latter case one has the so-called columnar spin structure, which consists of ferromagnetic lines (columns), arranged antiferromagnetically. We can also visualize this order as two AF sublattices with the unit cell $\sqrt{2} \times \sqrt{2}$, shifted relative to each other by one
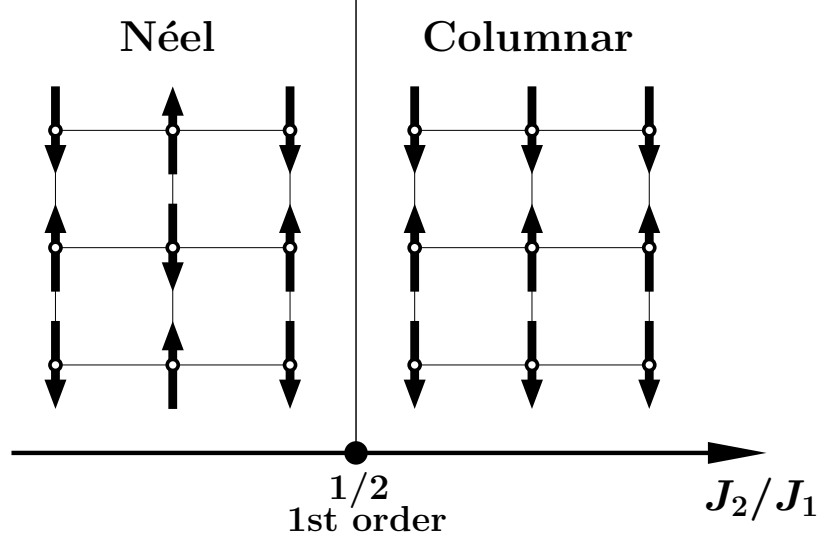
Figure 1.3: Classical phase diagram of the J_1-J_2 model. Arrows indicate spin structure in each phase. The two phases are separated by a first-order (discontinuous) phase transition at $J_2 = J_1/2$.

lattice constant. Classical GS energies per spin in the two phases are given by:

$$\frac{E}{N} = -2S^2 \times \left\{ \begin{array}{ll} J_1 - J_2, & J_2 < J_1/2; \\ J_2, & J_2 > J_1/2, \end{array} \right.$$

where $S = 1/2$ is the length of the classical spin vector. The two branches of $E(J_2/J_1)$ intersect when $J_2 = J_1/2$, which gives the 1st order phase transition point.

In case (i) the GS has only trivial degeneracies, associated with $\pi/4$ rotations and space inversion. Case (ii), however, is much more interesting. We observe that the GS has a *continuous* degeneracy, associated with a relative rotation of the two AF sublattices by a twist angle ϕ, as depicted in the left panel of Fig. 1.4. General arguments [15, 16] indicate that this classical degeneracy is lifted by quantum fluctuations (order-from-disorder), and a collinear (i.e. columnar) order with $\phi = 0$ or π is selected. In order to see this, one has to perform a spin-wave expansion around the classical GS with a particular value of the twist angle, and minimize the quantum zero-point energy as a function of ϕ [17, 18].

The goal is most easily achieved by writing equations of motion for spin operators [19]

$$\dot{\boldsymbol{S}}_i = i\big(H\boldsymbol{S}_i - \boldsymbol{S}_i H\big) = \sum_{a=1,2} J_a\bigg(\sum_{\delta_a}\big[\boldsymbol{S}_{i+\delta_a} \times \boldsymbol{S}_i\big]\bigg),$$

where $\dot{\boldsymbol{S}}_i = d\boldsymbol{S}_i/dt$ and δ_1 (δ_2) denotes four NN (next-NN) positions for a given site i. In the notations of Fig. 1.4, they are given by: $\delta_1 = \{\pm\boldsymbol{e}_x, \pm\boldsymbol{e}_z\}$ and $\delta_2 = \{\pm\boldsymbol{e}_x\pm\boldsymbol{e}_z\}$. Next we separate the fluctuating part of a spin operator by writing

$$\boldsymbol{S}_i = \langle\boldsymbol{S}_i\rangle + \boldsymbol{s}_i,$$

where $\langle\boldsymbol{S}_i\rangle$ is the classical solution,

$$\langle\boldsymbol{S}_i\rangle = \frac{S}{2}\big\{\sin\phi(\cos\pi z_i - \cos\pi x_i)\boldsymbol{e}_x + \big[(1+\cos\phi)\cos\pi z_i + (1-\cos\phi)\cos\pi x_i\big]\boldsymbol{e}_z\big\}.$$

Linearization of equations of motion with respect to $\boldsymbol{s}_i$, yields the magnon dispersion relation:

$$\omega_{\boldsymbol{k}}(\phi) = 4J_2 S\left[\frac{\lambda}{2}\big(\cos k_x + \cos k_z\big) + 1 + \cos k_x \cos k_z\right]^{1/2} \times$$
$$\times \left[\frac{\lambda}{2}\cos\phi\big(\cos k_x - \cos k_z\big) + 1 - \cos k_x \cos k_z\right]^{1/2},$$

where $\lambda = J_1/J_2$. We note that there is only *one* branch in the magnon spectrum, because $\boldsymbol{k}$ belongs to the large Brillouin zone. The zero-point energy is given by the usual expression:

$$E_{\text{fl}}(\phi) = \frac{1}{2}\sum_{\boldsymbol{k}}\omega_{\boldsymbol{k}}(\phi).$$

In the right panel of Fig. 1.4 we plot $\epsilon(\phi) = E_{\text{fl}}(\phi)/2J_2 SN$ for several values of λ, approaching the transition point from inside the columnar phase. We see that $\epsilon(\phi)$ indeed has two minima, at $\phi = 0$ and π, corresponding to the collinear spin alignment with ferromagnetic chains running along x and z axis, respectively.

11
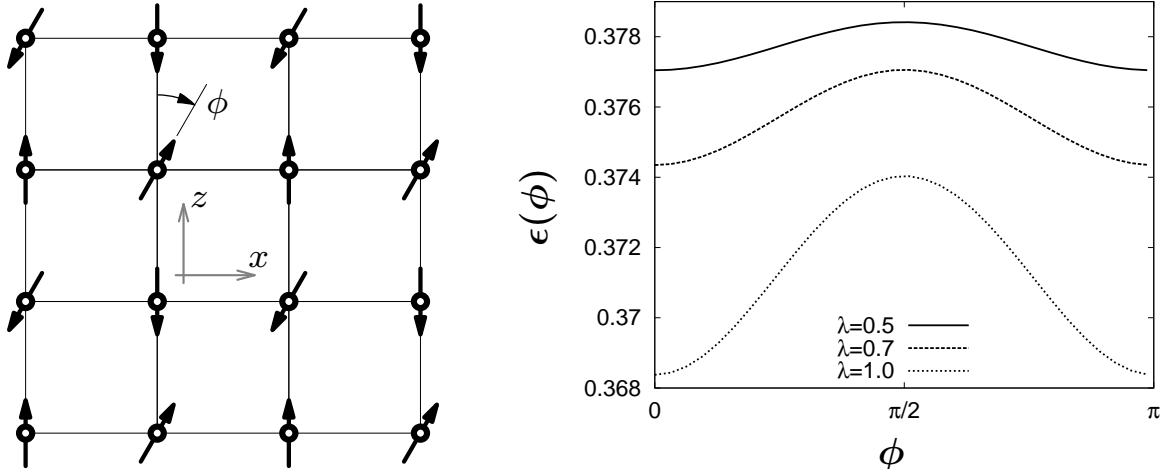
Figure 1.4: Left panel: A classical spin configuration for an arbitrary twist angle ϕ in the columnar phase $J_2 > J_1/2$ of the J_1-J_2 model (1.4). Right panel: Normalized zero-point energy, $\epsilon(\phi) = E_{\text{fl}}(\phi)/2J_2SN$ as a function of the twist angle for several values of the dimensionless coupling $\lambda = J_1/J_2$.

Finally, we note that exactly at the point $J_2 = J_1/2$ the GS is macroscopically degenerate, because the Hamiltonian (1.4) can be rewritten as:

$$H = \text{const.} + \frac{J_1}{2} \sum_{\square} \boldsymbol{S}_{\square}^2,$$

where the sum runs over plaquettes of the square lattice with $\boldsymbol{S}_{\square}$ being the total spin of a plaquette. Thus, the classical energy is minimized, when each plaquette has a vanishing total spin. The classical GS is, therefore, highly degenerate. At this point the spin-wave expansion breaks down [17, 20], which is a strong evidence of existence of a quantum disordered (paramagnetic) phase in this region of the parameter space. We shall consider this question more closely in Chap. 2.

1.1.3 Superconductivity in repulsive fermion systems

The phenomenon of superconductivity (SC), or superfluidity in neutral fermion systems, is usually associated with some kind of an effective attractive interaction between the fermions. For instance, in such "conventional" superconductors as Al, Pb

or Cd, the electron attraction is caused by electron-phonon interaction. Another crucial requirement for SC is the sharpness of the Fermi surface. As shown by Cooper [21], the Fermi sea is unstable against an arbitrarily weak attraction $V \ll \varepsilon_F$ acting between particles at the Fermi surface. It is well known from quantum mechanics that in two dimensions a weak attractive potential always has an exponentially shallow bound state [4]. Similarly, the origin of the Cooper effect is the finite density of states, g_F, at the Fermi level; the bound state energy, also known as the superconducting gap, is given by $\Delta \sim e^{1/Vg_F}$. The ground state of a superconductor is a "condensate" of paired fermions, or Cooper pairs. Superfluidity in He^3 and high-temperature SC present a significant puzzle, since there is no obvious attraction mechanism between the fermions. Thus, superfluidity in *repulsive* Fermi systems is still an actively developed subject in condensed matter physics. In this section we will set up basic notions of the usual Bardeen-Cooper-Schrieffer (BCS) theory of SC [19, 22], and discuss the Kohn-Luttinger mechanism [23] of SC in weakly repulsive systems.

Let us consider a system of fermions of mass m, interacting via some two-body potential $V(\boldsymbol{x}_1 - \boldsymbol{x}_2)$, see Eq. (1.1). The Heisenberg equation of motion for the field operator $\psi_\alpha(t, \boldsymbol{x})$, has the form [19]:

$$\mathrm{i}\frac{\partial \psi_\alpha(t, \boldsymbol{x})}{\partial t} = \left(\frac{\hat{\boldsymbol{p}}^2}{2m} - \mu\right)\psi_\alpha(t, \boldsymbol{x}) + \int d\boldsymbol{y} V(\boldsymbol{x} - \boldsymbol{y})\psi_\beta^\dagger(t, \boldsymbol{y})\psi_\beta(t, \boldsymbol{y})\psi_\alpha(t, \boldsymbol{x}),$$

where μ is the chemical potential, and we assume summation over doubly repeated spin indices α, β, etc. At zero temperature μ is just the Fermi energy ε_F, and we shall use the notations

$$\xi_p = p^2/2m - \mu \approx v_F(p - p_F); \quad g_F = mp_F/\pi^2,$$

where p_F is the Fermi momentum, $v_F = p_F/m$, and g_F is the density of state at the Fermi level mentioned above.

Next we define the single-particle time-ordered Green's function [19]:

$$G_{\alpha\beta}(t_1\boldsymbol{x}_1, t_2\boldsymbol{x}_2) = -\mathrm{i}\langle T\psi_\alpha(t, \boldsymbol{x}_1)\psi_\beta^\dagger(t_2, \boldsymbol{x}_2)\rangle =$$
$$= -\mathrm{i}\big[\theta(t_1 - t_2)\langle\psi_\alpha(t_1, \boldsymbol{x}_1)\psi_\beta^\dagger(t_2, \boldsymbol{x}_2)\rangle - \theta(t_2 - t_1)\langle\psi_\beta^\dagger(t_2, \boldsymbol{x}_2)\psi_\alpha(t_1, \boldsymbol{x}_1)\rangle\big],$$

where the average is taken in the ground state, and $\theta(x)$ is the Heaviside step function: $\theta(x) = 1$ if $x \geqslant 0$ and $\theta(x) = 0$ if $x < 0$. This correlator allows us to compute single-particle observables for a normal system. In order to describe properties of a superconductor, one has to introduce the anomalous (Gorkov's) Green function:

$$F_{\alpha\beta}(t_1\boldsymbol{x}_1, t_2\boldsymbol{x}_2) = -\mathrm{i}\langle T\psi_\alpha(t, \boldsymbol{x}_1)\psi_\beta(t_2, \boldsymbol{x}_2)\rangle$$

and its conjugate $F_{\alpha\beta}^\dagger$. These expectation values are defined only in the thermodynamic limit, because they violate particle number conservation. It is breaking of this $U(1)$ symmetry which distinguishes the superconducting state from the normal phase.

Equations of motion for G and $F^\dagger$ follow from those for ψ and $\psi^\dagger$:

$$\left(\mathrm{i}\frac{\partial}{\partial t} - \frac{\hat{\boldsymbol{p}}}{2m} + \mu\right)G_{\alpha\beta}(x - x') = \delta_{\alpha\beta}\delta(x - x') +$$
$$+ \mathrm{i}\int d\boldsymbol{y}V(\boldsymbol{x} - \boldsymbol{y})\langle T\psi_\alpha(x)\psi_\gamma(y)\psi_\gamma^\dagger(y)\psi_\beta^\dagger(x')\rangle;$$
$$\left(\mathrm{i}\frac{\partial}{\partial t} + \frac{\hat{\boldsymbol{p}}}{2m} - \mu\right)F_{\alpha\beta}^\dagger(x - x') =$$
$$= \mathrm{i}\int d\boldsymbol{y}V(\boldsymbol{x} - \boldsymbol{y})\langle T\psi_\alpha^\dagger(x)\psi_\gamma^\dagger(y)\psi_\gamma(y)\psi_\beta^\dagger(x')\rangle,$$

where we used the notations $x = (t, \boldsymbol{x})$, $y = (t, \boldsymbol{y})$ and the fact that in a translationally invariant system all averages depend only on the difference $x - y$, but not on x and y separately. The essence of the BCS approximation is a mean-field decoupling[3] of the

---

[3]If there is a product of two operators A and B, then the mean-field approximation will amount to writing
$$AB = \langle A\rangle\langle B\rangle + \langle A\rangle B + \langle B\rangle A + \big(A - \langle A\rangle\big)\big(B - \langle B\rangle\big)$$

quartic averages in these equations. Neglecting the usual Hartree and Fock terms, which only modify the value of μ, we have [19]:

$$\left\langle T\psi_\alpha(x)\psi_\gamma(y)\psi_\gamma^\dagger(y)\psi_\beta^\dagger(x')\right\rangle \to \left\langle T\psi_\alpha(x)\psi_\gamma(y)\right\rangle\left\langle T\psi_\gamma^\dagger(y)\psi_\beta^\dagger(x')\right\rangle =$$

$$= -F_{\alpha\gamma}(x-y)F_{\gamma\beta}^\dagger(y-x');$$

$$\left\langle T\psi_\alpha^\dagger(x)\psi_\gamma^\dagger(y)\psi_\gamma(y)\psi_\beta^\dagger(x')\right\rangle \to \left\langle T\psi_\gamma(y)\psi_\beta^\dagger(x')\right\rangle\left\langle T\psi_\alpha^\dagger(x)\psi_\gamma^\dagger(y)\right\rangle =$$

$$= -G_{\gamma\beta}(y-x')F_{\alpha\gamma}^\dagger(x-y).$$

The equations of motion linearized in this way are most conveniently written in momentum space[4]:

$$\left(\omega - \xi_p\right)G_{\alpha\beta}(\omega,\boldsymbol{p}) + \Delta_{\alpha\gamma}(\boldsymbol{p})F_{\gamma\beta}^\dagger(\omega,\boldsymbol{p}) = \delta_{\alpha\beta};$$

$$\Delta_{\alpha\gamma}^\dagger(\boldsymbol{p})G_{\gamma\beta}(\omega,\boldsymbol{p}) + \left(\omega + \xi_p\right)F_{\alpha\beta}^\dagger(\omega,\boldsymbol{p}) = 0.$$

Here we introduced the BCS gap function:

$$\Delta_{\alpha\beta}(\boldsymbol{p}) = i\int \frac{d\omega d\boldsymbol{q}}{(2\pi)^4}V(\boldsymbol{p}-\boldsymbol{q})F_{\alpha\beta}(\omega,\boldsymbol{q}),$$

which plays a central role in the entire SC theory. This function satisfies the self-consistent BCS equation [22]:

$$\Delta_{\alpha\beta}(\boldsymbol{p}) = -\int \frac{d\boldsymbol{q}}{(2\pi)^4}V(\boldsymbol{p}-\boldsymbol{q})\frac{\Delta_{\alpha\beta}(\boldsymbol{q})}{2E(\boldsymbol{q})},$$

---

and neglecting the terms in parentheses. For correlation functions this approximation implies that $\langle AB\rangle \to \langle A\rangle\langle B\rangle$.

[4]We define the Fourier transform of a function $D(x)$ as

$$D(x) = \int \frac{d\omega d\boldsymbol{q}}{(2\pi)^4}e^{-i\omega t + i\boldsymbol{q}\boldsymbol{x}}D(\omega,\boldsymbol{q}).$$

where the quantity

$$E(\boldsymbol{p}) = \sqrt{\xi_p^2 + |\Delta_{\boldsymbol{p}}|^2}; \ \text{with} \ |\Delta_{\boldsymbol{p}}|^2 = \frac{1}{2}\text{Tr}\Delta^\dagger(\boldsymbol{p})\Delta(\boldsymbol{p})$$

gives the spectrum of single-particle excitations.

The tensor structure of $\Delta_{\alpha\beta}$ depends on the total spin S of the Cooper pair [24]. For example, for $S = 0$: $\Delta_{\alpha\beta}(\boldsymbol{k}) = \Delta(\boldsymbol{k})i\sigma^y_{\alpha\beta}$. Since the the Cooper pair wavefunction must be antisymmetric under the interchange of the electrons, spin singlet states correspond to pairing with an even angular momentum l, e.g. s-wave, d-wave, etc, and spin triplets (states with $S = 1$) can only have an odd l-value: p, f, ... Below we only consider the case of the singlet pairing, for simplicity.

Due to the isotropy of space the Fermi surface is a sphere. Since the relevant physics takes place in the vicinity of the Fermi level, we can assume that $\boldsymbol{p} = p_F\boldsymbol{n}$ with $\boldsymbol{n} = (\sin\theta\cos\phi, \sin\theta\sin\phi, \cos\theta)$. All quantities depend only on angular variables, and can be expanded in spherical harmonics:

$$\Delta(\boldsymbol{p}) = \sum_{lm}\Delta_{lm}Y_{lm}(\boldsymbol{n}); \quad V(\boldsymbol{p} - \boldsymbol{q}) = \sum_{lm}V_lY^*_{lm}(\boldsymbol{n}_p)Y_{lm}(\boldsymbol{n}_q).$$

Because of exponential smallness of Δ compared to V, one can neglect the coupling of Δ_{lm} with different l in the BCS equation [25]. The BCS equation itself can now be rewritten as:

$$1 = -V_l g_F \int_0^{\omega_c} d\xi \oint d\boldsymbol{n} \frac{|Y(\boldsymbol{n})|^2}{\sqrt{\xi^2 + \Delta_{lm}^2|Y(\boldsymbol{n})|^2}},$$

where ω_c is some ultraviolet cutoff and $d\boldsymbol{n} = d\Omega/4\pi$ denotes integration over the solid angles. The above equation has non-trivial solution $\Delta_{lm} \sim \omega_c e^{2/V_l g_F}$, corresponding to pairing in a particular l-channel, only if $V_l < 0$.

So far V denoted the bare electron interaction. However, as Kohn and Luttinger pointed out [23], it should actually be replaced by the *dressed* potential, K, which

16

includes many-body renormalization corrections. They were able to demonstrate that in the perturbative regime, when second-order corrections $\sim V^2$ are taken into account, K_l becomes negative for sufficiently large l, i.e. $K_l \sim -1/l^4$, regardless of the form of V. Thus, any weakly coupled repulsive fermion system should become superconducting at sufficiently low temperature. This claim is usually known as the Kohn-Luttinger theorem. Similar ideas were applied in [26] to the small-U Hubbard model. In Chap. 3 we shall return to this problem, but in the context of the *strongly repulsive* Hubbard model.

1.1.4 Multiferroics and magneto-electric coupling

In this section we shall introduce basic concepts in the field of multiferroics and magneto-electric phenomena. For a more detailed review an interested reader is referred to the works [27, 28, 29].

Multiferroics are materials which exhibit several *coexisting* ferroic (hence the name) orderings, e.g. ferroelectric, ferromagnetic, ferrotoroidic, and even ferroelastic. Although there seems to be no precise classification of these materials, it is customary to crudely divide them into two classes, depending on the origin of ferroelectricity. In type-1 compounds the ferroelectric and magnetic orders emerge due to different and largerly independent mechanisms. A classical example is the perovskite $BiFeO_3$, where ferroelectricity happens because of the displacement of Bi ions, while magnetism comes from the partially filled d-shell of Fe. The two orders are coupled through striction effects, which means that this coupling is relatively weak. In type-2 multiferroics, the ferroelectricity is caused by magnetism and exists only in a magnetic phase. This implies a much stronger magneto-electric coupling. Perhaps the most known representative of this group is the spin-spiral multiferroic $TbMnO_3$.

There exists a special "subgroup" of type-1 multiferroic materials in which ferroelectricity is caused by the charge ordering. Examples include the famous mag-
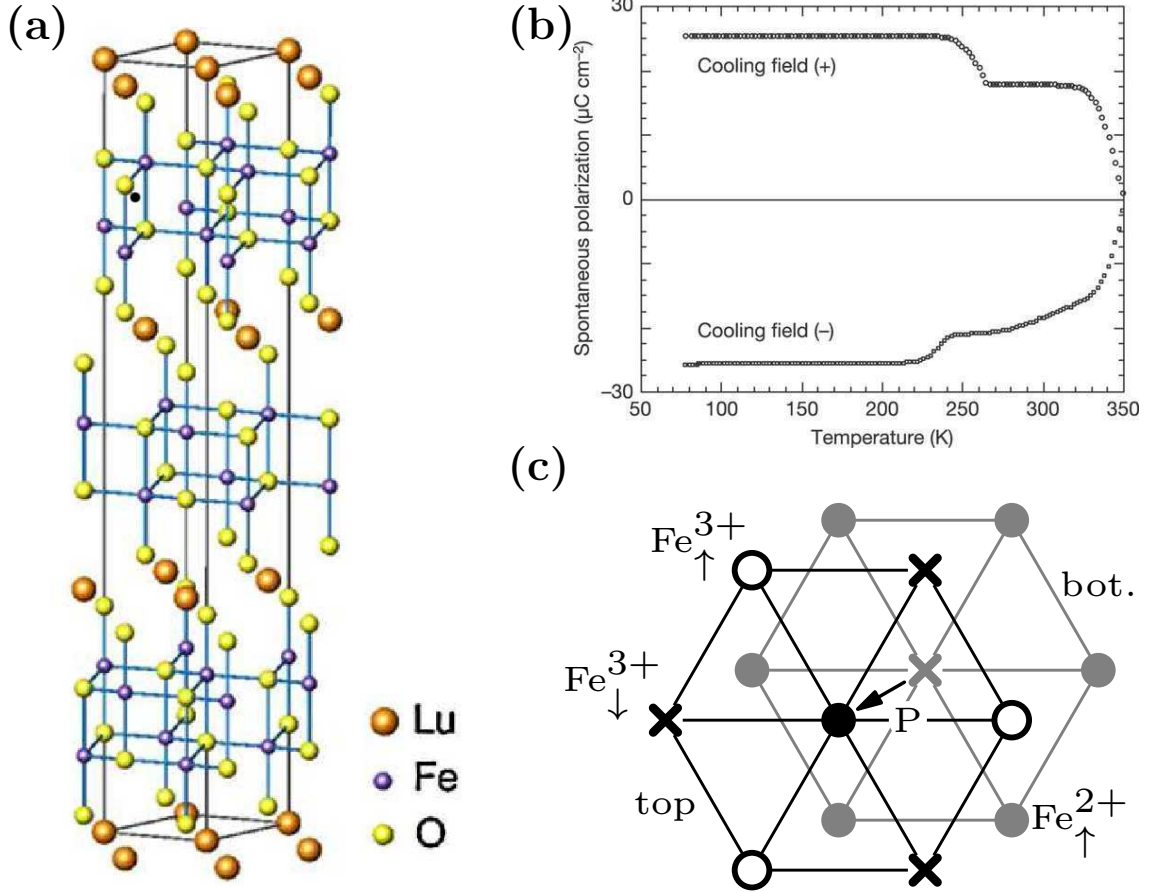
Figure 1.5: (a) Unit cell of $LuFe_2O_4$, which includes three FeO triangular double layers, separated by Lu atoms. (b) Temperature dependence of the electric polarization in $LuFe_2O_4$ (taken from [31]). (c) Ground state of a single FeO double layer. Black (gray) symbols correspond to the top (bottom) single layer. Filled and open circles, and crosses denote iron ions: Fe^{2+} with spin projection $S_z = +2$, Fe^{3+} with $S_z = +5/2$ and Fe^{3+} with $S_z = -5/2$, respectively.

netite Fe_3O_4, perovskite manganites $(PrCa)MnO_3$, and the charge-frustrated compound $LuFe_2O_4$ [30, 31]. Below we give a brief overview of this material, for future reference.

The lattice of $LuFe_2O_4$ is shown in Fig. 1.5(a). It consists of iron-oxygen triangular double layers (TLL). At high temperature the average valence of iron is $Fe^{2.5+}$, with an equal number of Fe^{2+} and Fe^{3+} ions[5]. Below $T_0 \approx 500\,K$ the system exhibits a two-dimensional charge-density wave (CDW) order within each layer. At $T_{CO} \approx 330\,K$

---

[5]Their electronic configurations are $[Ar]3d^54s^0$ and $[Ar]3d^64s^0$, respectively.

a three-dimensional charge-ordering occurs. Because of the frustrated nature of the triangular lattice, a charge redistribution between layers takes place, so that each layer within a TLL has a 1:2 (or 2:1) ratio of Fe^{2+} and Fe^{3+}. This redistribution "relieves" frustration and a layer can have a charge ordering, with two sublattices occupied by ions of one kind and the third one – with ions of the second kind. As a result, the TLL develops an electric polarization, whose temperature dependence is shown in Fig. 1.5(b).

Below $T_N \approx 250\,K$ a ferrimagnetic order sets in and $LuFe_2O_4$ becomes multiferroic. In Fig. 1.5(c) we show one possible ground state, characterized by the coexistence of CDW and magnetic orders. Each Fe^{3+} ion carries a core spin $S = 5/2$, while Fe^{2+} has spin $S = 2$. The Fe^{3+} spins order antiferromagnetically in the honeycomb sublattice, while Fe^{2+} spins are aligned ferromagnetically. The spin structure is collinear because of the easy-axis anisotropy associated with spin-orbit interaction in iron. As we already mentioned, Fe^{2+} has one extra $3d$ electron which can propagate. In the charge-ordered state (but above T_N) this band is still itinerant, thus "dissolving" the CDW. However, below the magnetic transition these hopping processes are strongly suppressed due to the Hund coupling [4], favoring the CDW order and further enhancing the electric polarization within a TLL. This simple physical mechanism is believed to be responsible for the anomaly found in pyroelectric current measurements around T_N (see Fig. 1.5(b)) [31]. In Chap. 4 we shall investigate this frustration-driven mechanism of multiferroicity in more detail.

The interest in multiferroics is not purely fundamental but is also stimulated by promising technological applications of these materials, e.g. as low-power memory and storage devices. These applications would be realistic if the material exibits a sizeable coupling between its ferroic orders, allowing the manipulation of magnetization with an external electric field (voltage). In principle, any material should exhibit some magneto-electric coupling, possibly due to non-linear effects. For applications the so-

called linear magneto-electric effect is of primary interest. At the phenomenological level this effect is described by a correction to the Gibbs thermodynamic potential of the form [32]:

$$\Delta\Phi_{ME} = -\alpha_{ij}E_iH_j,$$

where α_{ij} is the (non-symmetric) magnetoelectric tensor. In the zero-field regime the magnetization (electric polarization) is proportional to the applied electric (magnetic) field: $M_i = \alpha_{ij}E_j$ and $P_i = \alpha_{ij}H_j$. Since $\boldsymbol{E}$ is a polar and $\boldsymbol{H}$ is an axial vector, $\alpha_{ij} \neq 0$ only in non-centrosymmetric crystals. Also, α_{ij} vanishes in systems without broken time-reversal invariance.

1.2   Roadmap

The general agenda of this thesis is the study of physical phenomena driven by frustration and strong correlations. Our research focused on three major directions, each described below in a respective chapter:

- Low-dimensional magnetic insulators (Chap. 2)

  Our interest in this field is both fundamental and methodological. First, in Sec. 2.2 we develop a real-space mean-field framework, aimed at computing ground state properties of frustrated systems. This method combines exact diagonalization of finite clusters and variational calculation of the state of an infinite system, thus capturing local quantum correlations, and providing a controlled and unbiased approximation scheme. We apply this approach to several important models of quantum magnetism. Sec. 2.2 is devoted to investigation of the non-magnetic phase of the J_1-J_2 model. In Sec. 2.3 we formulate a local physical mechanism behind the phenomenon of magnetization plateaux in orthogonal dimer compounds such as $\mathrm{SrCu_2(BO_3)_2}$, mathematically described by the Shastry-Sutherland model. Finally in Sec. 2.4 we compute and characterize

the phase diagram of a non-frustrated Heisenberg magnet with biquadratic spin interactions.

- Superconductivity in strongly repulsive fermions (Chap. 3)

  Here we study the effects of lattice inhomogeneities and frustrating hoppings beyond nearest neighbors on superconductivity in fermion systems with repulsive short-ranged interactions, such as the Hubbard model. We show that under certain conditions, the above features can lead to a macroscopic ground state degeneracy which allows magnetic fluctuations to stabilize the superconducting state for arbitrarily strong fermion repulsion. We also discuss the possibility to observe this phenomenon in experiments using cold fermionic atoms, e.g. ^{40}K, in specially prepared optical lattices.

- Magneto-electric coupling due to order-from-disorder (Chap. 4)

  In this last chapter we study magneto-electric phenomena in charge-ordered multiferroic materials. Using the rare-earth oxide $LuFe_2O_4$ as a prototype, we construct a minimal effective model which includes lattice frustration, unscreened Coulomb and superexchange interactions, and spin-orbit effects. We investigate its phase diagram and demonstrate how the order-from-disorder physics leads to a ferroelectric charge ordering. Emergence of the ferrimagnetism results in an enhancement of the electric polarization, in a qualitative agreements with experiments in $LuFe_2O_4$. The electric and magnetic orders are coupled by the double-exchange mechanism. This coupling manifests itself in a finite value of the magneto-electric coefficient, which is strongly enhanced around the ferrimagnetic transition temperature.

Chapter 2

Low-dimensional frustrated magnets

Our study of frustrated magnets has both methodological and fundamental goals. The key achievments of this chapter can be summarized as follows:

- We develop the hierachical mean-field method – a non-perturbative technique for computing ground-state properties of the system;

- Using this approach we obtain the phase diagram of the J_1-J_2 model, and characterize its quantum paramagnetic phase;

- We propose a physical mechanism, leading to magnetization plateaux in the orthogonal dimer compound $SrCu_2(BO_3)_2$, described by the Shastry-Sutherland model.

2.1 General remarks

A usual method for dealing with quantum spin systems consists of identifying a particular classical ground state (GS) and building a fluctuation expansion[1] around it [19]. Provided the true GS of the system is not "too far" from this classical one, the above approach yields GS properties and the spectrum of low-lying excitations. However, when applied to frustrated magnets, this programme faces a serious difficulty. Indeed, as we saw in Sec. 1.1.2, lattice frustration or conflicting interaction lead to the classical GS degeneracy, often macroscopic. Quantum fluctuations now play a prominent role of selecting a particular GS out of several competing phases. In the usual sense, the notion of a phase is directly related to the concept of an order parameter (OP) – an expectation value of some local operator – as a unique characteristic of that phase, e.g. magnetization of the magnetic sample. The existence of an OP implies a certain mean-field description of the problem. Clearly, competition between different phases makes the formulation of this mean-field approximation quite challenging, simply because one has to guess the "right" OP. A consistent approach to studying such systems with competing orders should, therefore, be able to capture this interplay and consider various possible phases in an unbiased fashion.

In the present chapter we discuss one such mean-field framework, whose central ingredient is the notion of a *hierarchical language* (HL) of operators [33] – an operator basis of the fundamental representation of the highest-dimensional local algebra. For instance, in the case of two spin-1/2 operators (4 states), the HL is realized by the generators of $su(4)$. In terms of the HL generators, any local observable can be represented as a linear, and the Hamiltonian of the system – as a quadratic form. Thus, the HL provides a natural starting point for an unbiased mean-field approximation – the hierachical mean-field (HMF) theory.

Of course, an implementation of this approximation scheme depends on the prob-

---

[1]Also known as the spin-wave theory, or random-phase approximation.

lem at hand. Since this chapter studies models, formulated in terms of localized spins, we choose to implement the HMF approach in real space. In this regard, it is similar to other cluster mean-field methods, such as the dynamical mean-field theory (DMFT) [34]. The lattice is divided in spin clusters, the cluster Hamiltonian is diagonalized exactly, and the inter-cluster terms are treated approximately. Contrary to DMFT-like approaches, which handle the inter-cluster interaction perturbatively, we formulate the HMF approximation as a *variational* (relative to the energy) theory, which is much better suited for studying originally translationally invariant systems.

This chapter is organized as follows. Sec. 2.2 introduces the HMF method, using as an example the J_1-J_2 model [35] already discussed in Sec. 1.1.2. This method is then applied in Sec. 2.3 to unveil the physical mechanism responsible for the emergence of magnetization plateaux in the Shastry-Sutherland model [36]. Another application of the HMF approach to a non-frustrated Heisenberg planar antiferromagnet with four-spin ring exchange interactions [37, 38] is presented in Sec. 2.4.

2.2 Hierarchical mean-field approach to the square lattice J_1-J_2 Heisenberg model

In this section we develop the HMF approach by computing the quantum phase diagram and excitation spectrum of the frustrated J_1-J_2 spin-1/2 Heisenberg model. In particular, we show how a single variational ansatz for the GS wavefunction allows one to obtain the *entire* phase diagram of the system. Our results support the existence of a quantum paramagnetic phase around $J_2/J_1 = 1/2$ (see the end of Sec. 1.1.2) and indicate that its structure is a *plaquette crystal*. We also introduce fluctuations around the HMF solution, and demonstrate that in the paramagnetic phase the ground and first excited states are separated by a finite gap, which closes in the ordered Néel and columnar phases.

2.2.1 Introduction

Despite numerous analytical and numerical efforts, the J_1-J_2 model, which exhibits a two sublattice Néel AF, quantum paramagnetic and a four sublattice columnar AF states, continues to attract a lot of attention (for a review of recent achievements, see [13]). While existence of the Néel-ordered phase at small frustration ratio J_2/J_1 and of the columnar AF state at large J_2/J_1 is widely established, properties of the intermediate non-magnetic phase, which occurs around the maximum frustration point $J_2 = J_1/2$, are still under debate. In particular, the correlated nature of the intermediate state and the kind of quantum phase transition separating it from the Néel state is unclear. Various methods have been applied recently to characterize the quantum paramagnetic phase, such as Green's function Monte Carlo [39, 40, 41], coupled cluster methods [42], series expansions [43] and field-theoretical methods [44, 45, 46]. As a result several possible candidate ground states were proposed, namely: a spin liquid [40] preserving translational and rotational symmetries of the lattice as well as various lattice symmetry breaking phases, out of which the dimer phase [45, 47], and the *plaquette resonating valence bond* phase [39] are worth mentioning.

Not surprisingly, the nature of the quantum phase transition separating the Néel-ordered and quantum paramagnetic phases is also under scrutiny. The most dramatic, and at the same time original, scenario [48] is believed to violate the Ginzburg-Landau paradigm of phase transitions [49], which revolves around the concept of an order parameter. Such point of view is based on the observation that there are different spontaneously broken symmetries in the Néel and quantum paramagnetic phases, which thus cannot be connected by a group-subgroup relation. The former, of course, breaks the $SU(2)$ invariance of the Hamiltonian and lattice translational symmetry T^2 [50], but preserves the four-fold rotational symmetry of the square C_4. On the

---

[2]That the translational symmetry is broken in the Néel phase is easy to see, if one *assumes* broken spin $SU(2)$ symmetry. Then, due to the principle of weakening of correlations, the staggered

other hand, the paramagnetic phase is known to restore the spin-rotational symmetry and is believed to break T and C_4, due to spontaneous formation of dimers along the links of the lattice [47, 45]. It follows that these two phases cannot be joined by the usual Landau second-order critical point. This phase transition can either be of the first-order [51] (the latest coupled cluster calculations [42], however, seem to rule out this possibility), or may represent an example of a second order critical point, which cannot be described in terms of a bulk order parameter, but rather in terms of emergent fractional excitations (spinons), which become deconfined right at the critical point [48].

Evidence regarding the structure of the non-magnetic phase is quite controversial. The results of spin-wave calculations [45], large-N expansions [47], and calculations using the density matrix renormalization group combined with Monte-Carlo simulations [41] are believed to indicate the emergence of a dimer order. On the other hand, Monte-Carlo [39] and coupled cluster calculations [42], and analytical results [44] seem to support the presence of C_4 symmetry (plaquette-type ordering) in the paramagnetic phase. In the absence of a reliable numerical or analytical proof of existence of any particular order in the non-magnetic region, there is no apparent reason to believe in the exotic deconfined quantum criticality scenario. Although there apparently exists numerical evidence [52], at the moment of writing we are unaware of a local Hamiltonian in space dimensions larger than one rigorously proven to exhibit the type of quantum critical point discussed in [48]. It was demonstrated in [53] that a two-dimensional lattice model can possess a *first order* quantum critical point, which exhibits deconfined excitations.

In the present section we construct the HMF approximation to systematically in-

---

correlation function satisfies:

$$\lim_{|i-j|\to\infty} (-1)^{i-j} \langle S_i^z S_j^z \rangle = (-1)^{i-j} \langle S_i^z \rangle \langle S_j^z \rangle,$$

which can be constant only if $\langle S_i^z \rangle$ depends on i.

vestigate properties of the various phases displayed by the J_1-J_2 model. The crux of our method is identification of a *plaquette* (spin cluster 2×2 or even larger 4×4 (*super-plaquette*) symmetry-preserving cluster) as the relevant elementary degree of freedom, which captures necessary quantum correlations to represent essential features of the phase diagram. The importance of this degree of freedom was realized only recently in the present context [44], and somewhat earlier in connection with $SU(4)$ spin-orbital [54], and Hubbard [55] models. Besides being variational, our formalism has the attractive feature of preserving fundamental lattice point symmetries and the $SU(2)$ symmetry of the Hamiltonian. Remarkably, such simple mean-field calculation already yields all known results concerning the phase diagram of the J_1-J_2 model, with a good accuracy, namely: existence of a Néel-ordered phase with antiferromagnetic wavevector (π, π) and spin-wave type excitations for $J_2/J_1 \lesssim 0.42$, a non-magnetic intermediate gapped phase, separated by a second-order quantum phase transition, and a first-order transition point, which is characterized by the discontinuous disappearance of the energy gap and connects the paramagnetic state with the columnar antiferromagnetic phase at $(\pi, 0)$ and $(0, \pi)$ for $J_2/J_1 \gtrsim 0.66$.

We emphasize that our investigation primarily focuses on the symmetry analysis of the various phases. Out of many possible coarse graining scenarios, such as covering of the 2D lattice with plaquettes, dimers and crosses, only the C_4-*symmetry preserving* plaquette (or superplaquette) covering (which reproduces the original Bravais lattice) displays the correct phase diagram. In particular, the intermediate paramagnetic phase is shown to be a *plaquette crystal*, which preserves spin and lattice rotational symmetries. For all other scenarios, including dimerized (bond-ordered) phases, we were unable to reproduce all known quantum phase transition points of the model. The HMF coarse graining procedure leads to an explicit breaking of a particular translational symmetry. As a result, one cannot draw rigorous conclusions on the order of the phase transitions based solely on a fixed coarse graining. Nevertheless,

it is still possible to make some predictions using a finite-size scaling of the relevant degree of freedom towards the thermodynamic limit, where the effects associated with coarse graining should disappear.

Our main conclusions are summarized in panel (a) in Fig. 2.1, which also emphasizes symmetry relations between different phases of the model.

2.2.2 The plaquette degree of freedom

The J_1-J_2 model was defined in Eq. (1.4):

$$H = J_1 \sum_{\langle i,j \rangle} \boldsymbol{S}_i \boldsymbol{S}_j + J_2 \sum_{\langle\langle i,j \rangle\rangle} \boldsymbol{S}_i \boldsymbol{S}_j.$$

As mentioned above, we choose the plaquette – any square in Fig. 1.2(c) – as our *elementary* degree of freedom. Then, assuming that the number of sites N is chosen appropriately, the entire lattice can be covered with such plaquettes in a sub-exponentially [54] ($\sim 2^{\sqrt{N}}$) large number of ways.

To illustrate the main idea of the method, we consider in detail only the symmetric covering of the lattice with 2×2 plaquettes, which preserves the C_4 lattice symmetry, see panel (b) in Fig. 2.1, although later the displaced covering (Fig. 2.2, left panel), which breaks C_4 down to C_2 (two-fold symmetry axis), and the case of larger plaquettes (superplaquettes, see Appendix A and Fig. 2.12) will be analyzed as well.

It is convenient to take as a basis the states $|a\rangle = |l_1 l_2 LM\rangle$, where $\boldsymbol{l}_1 = \boldsymbol{S}_1 + \boldsymbol{S}_4$ and $\boldsymbol{l}_2 = \boldsymbol{S}_2 + \boldsymbol{S}_3$ are total spins of the plaquette diagonals (see the legend in Fig. 2.1(b) for site numbering), while $\boldsymbol{L} = \boldsymbol{l}_1 + \boldsymbol{l}_2$ is the total spin of the entire plaquette and M is its z-component. This basis is a natural one and allows us to explicitly label states with corresponding representations of $SU(2)$. The states $\{|a\rangle\}$ are eigenstates
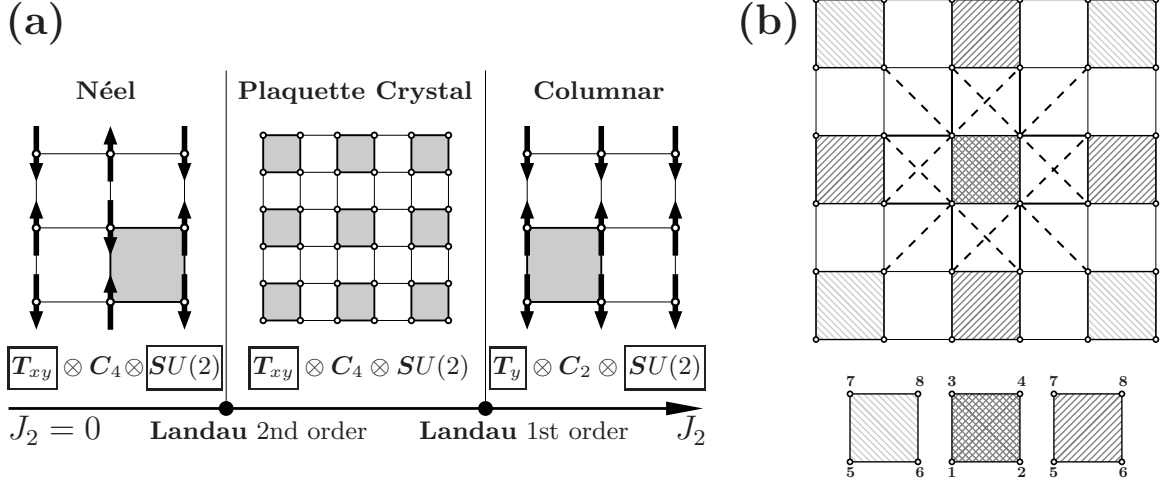
Figure 2.1: (a) A schematic phase diagram of the J_1-J_2 model, summarizing our results. In each phase we show spontaneously broken (framed symbols) and unbroken symmetries (usual symbols). The translational invariance is broken along both directions in the Néel and paramagnetic phases, and only along the y–direction in the columnar phase. This fact is indicated by the subscripts xy and y after T. Conclusions regarding the order of the phase transition separating Néel and plaquette crystal phases, as well as symmetries of various phases, are based upon extrapolation of our results towards the thermodynamic limit. (b) Symmetric covering of the 2D lattice with 2×2 plaquettes. Each plaquette is connected to 4 nearest and 4 next-nearest neighbors.

of the single-plaquette Hamiltonian

$$H_\square = J_1\big(\boldsymbol{S}_1 + \boldsymbol{S}_4\big)\big(\boldsymbol{S}_2 + \boldsymbol{S}_3\big) + J_2\big(\boldsymbol{S}_1\boldsymbol{S}_4 + \boldsymbol{S}_2\boldsymbol{S}_3\big)$$

with eigenvalues

$$\epsilon_{l_1 l_2 L} = \frac{J_1}{2}\Big[L\big(L+1\big) - l_1\big(l_1+1\big) - l_2\big(l_2+1\big)\Big] + \frac{J_2}{2}\Big[l_1\big(l_1+1\big) + l_2\big(l_2+1\big) - 3\Big]. \quad (2.1)$$

The next step is to establish how a plaquette couples to the rest of the system. In Fig. 2.1(b) we show the symmetric plaquette covering of the 2D lattice. In the figure, the vertices of every non-central plaquette are similarly labeled by the numbers $5, 6, 7, 8$, and total spins of diagonals are $\boldsymbol{l}_3 = \boldsymbol{S}_5 + \boldsymbol{S}_8$ and $\boldsymbol{l}_4 = \boldsymbol{S}_6 + \boldsymbol{S}_7$. In the

uncoupled basis, the matrix elements of the inter-plaquette interaction are:

$$\left(H_{\text{int}}^{\sigma}\right)_{a_1 a_2}^{a_1' a_2'} = \sum_{LM} \langle \lambda_1' \lambda_2', LM | H_{\text{int}}^{\sigma} | \lambda_1 \lambda_2, LM \rangle \times \qquad (2.2)$$

$$\times \langle L_1' M_1' L_2' M_2' | L_1' L_2' LM \rangle \langle L_1 M_1 L_2 M_2 | L_1 L_2 LM \rangle,$$

where $\sigma = 1$ ($\sigma = 2$) corresponds to the nearest (next-nearest) neighbor plaquette interaction, L_1, L_2 (L_1', L_2') represent initial (final) angular momenta of the two pla-quettes and $\boldsymbol{L} = \boldsymbol{L}_1 + \boldsymbol{L}_2$ is their total angular momentum. In this equation we have introduced the notations $\lambda_1 = \{l_1 l_2 L_1\}$, $\lambda_2 = \{l_3 l_4 L_2\}$ and $a_i = \{\lambda_i M_i\}$, and similarly for the primed indices. Because each plaquette has 4 nearest neighbors (NN) and 4 next-nearest neighbors (NNN) (see Fig. 2.1(b)), the symmetrized NNN interaction may be written as:

$$\langle \lambda_1' \lambda_2', LM | H_{\text{int}}^2 | \lambda_1 \lambda_2, LM \rangle = J_2 \rho_{L_1 L_2}^{L_1' L_2'}(L) \times$$

$$\times \left(S_3^{\lambda_1' \lambda_1} S_6^{\lambda_2' \lambda_2} + S_1^{\lambda_1' \lambda_1} S_8^{\lambda_2' \lambda_2} + S_2^{\lambda_1' \lambda_1} S_7^{\lambda_2' \lambda_2} + S_4^{\lambda_1' \lambda_1} S_5^{\lambda_2' \lambda_2} \right).$$

while the symmetrized NN plaquette interaction has the form:

$$\langle \lambda_1' \lambda_2', LM | H_{\text{int}}^1 | \lambda_1 \lambda_2, LM \rangle = J_1 \rho_{L_1 L_2}^{L_1' L_2'}(L) \left[\left(S_1^{\lambda_1' \lambda_1} + S_4^{\lambda_1' \lambda_1} \right) \left(S_6^{\lambda_2' \lambda_2} + S_7^{\lambda_2' \lambda_2} \right) + \right.$$

$$\left. + \left(S_2^{\lambda_1' \lambda_1} + S_3^{\lambda_1' \lambda_1} \right) \left(S_5^{\lambda_2' \lambda_2} + S_8^{\lambda_2' \lambda_2} \right) \right] + 2 \langle \lambda_1' \lambda_2', LM | H_{\text{int}}^2 | \lambda_1 \lambda_2, LM \rangle,$$

In the expressions for matrix elements of $H_{\text{int}}^{1,2}$ the symbols $S_n^{\lambda' \lambda} = \langle \lambda' \| S_n \| \lambda \rangle$ denote reduced matrix elements of the n-th spin operator, and:

$$\rho_{L_1 L_2}^{L_1' L_2'}(L) = \frac{1}{4}(-1)^{L + L_2' + L_1} \begin{Bmatrix} L_1' & L_2' & L \\ L_2 & L_1 & 1 \end{Bmatrix},$$

where $\{\cdots\}$ are Wigner $6j$-symbols (or Racah coefficients) [56].

Let us now identify the plaquette degree of freedom with a Schwinger boson γ_{ia} which creates a specific state of the plaquette: $|a\rangle_i \leftrightarrow \gamma_{ia}^\dagger$. The J_1-J_2 Hamiltonian (1.4) can be expressed in the plaquette basis as:

$$H = \sum_{i,a} \epsilon_a \gamma_{ia}^\dagger \gamma_{ia} + \sum_{\substack{\langle ij\rangle_\sigma \\ \sigma=1,2}} \left(H_{\text{int}}^\sigma\right)_{a_1 a_2}^{a_1' a_2'} \gamma_{ia_1'}^\dagger \gamma_{ja_2'}^\dagger \gamma_{ia_1} \gamma_{ja_2}, \tag{2.3}$$

where we abbreviated $\langle ij\rangle_\sigma = \left(\langle ij\rangle, \langle\langle ij\rangle\rangle\right)$, the operator $\gamma_{ia}^\dagger$ creates a boson on site i of the *plaquette* lattice (which contains $N_\square = N/4$ sites) in the state, denoted by an index a, running through the entire single-plaquette Hilbert space (of dimension $2^4 = 16$), and the summation is performed over doubly repeated dummy indices. The unphysical states are eliminated by enforcing the local constraint $\sum_a \gamma_{ia}^\dagger \gamma_{ia} = 1$. In what follows we impose periodic boundary conditions on the plaquette lattice. The bosonic operators γ_{ia} define the HL (see the beginning of this chapter) for our problem.

2.2.3 Hierarchical mean-field approximation

As follows from Eq. (2.1) the lowest single-plaquette state has energy $\epsilon_{1100}/4 = -J_1/2 + J_2/8$ per spin which, when $J_2 = 0$, gives only the energy of a classical 2D antiferromagnet. Thus it is necessary to take into account the interaction term in Eq. (2.3).

The HMF approximation is a mean-field approach, performed on the relevant degrees of freedom. Here we discuss the simplest one – a Hatree-Fock like (HF) approximation. A possible way to include fluctuation corrections is presented in Appendix B at the end of this chapter. The HF approximation introduces a mixing of single-plaquette states, which minimizes the total energy of the system and is based on a canonical transformation among the bosons. Here we consider only the

homogeneous case, when this transformation is plaquette-independent:

$$\gamma_{ia} = R_a^n \Gamma_{in}.$$

The matrix R (which we can choose to be real) satisfies canonical orthogonality and completeness relations:

$$R_a^n R_a^{n'} = \delta_{nn'}; \quad R_a^n R_{a'}^n = \delta_{aa'}$$

A *translationally invariant* variational ansatz for the ground state is a boson condensate in the lowest HF single-particle energy state ($n = 0$):

$$|\text{HF}\rangle = \prod_i \Gamma_{i0}^\dagger |0\rangle, \tag{2.4}$$

where $|0\rangle$ is the Schwinger boson vacuum. Since the state (2.4) has one boson per plaquette, there is no need to impose the Schwinger boson constraint in the calculation.

Minimizing the total energy with respect to R, we arrive at the self-consistent equation:

$$\left\{ \epsilon_a \delta_{aa'} + \sum_\sigma z_\sigma \left(H_{\text{int}}^\sigma\right)_{a' a_2}^{a a_1} R_{a_1}^0 R_{a_2}^0 \right\} R_{a'}^n = \varepsilon_n R_a^n, \tag{2.5}$$

where $z_1 = z_2 = 4$ are the nearest- and next-nearest coordination numbers. The ground state energy (GSE) per spin is then given by the expression:

$$\frac{E_0}{N} = \frac{\langle \text{HF}|H|\text{HF}\rangle}{N} = \frac{1}{8}\left(\varepsilon_0 + \sum_a \epsilon_a \left(R_a^0\right)^2 \right) \tag{2.6}$$

with ε_0 being the lowest eigenvalue of Eq. (2.5).

Another fundamental quantity to compute is the polarization of spins within a plaquette:

$$\langle \text{HF}|S_{in}^z|\text{HF}\rangle = \left(S_n^z\right)_{a'a} R_{a'}^0 R_a^0,$$

where $n = 1 \ldots 4$ is the spin index, and the matrix elements (determined from the Wigner-Eckart theorem) are:

$$(S_n^z)_{a'a} = \langle l_1' l_2' L' M' | S_n^z | l_1 l_2 L M \rangle = \qquad (2.7)$$
$$= (-1)^{L+L'+1} \delta_{MM'} \frac{\langle 1 0 L M | 1 L L' M \rangle}{\sqrt{2L'+1}} \langle l_1' l_2' L' || S_n || l_1 l_2 L \rangle.$$

This enables us to define the staggered and columnar (along x and y lattice directions) magnetizations:

$$M_{\text{stag}} = \frac{1}{4} \langle \text{HF} | S_1^z + S_4^z - S_2^z - S_3^z | \text{HF} \rangle; \qquad (2.8)$$
$$M_{\text{col}}(x, y) = \frac{1}{4} \langle \text{HF} | S_1^z - S_4^z + S_{2,3}^z - S_{3,2}^z | \text{HF} \rangle.$$

Notice the extreme simplicity of the HMF approximation. The reason why it is able to realize meaningful results is that the plaquette degree of freedom seems to contain the main correlations defining the physics of the J_1-J_2 model. To avoid confusion, we emphasize that the HF approximation and the fluctuation theory of Appendix B are physically (and obviously mathematically) different from the spin-wave or canonical Schwinger-Wigner boson mean-field approach to spin systems [57]. In particular, *we make no assumption about the underlying ground state*, thus allowing for an interplay of various quantum phases. Moreover, it will be demonstrated that the collective excitation spectra in each phase consistently reflect spontaneously broken symmetries, unlike the usual Schwinger boson case [57] in which one obtains gapped excitations.

2.2.4   GS properties and excitation spectrum of the model

Our choice of the plaquette as an elementary degree of freedom remains unjustified at this point. In order to show its relevance we applied the HMF analysis to several
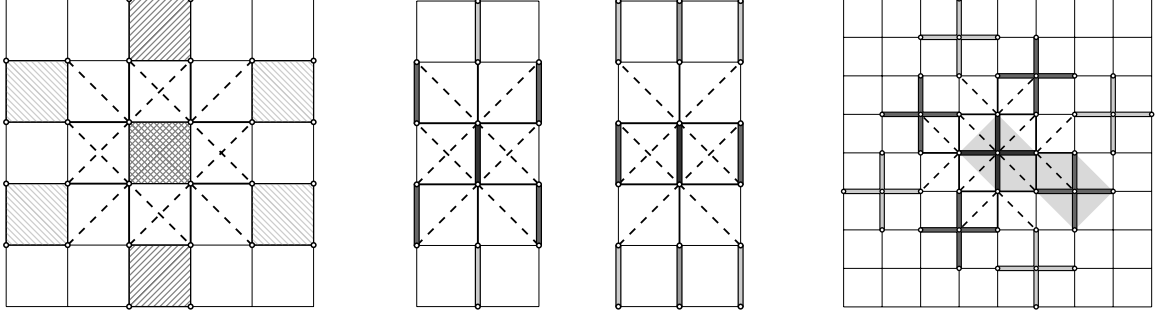
Figure 2.2: Different tesselations and clusters used in the HMF calculation. Left: displaced plaquette covering. Notice that the C_4 symmetry is broken down to C_2. Center: Connectivity of the dimer lattice for displaced (left) and symmetric (right) dimer coverings. The rotational C_4 symmetry is lowered to C_2 in both cases. Right: Covering of the lattice with crosses – arrays of five spins. Since one cross cannot form a singlet, it is necessary to double the unit cell, as indicated by the gray shading. This choice of a degree of freedom clearly preserves the C_4 symmetry, but the resulting lattice breaks it.

other tesselations (besides the symmetric plaquette covering, case (a), shown in Fig. 2.1, right panel): (b) *superplaquette* (spin cluster 4×4) degree of freedom, covering the lattice in such a way that C_4 is preserved (for details see Appendix A at the end of this chapter); (c) displaced plaquette covering of the lattice, Fig. 2.2, left panel; (d) symmetric and displaced *dimer* coverings, shown in the center panel of Fig. 2.2; (e) *cross* degree of freedom, Fig. 2.2, right panel. One should observe that symmetries of the original Bravais lattice are preserved only in cases (a) and (b). In cases (c) and (d) the lattice rotational symmetry C_4 is lowered to C_2. Case (e) is special in the sense that an isolated degree of freedom does not possess a singlet ground state. The information about a particular configuration is encoded in matrix elements of H_{int}^{σ}, whose calculation is elementary. Other equations presented above retain their form.

For each of the above cases we iteratively solve Eq. (2.5) and compute the GSE (2.6), staggered and columnar magnetizations (2.8)). The main message, which we would like to convey here, is that only the plaquette degree of freedom (of any size) is relevant for constructing the phase diagram of the J_1-J_2 model.

(i) Symmetry preserving plaquette configurations

Let us focus first on cases (a) and (b), i.e. symmetry-preserving coverings of the lattice with plaquette (Fig. 2.1(b)) and superplaquette (Fig. 2.12) degrees of freedom. The resulting GSE as a function of J_2/J_1 is shown in Fig. 2.3(a). One immediately observes a level-crossing at $J_2^{c2} \approx 0.67J_1$, indicating the first-order transition and a second-order quantum critical point at $J_2^{c1} \approx 0.42J_1$, which is supported by a jump of the second order derivative d^2E_0/dJ_2^2, Fig. 2.3(b). Néel and columnar phases are characterized by spontaneously broken $SU(2)$ symmetry. The former exhibits a nonvanishing staggered magnetization (M_{stag}) while the latter has nonzero columnar magnetization along the x-direction ($M_{\text{col}}(x)$). Both order parameters become zero in the paramagnetic phase, suggesting that $SU(2)$ is restored. These results are summarized in Fig. 2.4(a), from which it also follows that the phase transition at J_2^{c1} is continuous, while J_2^{c2} corresponds to a first-order transition point. Recall that our approach does not explicitly break the spin rotational symmetry, thus allowing for the treatment of competing ground states.

As expected, considering a larger elementary degree of freedom – superplaquette – leads to a significant improvement of the GSE and reduction of the magnetization, due to larger quantum fluctuations. The finite-size scaling (insets in Figs. 2.3(a) and 2.4(a)), using these two sizes (2×2 and 4×4), indicates that $E_0(J_2 = 0)/N \to -0.64J_1$ and $M_z(J_2 = 0) \to 0.39$ in the thermodynamic limit, a satisfying result for a HF approximation, which completely ignores fluctuations (these numbers should be compared with well-known results of Monte-Carlo simulations [58]: $E_0/N \approx -0.67J_1$ and $M_z \approx 0.31$).

Next we focus on symmetry properties of the various phases in Fig. 2.1(a). At all values of $J_2 \leq J_2^{c2}$ the lattice translational symmetry T is broken, but the rotational C_4 symmetry is preserved. For $J_2 \leq J_2^{c1}$ this corresponds to a Néel-type long-range order with spontaneously broken $SU(2)$. At large values $J_2 \geq J_2^{c2}$ we ob-
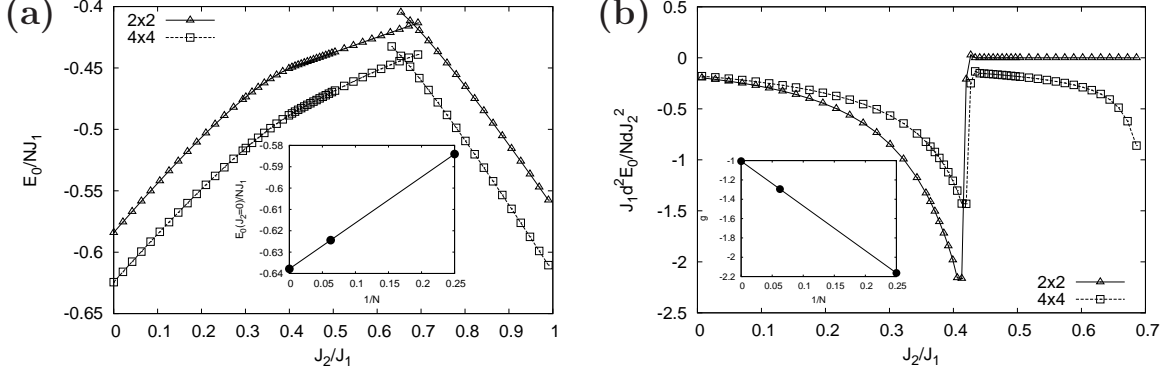
Figure 2.3: (a) Ground state energy per spin computed at the HF level for the 2×2 and 4×4 plaquette elementary degrees of freedom. The inset shows finite-size scaling in the AF phase at $J_2 = 0$. (b) Second-order derivative $d^2 E_0/dJ_2^2$ for the 2×2 and 4×4 plaquette degrees of freedom. The discontinuity at $J_2/J_1 \approx 0.42$ is indicative of a second-order quantum phase transition. In the inset we present finite-size scaling for the jump $g \equiv (J_1 d^2 E_0/N d J_2^2)_{J_2^{c1}-0}^{J_2^{c1}+0}$.

serve the columnar ordering, which spontaneously breaks C_4 down to C_2, and $SU(2)$, but partially (i.e. along one direction) restores the lattice translational symmetry. We present a more detailed discussion of the spatial symmetries later. In the intermediate region $J_2 \in (J_2^{c1}, J_2^{c2})$ the spin $SU(2)$ rotational symmetry is restored. In this paramagnetic phase the ground state wavefunction is a tensor product of individual plaquette ground states (with quantum numbers $l_1 = l_2 = 1$, $L = M = 0$):

$$|1100\rangle = \frac{1}{2\sqrt{3}} \Big[2\big(|\uparrow_1\uparrow_4\downarrow_2\downarrow_3\rangle + |\downarrow_1\downarrow_4\uparrow_2\uparrow_3\rangle\big) -$$

$$- \big(|\uparrow_1\downarrow_4\uparrow_2\downarrow_3\rangle + |\uparrow_1\downarrow_4\downarrow_2\uparrow_3\rangle + |\downarrow_1\uparrow_4\uparrow_2\downarrow_3\rangle + |\downarrow_1\uparrow_4\downarrow_2\uparrow_3\rangle\big)\Big],$$

where arrows denote S^z-eigenstates of spins within the plaquette (for site numbering see Fig. 2.1(b)). This ground state necessarily breaks the lattice translational symmetry, but preserves C_4. In fact, the paramagnetic region in Fig. 2.4(b) is a trivial plaquette crystal: a set of *non-interacting* plaquettes, because the expectation value of the plaquette interaction (see Eq. (2.3)) in the singlet state $\prod_i \gamma_{i,(1100)}^\dagger |0\rangle$ vanishes.
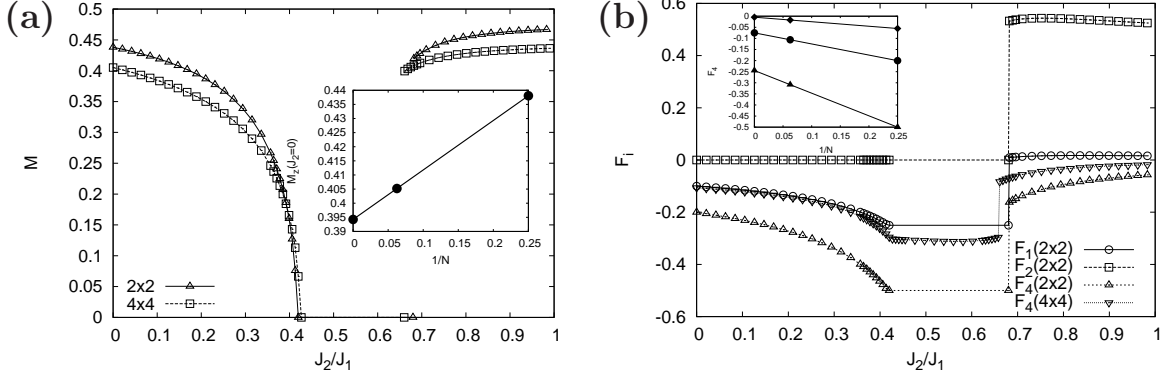
Figure 2.4: (a) Staggered magnetization, M_{stag}, for $J_2 \leq J_2^{c1}$ and columnar magnetization along the x-direction, $M_{\text{col}}(x)$, for $J_2 \geq J_2^{c2}$ (for the 2×2 and 4×4 plaquette degrees of freedom), computed at the HF level. Notice the continuous phase transition at $J_2/J_1 \approx 0.42$ and a first-order transition at $J_2/J_1 \approx 0.68$ (2×2) and $J_2/J_1 \approx 0.66$ (4×4). The inset shows finite-size scaling of M_{stag} at $J_2 = 0$. (b) HF ground state expectation values of the symmetry-breaking perturbations, given by Eq. (2.9), plotted as functions of J_2/J_1 for the plaquette and superplaquette degrees of freedom. Due to the C_4 symmetry in the Néel and paramagnetic phases, values of F_4 are twice larger than the corresponding values of F_1. The inset shows finite-size scaling for F_4 for three values of J_2/J_1: 0 (circles), 0.504 (triangles) and 0.997 (rhombs).

An analogous situation is realized when the superplaquette is chosen as an elementary degree of freedom: the paramagnetic phase is a crystal of superplaquettes. It is interesting to note that in [39] a "plaquette resonating-valence-bond state", exactly equal to $|1100\rangle$, has been proposed. However, later [40] the intermediate phase was argued to be a spin liquid, i.e. a state that preserves the lattice translational symmetry.

In order to learn about spatial symmetries in various phases, we compare magnitudes of the several lattice symmetry-breaking observables proposed in the literature. We consider the following three, introduced in [42] (in the notation of that paper):

$$F_1 = \frac{1}{N} \sum_{x,y} (-1)^x \boldsymbol{S}_{x,y} \boldsymbol{S}_{x+1,y};$$

$$F_2 = \frac{1}{N} \sum_{x,y} \boldsymbol{S}_{x,y} \big(\boldsymbol{S}_{x+1,y} - \boldsymbol{S}_{x,y+1} \big);$$

$$F_4 = \frac{1}{N} \sum_{x,y} \boldsymbol{S}_{x,y} \big[(-1)^x \boldsymbol{S}_{x+1,y} + (-1)^y \boldsymbol{S}_{x,y+1} \big],$$
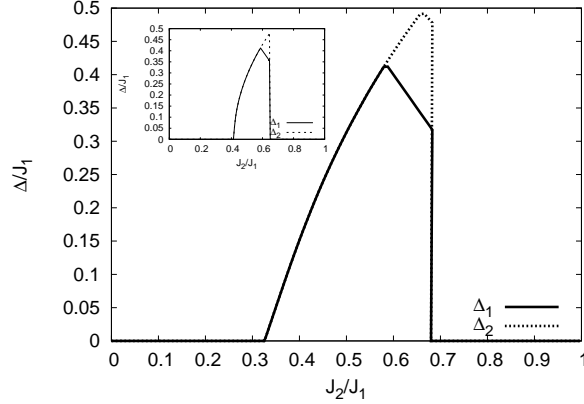
Figure 2.5: The two lowest excitation energies taken at the center of the plaquette Brillouin zone. The main panel shows the self-consistent solution to Bogoliubov's equations, while the inset corresponds to the solution without self-consistency (i.e. by linearizing the HMF equation (2.5)). Since wavefunctions of collective excitations in the Néel and columnar phases have different symmetries, there are level crossings in the non-magnetic phase (cusps in the plot).

where indices x, y specify a spin in the 2D lattice. The operator F_4 probes the plaquette ordering, which preserves the lattice rotational symmetry, while F_1 and F_2 correspond to the columnar ordering. We note that F_1 is already non-zero for an isolated plaquette (or superplaquette). These functions can be combined in the complex "order parameter" introduced in [48]. Here we show details of the calculation of functions $F_{1,2,4}$ for the plaquette degree of freedom (case (a)) and only present the result for F_4 for the superplaquette (case (b)). In the plaquette representation the above operators are written as:

$$F_1 = \frac{1}{N} \sum_{i,j} \left[\left(\boldsymbol{S}_{1;i,j} \boldsymbol{S}_{2;i,j} + \boldsymbol{S}_{3;i,j} \boldsymbol{S}_{4;i,j} \right) - \left(\boldsymbol{S}_{2;i,j} \boldsymbol{S}_{5;i+1,j} + \boldsymbol{S}_{4;i,j} \boldsymbol{S}_{7;i+1,j} \right) \right]; \qquad (2.9)$$

$$F_{2,4} = \frac{1}{N} \sum_{i,j} \left[\left(\boldsymbol{S}_{1;i,j} \mp \boldsymbol{S}_{4;i,j} \right) \left(\boldsymbol{S}_{2;i,j} \mp \boldsymbol{S}_{3;i,j} \right) \pm \left(\boldsymbol{S}_{2;i,j} \boldsymbol{S}_{5;i+1,j} + \boldsymbol{S}_{4;i,j} \boldsymbol{S}_{7;i+1,j} \mp \right. \right.$$

$$\left. \left. \mp \boldsymbol{S}_{3;i,j} \boldsymbol{S}_{5;i,j+1} \mp \boldsymbol{S}_{4;i,j} \boldsymbol{S}_{6,i,j+1} \right) \right].$$

In this equation the indices i, j are coordinates of a plaquette in the lattice.

Expectation values of the functions (2.9) in the HF GS are shown in Fig. 2.4(b). Both phase transition points J_2^{c1} and J_2^{c2} are clearly seen from this plot. All functions change continuously across the second-order critical point J_2^{c1} and jump at the first-order transition point J_2^{c2}. Except in the columnar phase the values of F_4 are everywhere exactly twice larger than those of F_1, which is an indication of the unbroken four-fold rotational symmetry of the lattice in these regions. In the columnar phase, on the other hand, this symmetry is broken and the above relation does not hold. While in the Néel and columnar phases nonlocal terms in Eq. (2.9) are important, in the paramagnetic state the only contribution to either expectation value comes from isolated plaquettes (local terms in (2.9)), or superplaquettes. This observation is consistent with properties of the ground state in the non-magnetic phase, discussed earlier in this section.

As we already mentioned, any choice of a degree of freedom breaks explicitly the lattice translational symmetry T, with the result that links in the lattice become inequivalent. Indeed, the functions of Eq. (2.9), defined on the links, have non-zero values even in the AF phase at $J_2 = 0$. However, this effect vanishes in the thermodynamic limit (i.e. as the size of the degree of freedom is increased). The finite-size scaling for $F_4(J_2/J_1)$ is presented in the inset to Fig. 2.4(b). The three extrapolated values: $F_4(0) = -0.075$, $F_4(0.504) = -0.245$ and $F_4(0.997) = -0.004$, suggest that the "link-wise" translational invariance is restored in the thermodynamic limit in the Néel and columnar phases, but not in the plaquette crystal phase. Moreover, the value of the jump $g \equiv J_1 d^2 E_0 / N d J_2^2 \big|_{J_2^{c1}-0}^{J_2^{c1}+0}$, extrapolated to the thermodynamic limit (see inset to Fig. 2.3(b)) remains finite: $g(J_2^{c1}) = -1.006$. In other words, these results imply that the critical point J_2^{c1} corresponds to the usual Landau second-order phase transition.

(ii) Collective excitations in the plaquette crystal phase

Until now we have considered only ground-state properties of the J_1-J_2 model. Low-lying excited states also represent considerable interest. The paramagnetic phase is known to have gapped excitations, while Néel and columnar phases exhibit Goldstone modes. Thus the phase transition points J_2^{c1} and J_2^{c1} must be accompanied by the opening of a gap in the excitation spectrum: the former in a continuous and the latter in a discontinuous fashion. In Appendix B we present a particular method to obtain the collective spectrum of the system. The main idea of this approximation is borrowed from the Bogoliubov-Fetter theory of superfluidity [59]. Assume that on each plaquette the majority of Schwinger bosons form a condensate in an appropriately chosen lowest energy state and neglect fluctuations in the number of condensed particles. Due to the Schwinger boson constraint, this quantity has the meaning of a probability to find a given plaquette in the lowest energy HF state, rather than the number of particles. Nevertheless, we will call it the condensate fraction n_0, which, in principle, should be determined self-consistently, and is a measure of the applicability of the entire approximation: it should satisfy the inequality $|n_0 - 1| \ll 1$. Once the condensation part is separated from γ_{ia}, what remains describes fluctuation corrections to the HF ground state. These fluctuations have rather strong effects near the phase transition points, leading to a considerable shift of J_2^{c1} and a smaller change in value of J_2^{c2}. These facts imply that our approximation breaks down near the phase transition points. In Appendix B it is shown that close to the transition, the condensate is strongly suppressed. Deep in each phase $n_0 \sim 0.9$ and the approximation is valid, allowing us to draw conclusions about general properties of the collective spectrum.

The complete summary of the results is given in Appendix B. Here we only present the most interesting one: the gap in the excitation spectrum as a function of J_2/J_1. Although we focus only on case (a) (2×2 plaquette), the superplaquette degree of

freedom can be considered in a similar manner. The gap always occurs in momentum space at $\boldsymbol{k} = 0$, which reflects translational invariance of the *plaquette* lattice. Below we focus only on this point in the plaquette Brillouin zone. In fact, there are $16 - 1 = 15$ collective branches and only some of them become gapless in the phases with spontaneously broken $SU(2)$. However, in the paramagnetic phase all branches develop a gap. In Fig. 2.5 we show the energy gap $\Delta(J_2) = \omega(\boldsymbol{k} = 0, J_2)$ for the two lowest excitation branches in a system of 100×100 plaquettes, which approximates well the thermodynamic limit. The main panel shows results of the self-consistent solution of Bogoliubov's equations. The inset compares it with the solution of the HMF (or Gross-Pitaeveskii) equation (2.5), linearized around the mean-field solution. This procedure corresponds to the weak-coupling approximation. In the Néel and columnar phases there are two spin wave-type Goldstone modes, both of which acquire a gap in the paramagnetic phase at J_2^{c1} and J_2^{c2}. However, as follows from Fig. 2.5, the positions of these points change from their HF values to $J_2^{c1} \approx 0.33 J_1$ and $J_2^{c2} \approx 0.65 J_1$. The critical point J_2^{c1} was obtained by extrapolation of the staggered magnetization curve (Fig. 2.13(b)) to zero and the first-order point J_2^{c2} by extrapolating the two GSE curves in Fig. 2.13(a) until intersection. The single-plaquette physical picture discussed previously in connection with the paramagnetic phase remains valid, e.g. the condensation occurs again in the plaquette state $|1100\rangle$. Using this observation and symmetries of the matrix elements $\left(H_{\text{int}}^{\sigma}\right)_{ab}^{a'b'}$, one can rigorously show the existence of a gap in the non-magnetic region. We can say that it is a property of our HMF approximation, rather than a numerical evidence.

(iii) Other degrees of freedom

Finally we comment on the results for cases (c)-(e) which, contrary to the configurations considered before, explicitly break lattice rotational symmetry (see Fig. 2.2). The corresponding GSEs are shown in Fig. 2.6. In contrast to the previously con-
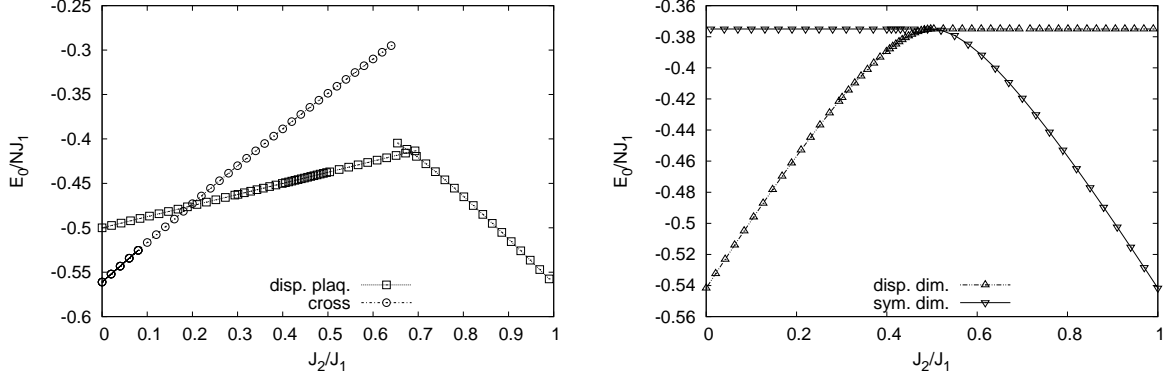
Figure 2.6: HF ground state energy per spin for the displaced plaquette and cross (left panel), and dimer (right panel) coverings.

sidered scenarios, these cases give *qualitatively* wrong phase diagrams. Indeed, if we cover the lattice with displaced plaquettes or crosses, there exists no classical spin configuration which gives the long-range Néel order. On the other hand, such a configuration exists for the columnar state. For the displaced plaquette covering the low-J_2 phase $J_2 \leq J_2^{c2}$ is an $SU(2)$ singlet, and spatially is a set of non-interacting plaquettes (notice the coincidence of 2×2–plaquette energies in the paramagnetic phases of Figs. 2.3(a) and 2.6). Thus the phase transition to the columnar state is the first-order. For the cross covering, on the other hand, $SU(2)$ is explicitly broken for all values of J_2, but since the columnar phase partially restores the lattice translational invariance, it is again separated from the non-magnetic state by a first-order phase transition point. The two dimer configurations (case (d)) are complementary to each other in the sense that one of them has only the classical Néel state and another – only the columnar phase. It follows that these configurations can have only one second-order critical point at which $SU(2)$ is restored and other symmetries remain broken. These observations imply that the coarse graining prescriptions (c)-(e) are probably a bad starting point for any approximation scheme.

2.2.5 Concluding remarks

Let us now put our main conclusions in perspective by making several summarizing remarks. It should be emphasized that the discussion below is based on the results of the finite-size scaling analysis. From our presentation it follows that dimer (bond) order is always unfavorable in the non-magnetic phase. Notice that even when the plaquette coverings were considered such an order did not occur, although spontaneous dimerization was not explicitly prohibited. Instead the quantum paramagnetic phase prefers to preserve the lattice rotational symmetry, which makes the phase transition separating it from the Néel phase fit perfectly well within the Ginzburg-Landau paradigm. The data presented for the staggered magnetization (Fig. 2.4(a)) and symmetry-breaking observables (Fig. 2.4(b)) indicate that the symmetry group of the Néel state is a subgroup of the symmetry group in the paramagnetic phase, as both phases break T and preserve C_4, but the latter also preserves $SU(2)$. On the contrary, there is no such group-subgroup relation between the paramagnetic and columnar antiferromagnetic phases. Consequently, the transition between these two states is first order. These observations are summarized in Fig. 2.1(a). Starting from the known symmetry in the Néel state and assuming validity of the Landau theory, one can unambiguously rule out dimerized structures in the paramagnetic phase, since they break lattice rotational symmetry. Therefore our results do not favor the scenario of deconfined quantum criticality advocated in [48, 42]. As we already mentioned several times, our method explicitly breaks a particular lattice translational symmetry: the ground state in Eq. (2.4) at $J_2 = 0$ (AF phase), is not invariant under a [11] lattice translation. One way to cure this problem is to consider variational wavefunctions of the "resonating plaquette" type:

$$|\Psi\rangle = \left(1 + T_{11}\right)|\text{HF}\rangle,$$

which restore that symmetry (T_{11} is the translation operator along the [11] direction in the lattice). This state describes two resonating plaquette configurations, shifted with respect to each other along [11]. Results of calculations using this wavefunction for systems up to 6×6 spins indicate that for $J_2 < J_2^{c1}$ the ground state has long-range Néel order and is paramagnetic for $J_2 \in (J_2^{c1}, J_2^{c2})$. The intermediate phase has a plaquette crystal order, but with partially restored translational invariance. The phase transition at J_2^{c1} is still of the second-order, which is not surprising as it can be described solely in terms of the $SU(2)$ order parameter. Based on these small system sizes, we can not definitively conclude whether this phase transition remains of the second-order or becomes weakly first-order in the thermodynamic limit.

Next we observe that, despite profound differences between the 2D and 1D equivalent J_1-J_2 models, their non-magnetic phases present some similarities. The one-dimensional model is known to be quasi-exactly solvable [60] at the point $J_2 = 0.5J_1$ and exhibits a paramagnetic ground state with short-range correlations for J_2 above the critical value [61] $J_2^c \approx 0.24J_1$ (due to the peculiar physics in one dimension, the critical point J_2^c is an essential singularity and may not be accessible for the HMF approximation of the type presented here). In this non-magnetic region the ground state is doubly degenerate, corresponding to two possible coverings of a 1D lattice with dimers, in accordance with the Lieb-Schultz-Mattis theorem [62]. Unfortunately, a finite-size scaling calculation for the gap between the lowest and first excited energy levels, based on exact diagonalization of the 2×2 and 4×4 clusters with periodic boundary conditions, does not provide a definitive answer to the question of whether the ground state of the 2D J_1-J_2 model becomes degenerate in the region $J_2^{c1} \leq J_2 \leq J_2^{c2}$. This is indeed what one would expect on the basis of a generalization of the Lieb-Schultz-Mattis theorem to higher space dimensions (see, e.g. [63]). At the HF level, it is true that different *plaquette* coverings of the lattice have the same energy (simply because each plaquette is in its singlet ground state). How-

ever, the total number of such configurations grows *sub-exponentially* $\sim 2^{\sqrt{N}}$, which should be contrasted with the dimer covering problem, where this number is known [64] to be exponentially large. Based on this distinction, one may speculate that if our plaquette picture is valid, there is not enough different plaquette configurations for the paramagnetic phase to become a spin liquid (i.e. a *resonating plaquette state*). This statement requires a separate investigation.

Finally, we emphasize that our main goal was to investigate the fundamental symmetries of the phases exhibited by the J_1-J_2 model. Although the energies presented for the 2×2 and 4×4 plaquette cases are higher than those obtained by more sophisticated numerical methods, they can be systematically improved by considering correlated trial wavefunctions or by using more complex methods which build upon the results reported here. However, we expect that our conclusions on the symmetries of the phases will remain unchanged.

In summary we analyzed the phase diagram of the 2D J_1-J_2 model on a square lattice, focusing on symmetries of the various phases. It was shown that in this model the HL [33] is defined by identifying the *plaquette as a relevant degree of freedom*. Consistent with previous works, we found the quantum paramagnetic phase in the interval $0.42 \leq J_2/J_1 \leq 0.66$. Our analysis indicates that the paramagnetic phase is a *plaquette crystal*, preserving both lattice and spin rotational symmetries. Extrapolation of our numerical results to the thermodynamic limit suggests that the Ginzburg-Landau paradigm of phase transitions is perfectly applicable in this case. Within the HMF there is a group-subgroup relation between symmetries of the non-magnetic and Néel phases, which are thus separated by a second-order phase transition. On the contrary, such relation does not exist between the plaquette crystal and columnar antiferromagnetic phases, so the corresponding transition is first order. We also proposed a way to include fluctuations around the HMF GS and demonstrated that the quantum paramagnetic state is characterized by a finite gap in the excitation

spectrum, which vanishes in the long-range ordered Néel and columnar phases.

2.3 Local physics of magnetization plateaux in the Shastry-Sutherland model

In the present section we will use the HMF approach to address the physical mechanism responsible for emergence of magnetization plateaux in the Shastry-Sutherland model. It will be shown that a plateau is stabilized in a certain *spin pattern*, satisfying *local* commensurability conditions. Results presented in this section provide evidence in favor of a robust local physics nature of the plateaux states, and are in agreement with recent nuclear magnetic resonance (NMR) experiments on $SrCu_2(BO_3)_2$.

2.3.1 Introduction

The interplay between quantum mechanics and the atomic lattice topology often leads to a complex mosaic of physical phenomena in low-dimensional frustrated magnets [65]. A prominent representative of this class of materials is the layered compound $SrCu_2(BO_3)_2$, which recently received a lot of attention because of its fascinating properties in an external magnetic field h, namely the emergence of magnetic plateaux at certain fractions of the saturated magnetization M_{sat}. The first experimental observations of the plateaux were reported in [66] for $m = M/M_{sat} = 1/8$ and $1/4$, and somewhat later for $m = 1/3$ [67]. Subsequent NMR experiments [68, 69] revealed spontaneous breaking of the lattice translational symmetry within the $1/8$ plateau, and also indicated that the spin superlattice persists right above this fraction [70]. The field was reignited by the work of Sebastian et al. [71], where additional plateaux at exotic values $m = 1/9$, $1/7$, $1/5$ and $2/9$ were reported. However, direct observation of the emerging spin superstructures remains an experimental challenge, primarily due to the high magnetic fields ($\sim 30 - 50$ Tesla) involved in measurements.
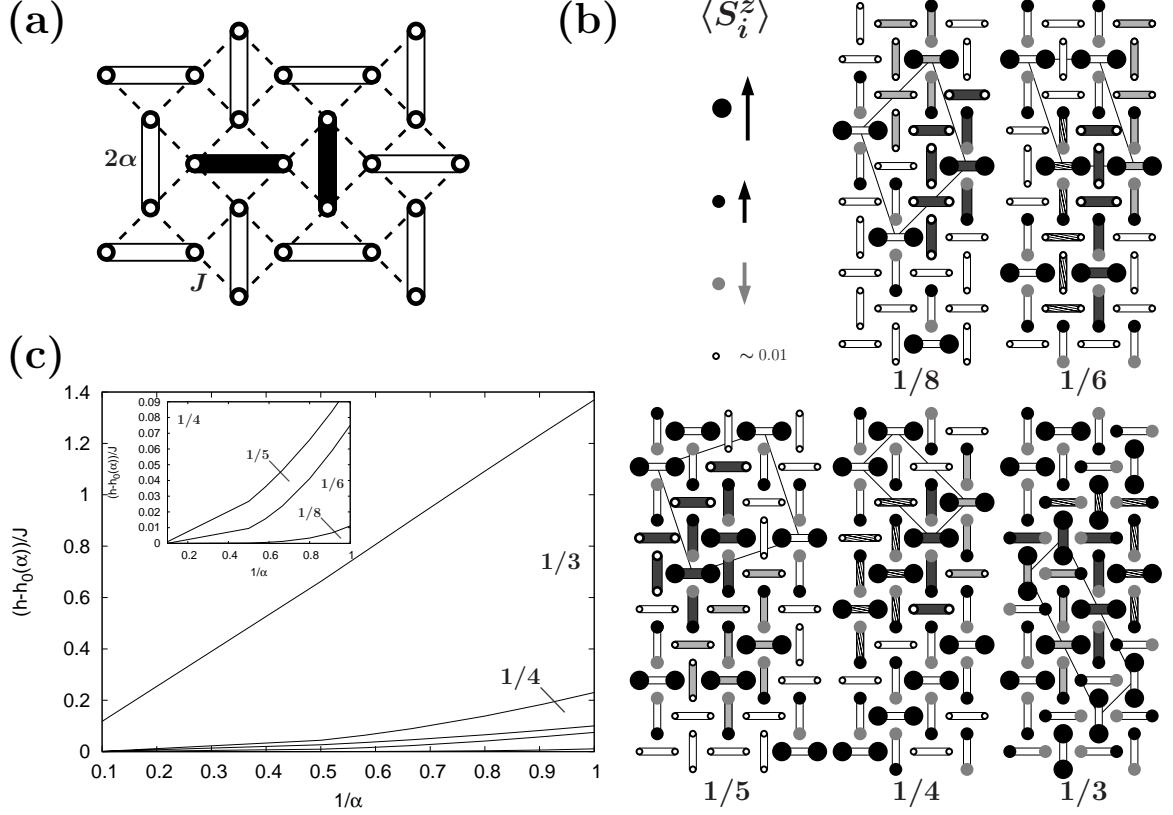
Figure 2.7: (a) The SS lattice. Circles denote spins, dashed lines correspond to the NN J coupling, double solid lines denote next-NN interactions (dimers). The simplest choice of a degree of freedom which does not cut dimers is shown in black. (b) Schematic spin profiles within plateaux. (Gray) black circles correspond to polarizations (anti) parallel to the field; their sizes encode the magnitude of the local magnetic moment. Empty circles denote sites with $|\langle S_i^z \rangle| \lesssim 10^{-2}$. The clusters used in HMF calculations consist of dark gray dimers. Light gray dimers represent the NN cluster. For $m = 1/3$, $1/4$ and $1/6$ dark and hatched dimers constitute the 24-spin cluster. Thin lines indicate unit cells of the spin superlattice. (c) High magnetic field phase diagram of the SS model for $\alpha \geqslant 1$. $h_0(\alpha)$ denotes the field after which the first plateau (at $1/8$) emerges. Fractions indicate values of m. For $\alpha \gg 1$ the triplons (●—●) in panel(b) become fully polarized and other dimers within the clusters turn into perfect singlets.

The nature of the magnetic states and physical mechanism leading to the plateaux are also not yet understood. It is believed that the Heisenberg antiferromagnetic model on a frustrated Shastry-Sutherland (SS) lattice with N sites [72] (see Fig.

2.7(a)),

$$H = J \sum_{\langle ij \rangle} \boldsymbol{S}_i \cdot \boldsymbol{S}_j + 2J\alpha \sum_{[ij]} \boldsymbol{S}_i \cdot \boldsymbol{S}_j - h \sum_i S_i^z, \qquad (2.10)$$

captures the essential magnetic properties of $SrCu_2(BO_3)_2$ in relatively high fields. In Eq. (2.10) $\boldsymbol{S}_i$ denotes a spin-1/2 operator at site i; the first sum is the usual nearest-neighbor (NN) Heisenberg term, while the second one runs over dimers; J and $\alpha \geqslant 0$. This model is quasi-exactly solvable [72] for $\alpha \geqslant 1 + h/2$: the GS is a direct product of singlet dimer states, and was shown to be stable up to $\alpha \sim 0.71\text{-}0.75$ in zero field [73]. In general, it is an intractable quantum many-body problem where approximation schemes are needed to deal with large-N systems.

All theories proposed to explain the magnetization plateaux in $SrCu_2(BO_3)_2$ start from the SS model. However, the physical mechanism stabilizing the plateau states, their nature, and the structure of the magnetization curve are still actively debated. Current ideas can be broadly divided into two groups. The first one advocates subtle non-local (in the spins) correlations leading to an underlying spin structure which preserves lattice symmetries [74]. It employs a mapping of the original spins to fermions coupled to a Chern-Simons gauge field, and then performs a Hartree-Fock decoupling. In this way the qualitative shape of the $SrCu_2(BO_3)_2$ magnetization curve was reproduced in high fields, but the lowest plateau at 1/8 was missing. Later this non-local mean-field approach was extended to include inhomogeneous phases [71], and it was argued that the plateaux correspond to stripe states with broken lattice symmetries. Remarkably the length scale ξ associated with the emerging spin superlattice was found to be $\xi \sim 100$ lattice spacings. The second group contends that the magnetization process can be described in terms of polarized dimers (triplons), which propagate in the background of singlet dimers [73, 75]. They developed effective hard-core boson models (truncating the original dimer Hilbert space), solved by perturbative [76] or contractor renormalization (CORE) [77] techniques, and found that the plateaux

states correspond to crystal phases with $\xi \sim 10$ lattice constants.

Such diversity of theoretical predictions demands further investigation. Here we use the HMF method presented in the previous section in an attempt to clarify the nature and physical mechanism, responsible for the emergence of magnetic plateaux in the SS model. Unlike previous calculations we deal directly with the SS Hamiltonian (2.10) (not with effective Hamiltonians as in [76, 77]) and combine exact diagonalization data with a simple and *controlled* approximation for the GS wavefunction. For instance, we do not discard the $M = 0$ dimer triplet states necessary for the propagation of a triplon. We focus on higher-lying fractions whose existence has been confirmed experimentally. Our conclusions support the *local* physics nature of the plateau states. In particular, we explicitly demonstrate how to construct those robust states based on a set of certain commensurability rules. Our results are also in agreement with the interpretation of NMR measurements [68].

2.3.2   HMF approach for the SS model

Application of the HMF method to the SS model starts by recalling that phases within plateaux break the lattice translational invariance. Therefore the best solution will be obtained if the cluster degree of freedom matches the unit cell of the spin superstructure. In terms of the coarse-grained cluster variables the SS model (2.10) can be written in a form similar to Eq. (2.3):

$$H = \sum_i \epsilon_a(\alpha, h) \gamma_{ia}^\dagger \gamma_{ia} + \sum_{\langle ij \rangle_\sigma} \left(H_{\text{int}}^\sigma \right)_{ab}^{a'b'} \gamma_{ia'}^\dagger \gamma_{jb'}^\dagger \gamma_{ia} \gamma_{jb}, \qquad (2.11)$$

where i denotes sites in the coarse-grained lattice, ϵ_a are exact cluster eigenenergies, and the symbol $\langle ij \rangle_\sigma$, with $\sigma = 1, 2, \ldots$, indicates pairs of neighboring blocks coupled by the same number of J-links. The operators $\gamma_{ia}^\dagger$ which create a particular state $|a\rangle$ of a N_q-spin cluster are $SU\left(2^{N_q}\right)$ Schwinger bosons (see the discussion after

49

Eq. (2.3)). Since the original SS Hamiltonian involves only two-spin interactions, in the new representation there will be only two-boson scattering processes: the corresponding matrix elements are denoted by $\left(H_{\text{int}}^{\sigma}\right)_{ab}^{a'b'}$. For each cluster size (N_q) and magnetization

$$m = \frac{1}{M_{\text{sat}}} \sum_i \langle S_i^z \rangle = \frac{2}{N} \sum_i \langle S_i^z \rangle = \frac{2}{N_q} \sum_{j=1}^{N_q} \langle S_j^z \rangle,$$

we determine the lowest-energy configuration (i.e. the cluster shape and corresponding tiling of the lattice). By virtue of above argument, this solution will have the "right" symmetry. Performing this operation for successive values of N_q up to the largest one that can be handled, we obtain a set of magnetization plateaux together with their corresponding spin profiles. It follows that a particular choice of coarse graining is critical for the success of this programme. One should recall that the experimental value for α in $\text{SrCu}_2\left(\text{BO}_3\right)_2$ is 0.74-0.84, i.e. the intradimer coupling seems to be "more relevant" than the interdimer one. Therefore it is natural to consider only those clusters, which contain an integer number of α-links. This constraint turns out to be quite severe. It follows that the degree of freedom must also contain an integer number of "minimal" blocks, shown in Fig. 2.7(a) in black: otherwise the tiling of the lattice will not be complete. These requirements comprise a set of local commensurability conditions necessary to stabilize a plateau.

Similar to the J_1-J_2 model, discussed in the previous section, we will use the variational GS wavefunction of the form (2.4): $|\psi_0\rangle = \prod_i \left(R_a \gamma_{ia}^\dagger\right)|0\rangle$, and solve the resulting Hartree-Fock equation. In this manner one obtains the approximate GS energy E_0 as a function of the magnetic field h.

Table 2.1: Representative values of the GS energy parameter ε_0. Numbers in parenthesis denote the size of a cluster, N_q.

α	1/8	1/6	1/5	1/4	1/3
1.1	0.72056	0.68561 (24) 0.68318 (12)	0.65678	0.61291 (24) 0.61121 (16)	0.53553 (24) 0.53212 (12)
2.0	1.26734	1.18978 (24) 1.18937 (12)	1.12758	1.03384 (24) 1.03336 (16)	0.87689 (24) 0.87569 (12)

2.3.3 Results

To guarantee that our results reduce to the exact solution in the limit $h \to 0$, we mainly consider the region $\alpha \gtrsim 1$. The simplest degree of freedom, consisting of 4 spins, is shown in Fig. 2.7(a). Using this cluster in our HMF scheme one obtains stable plateaux only at $m = 1/2$ and $m = 1$. Clearly, larger blocks are necessary to stabilize plateaux at lower magnetization fractions. Here, we consider cluster sizes $N_q = 4k$ with $k = 2\ldots6$ and discuss only plateaux at 1/3, 1/4, 1/5, 1/6 and 1/8, supported in minimal clusters of $N_q = 12, 8, 20, 12$ and 16 spins, respectively ($M_{\text{sat}} = N_q/2$). In Fig. 2.7(b) we present local spin profiles corresponding to the lowest energy configurations for each of these fractions. Comparison of patterns for different plateaux shows that states $1/n$ with n even are characterized by one polarized dimer per unit cell, while cells of odd-n states have two triplons. For a given plateau there typically exist several possible coarse-graining scenarios, characterized by different clusters and tessellations of the SS lattice, but identical unit cells. Although these configurations have slightly different energies, their existence provides an important check for robustness of local correlations stabilizing the plateau states. The patterns for all fractions except 1/5 are similar to those obtained in [68, 76]. Strictly speaking, the profiles in Fig. 2.7(b) are well defined only for large values of $\alpha > 1$ and quickly smear out with decreasing α. This effect is difficult to capture within the effective model calculations, like [76].

A clear advantage of the HMF approach, compared to previous works, is its ability to compute GS energies of the *original* SS model. Within each plateau we have: $E_0(h)/N = -\varepsilon_0 - mh/2$. The parameter ε_0 is presented in Tab. 2.1 for some values of α and different cluster sizes. In order to address finite-size effects, in Fig. 2.7(c) we present the high magnetic field phase diagram of the SS model for $\alpha \geqslant 1$. All fractions were calculated using the largest possible cluster. Due to the insulating nature of the plateau states, the finite-size corrections are not expected to significantly affect their stability. For instance, for $m = 1/6$ the energy difference between 12- and 24-spin clusters is only $\sim 5\%$ of its width for the values of α shown in Tab. 2.1. This observation serves as additional evidence in favor of a universal physical mechanism leading to the plateaux.

The HMF method does not involve truncation of the dimer Hilbert space. In order to understand consequences of such approximation, we computed ε_0 for different plateaux, ignoring the dimer state $|\downarrow\downarrow\rangle$. The resulting absolute error is of the same order of magnitude as finite size effects and plateau widths (cf. Table 2.1), which leads to a sizable change in the relative stability of the plateaux. For example, at $\alpha = 1.1$ the average error is $3 \cdot 10^{-3} J$, and the lower boundary of the 1/8 state shifts by $0.04 J$. Therefore, conclusions of the effective boson model calculations, which employ a similar truncation, should generally be taken with caution.

2.3.4 Discussion

Although the effective model approach does yield a sequence of plateaux, their understanding remains incomplete. Our work addresses this issue by focusing on the nature and correlations of the magnetic plateau states. In particular, the analysis presented above allows the formulation of a set of *universal* rules leading to well-defined *spin patterns* (Fig. 2.7(b)), which can be probed, e.g. by polarized neutron scattering. These rules define a hierarchy of variational plateau wavefunctions and constitute a

central prediction of this work. For a robust state to emerge at a given magnetization fraction m, the *commensurability conditions* that have to be fulfilled are:

- A cluster degree of freedom must contain an even number of dimers;

- The SS lattice must be tessellated completely with these clusters;

- The size of the cluster (unit cell), N_q, must allow the plateau state at m, implying $N_q = 2M/m$ with $M = 1, \ldots, N_q/2$ chosen in a way such that N_q is divisible by four;

- Number of triplons (⬤━⬤) per cluster is M and its shape must be such that each triplon is surrounded by two dimers of the type ▬●, within this cluster.

Application of these constraints leaves us with an essentially combinatorial problem of actually determining the symmetry and periodicity of the spin superstructure.

There also exists a number of concrete discrepancies between our work and recent publications [76, 77], which nevertheless support our general conclusion regarding the local nature of the plateau states. First, the experimentally observed plateaux at $1/4$ and $1/8$, which we found to be quite robust, were claimed in [76] to be unstable. However, the magnetization profile presented in Fig. 2.7(b) for $m = 1/8$, which persists at $\alpha = 0.787$, adequate for $\mathrm{SrCu_2(BO_3)_2}$, is consistent with interpretation of the available NMR data [68, 69] for this material. We believe that the origin of these states is purely magnetic and no additional interactions beyond the SS model are required, in contradiction with the claim of [76]. Our results also yield a stable $1/5$ plateau, contrary to conclusions of Refs. [76, 77]. We note that this fraction was observed in torque measurements of [71], however, their proposed spin superlattice differs dramatically from the one predicted in our Fig. 2.7(b). Another distinction concerns the robustness of the $1/6$ plateau advocated in [76], which, although present in our calculation, has a significantly smaller relative width (see the discussion above).

Other fractions at 1/9, 2/9 and 2/15, observed in [76] and [77], can also be obtained within our approach, but this requires significantly larger clusters than the ones used here. By virtue of our commensurability arguments, we expect the plateaux at 1/9 and 2/9 to emerge in degrees of freedom containing at least 36 spins, while the 2/15 fraction will be stabilized in a 60-spin cluster.

Finally we note that the precise shape of the magnetization curve (the relative energy stability of different plateaux) is quite sensitive to the value of α (i.e. the particular compound) and, most importantly, since there is no exact solution of the SS model at high fields, it depends on a particular approximation scheme. Other physical interactions present in the real materials and not included in the SS model may also add to this uncertainty.

2.4 Non-frustrated systems: Phase diagram of the Heisenberg antiferromagnet with four-spin exchange interactions

In this section we study the quantum phase diagram of the square-lattice Heisenberg antiferromagnet with a subset of four-spin ring exchange interactions (the so-called *J-Q* model) using the HMF method, discussed in Sec. 2.2. It will be shown that the model exhibits a transition between a Néel state and a quantum paramagnetic phase characterized by broken translational invariance. This non-magnetic phase preserves the lattice rotational symmetry and has a correlated plaquette nature.

2.4.1 Introduction

The *J-Q* model describes a non-frustrated spin-1/2 antiferromagnet (AF) with multi-spin exchange interactions. This toy model was proposed by Sandvik in [52] and later

studied by other authors [78, 79] in an attempt to provide numerical support for the hypothesis of deconfined quantum criticality [48]. This theory, already mentioned in the Introduction to Sec. 2.2, predicts the existence of a class of systems whose critical behavior lies outside the scope of the Landau theory of phase transitions [49]. Critical points in these systems are characterized by the deconfinement of fractionalized excitations, parameterizing the original degrees of freedom (e.g. spins), which occurs right at the transition. It was observed that this scenario can in principle be realized in spin systems which exhibit a second-order phase transition point characterized by the simultaneous breakdown of a continuous (e.g. spin $SU(2)$) and a discrete (e.g. lattice) symmetries, in such a way that symmetry groups on opposite sides of the transition are not group-subgroup related. Such critical points cannot be described in the framework of Landau's theory. According to the Quantum Monte Carlo (QMC) simulations presented in [52, 78, 79], the phase transition in the J-Q model indeed is of the deconfined type.

The J-Q model is defined by the Hamiltonian:

$$H = J \sum_{\langle ij \rangle} \mathbf{S}_i \mathbf{S}_j - Q \sum_{\langle ijkl \rangle} \left(\mathbf{S}_i \mathbf{S}_j - \frac{1}{4} \right) \left(\mathbf{S}_k \mathbf{S}_l - \frac{1}{4} \right),$$

where J and $Q \geqslant 0$, indices $i, j, \ldots$ denote sites in a 2D square lattice and $\mathbf{S}_i$ are spin-1/2 operators. The first summation extends over bonds (nearest neighbor sites). The second term contains two sums over plaquettes (sites of the dual lattice): first, (ij) and (kl) denote parallel horizontal links of the plaquette, and then (ik) and (jl) correspond to parallel vertical bonds. It was concluded [52] that there exists a critical point at $Q_c/J \sim 25$ separating the antiferromagnetic phase from a valence-bond solid (VBS) state, whose nature is, strictly speaking, unclear [52] but the calculations suggested a columnar (dimer) order in this paramagnetic region.

In this section we study the phase diagram of the J-Q model using the HMF

technique. As we already mentioned in Sec. 2.2 this approach artificially breaks the lattice translational symmetry and introduces a non-physical correlation length, producing a gap in the low-energy excitation spectrum. In order to describe gapless Goldstone modes in an ordered state (e.g. magnons in the AF phase) one must include fluctuations around the HMF GS, as we demonstrated in the case of the J_1-J_2 model. However, the large-Q phase in the J-Q model is known to be gapped. Therefore, errors introduced by the HMF approximation should not lead to a severe underestimation of quantum fluctuations close to the phase transition point.

2.4.2 Coarse graining and HMF approximation

For our purposes it is convenient to separate the two and four spin terms in the J-Q Hamiltonian:

$$H = -\frac{2NQ}{16} + \left(J + \frac{Q}{2}\right)\sum_{\langle ij \rangle} \boldsymbol{S}_i \boldsymbol{S}_j - Q \sum_{\langle ijkl \rangle} (\boldsymbol{S}_i \boldsymbol{S}_j)(\boldsymbol{S}_k \boldsymbol{S}_l). \qquad (2.12)$$

A satisfactory coarse graining procedure should partition the lattice into spin clusters (containing N_q sites) that explicitly preserve symmetries of the problem. In particular, the J-Q Hamiltonian is invariant under $SU(2)$ rotations and transformations from the lattice point group C_{4v} [4]. Therefore, we will consider only symmetry preserving degrees of freedom: (i) plaquettes (2×2 spin clusters) and (ii) 4×4 blocks.

In the Schwinder boson representation, the J-Q model will have the form of Eq. (2.3) with the addition of the four-boson interactions, which correspond to the four-spin terms in (2.12):

$$H = \sum_i \left(H_\square\right)_{a'a} \gamma_{ia'}^\dagger \gamma_{ia} + \sum_{\langle ij \rangle} \left(H_{\text{int}}^2\right)_{a_1 a_2}^{a_1' a_2'} \gamma_{ia_1'}^\dagger \gamma_{ja_2'}^\dagger \gamma_{ia_1} \gamma_{ja_2} + \qquad (2.13)$$

$$+ \sum_{\langle i_1 i_2 i_3 i_4 \rangle_h} \left(H_{\text{int}}^{4h}\right)_{a_1 a_2; a_3 a_4}^{a_1' a_2'; a_3' a_4'} \prod_{\mu=1}^4 \gamma_{i_\mu a_\mu'}^\dagger \gamma_{i_\mu a_\mu} + \sum_{\langle i_1 i_2 i_3 i_4 \rangle_v} \left(H_{\text{int}}^{4v}\right)_{a_1 a_3; a_2 a_4}^{a_1' a_3'; a_2' a_4'} \prod_{\mu=1}^4 \gamma_{i_\mu a_\mu'}^\dagger \gamma_{i_\mu a_\mu},$$

where $a, a', \ldots$ label states in the Hilbert space of a cluster, $i, j, \ldots$ denote sites in the coarse grained lattice, and summations are assumed over all repeated indices. The two-body interaction H_{int}^2 is given by Eq. (2.2) with $\sigma = 1$. The last line describes the correlated four-boson scattering. The superscript h indicates that $i_1 i_2$ and $i_3 i_4$ are horizontal links of a plaquette, and similarly v denotes the case when $i_1 i_3$ and $i_2 i_4$ are vertical links of the same plaquette.

We will investigate the phase diagram of the J-Q model using the variational GS of Eq. (2.4). It is important to emphasize that although the coarse graining procedure preserves symmetries of the Hamiltonian (2.12), some of them can be spontaneously broken at the mean-field level as a result of self-consistency. In particular, the columnar dimer state is contained in the wavefunction (2.4) although it never appears as a stable solution.

We have explicitly separated the four-boson interaction in the Hamiltonian (2.13) into horizontal and vertical link contributions. This distinction is important because these two terms must be properly symmetrized to obey bosonic statistics. The term H_{int}^{4h} has to be symmetrized only with respect to indices in the same group, and groups as a whole (groups are separated by semicolons), i.e. one needs to take into account only the following permutations: $(1 \leftrightarrow 2)$, $(3 \leftrightarrow 4)$ and simultaneously $(1 \leftrightarrow 3, 2 \leftrightarrow 4)$. Analogously, in the term H_{int}^{4v} only the permutations $(1 \leftrightarrow 3)$, $(2 \leftrightarrow 4)$ and $(1 \leftrightarrow 2, 3 \leftrightarrow 4)$ should be accounted for.

The problem then reduces to minimization of the energy functional:

$$\frac{N E_0[R]}{N_q} = (H_\square)_{a'a} R_{a'} R_a + \left(H_{\text{int}}^2\right)_{a_1 a_2}^{a_1' a_2'} \prod_{\nu=1}^{2} R_{a_\nu'} R_{a_\nu} + \left(H_{\text{int}}^{4h} + H_{\text{int}}^{4v}\right)_{a_1 a_2; a_3 a_4}^{a_1' a_2'; a_3' a_4'} \prod_{\nu=1}^{4} R_{a_\nu'} R_{a_\nu}$$

$$(2.14)$$

under the constraint $R_a R_a = 1$, which leads to the self-consistent eigenvalue equation

$(H_{HF})_{ab} R_b = \mu R_a$ with the Hartree-Fock Hamiltonian:

$$\left(H_{HF}\right)_{ab} = \left(H_\square\right)_{ab} + 2\left(H_{\text{int}}^2\right)_{a_1 a}^{a_1' b} R_{a_1'} R_{a_1} + 4\left(H_{\text{int}}^{4h} + H_{\text{int}}^{4v}\right)_{a_1 a_2 a_3 a}^{a_1' a_2' a_3' b} \prod_{\mu=1}^{3} R_{a_\mu'} R_{a_\mu}.$$

Once the amplitude R_a is determined, the ground state energy (GSE) can be computed using Eq. (2.14). Besides the GSE we will also be interested in computing the staggered magnetization M_z (see first line in Eq. (2.8)), and the two-component VBS "order parameter" [80]:

$$\text{Re}\Psi = \frac{1}{N}\sum_{\boldsymbol{x}}(-1)^x \boldsymbol{S}_{\boldsymbol{x}+\boldsymbol{e}_x}\boldsymbol{S}_{\boldsymbol{x}}; \quad \text{Im}\Psi = \frac{1}{N}\sum_{\boldsymbol{x}}(-1)^y \boldsymbol{S}_{\boldsymbol{x}+\boldsymbol{e}_y}\boldsymbol{S}_{\boldsymbol{x}},$$

which allows us to characterize point symmetries of a state.

In the rest of this section we will sketch the HMF calculation of E_0, M_z and Ψ for the case of plaquettes, and only present final expressions for the 4×4 clusters. For details regarding this latter case see Sec. 2.2 and Appendices A and B at the end of this chapter. From now on we shall put $J \equiv 1$.

(i) The plaquette degree of freedom

We start by considering the simplest way to cover the lattice – with plaquettes, as shown in Fig. 2.8(a).The Hamiltonian for an isolated plaquette has the form:

$$H_\square = \left(1 + \frac{Q}{2}\right)(\boldsymbol{S}_1 + \boldsymbol{S}_4)(\boldsymbol{S}_2 + \boldsymbol{S}_3) - Q\left[(\boldsymbol{S}_1\boldsymbol{S}_2)(\boldsymbol{S}_3\boldsymbol{S}_4) + (\boldsymbol{S}_1\boldsymbol{S}_3)(\boldsymbol{S}_2\boldsymbol{S}_4)\right]. \quad (2.15)$$

The interaction of this plaquette with the rest of the system can be conveniently partitioned according to (2.13) as: $H_{\text{int}} = H_{\text{int}}^2 + H_{\text{int}}^{4h} + H_{\text{int}}^{4v}$, where appropriately
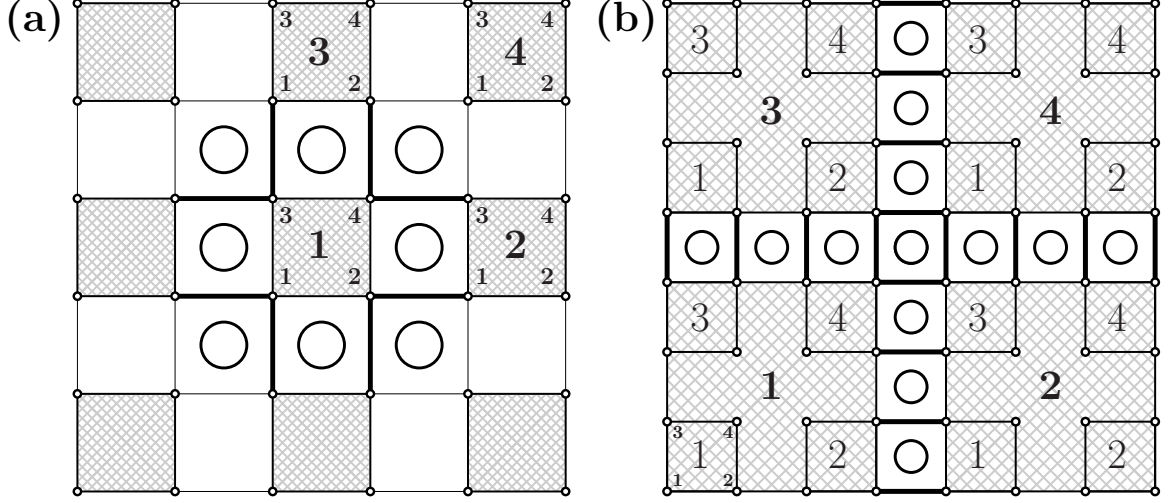
Figure 2.8: (a) The plaquette lattice. Thick lines denote interactions $J + Q/2$. The circles indicate four-spin terms of strength Q in the Hamiltonian (2.12). Small-sized numbers label spins within a plaquette, while the larger ones label plaquettes. (b) Connectivity of the lattice formed by 4×4 spin clusters. Small circles indicate spins. Bold numbers label the 4×4 clusters, while thin ones denote plaquettes.

symmetrized individual terms are given by:

$$
H_{\text{int}}^2 = \frac{1 + Q/2}{2} \big[(\boldsymbol{S}_{11} + \boldsymbol{S}_{14})(\boldsymbol{S}_{22} + \boldsymbol{S}_{23}) + (\boldsymbol{S}_{12} + \boldsymbol{S}_{13})(\boldsymbol{S}_{21} + \boldsymbol{S}_{24}) \big] -
$$
$$
- \frac{Q}{2} \big[(\boldsymbol{S}_{11}\boldsymbol{S}_{12})(\boldsymbol{S}_{23}\boldsymbol{S}_{24}) + (\boldsymbol{S}_{11}\boldsymbol{S}_{23})(\boldsymbol{S}_{12}\boldsymbol{S}_{24}) + (\boldsymbol{S}_{12}\boldsymbol{S}_{14})(\boldsymbol{S}_{21}\boldsymbol{S}_{23}) +
$$
$$
+ (\boldsymbol{S}_{12}\boldsymbol{S}_{21})(\boldsymbol{S}_{14}\boldsymbol{S}_{23}) + (\boldsymbol{S}_{13}\boldsymbol{S}_{14})(\boldsymbol{S}_{21}\boldsymbol{S}_{22}) + (\boldsymbol{S}_{13}\boldsymbol{S}_{21})(\boldsymbol{S}_{14}\boldsymbol{S}_{22}) +
$$
$$
+ (\boldsymbol{S}_{11}\boldsymbol{S}_{22})(\boldsymbol{S}_{13}\boldsymbol{S}_{24}) + (\boldsymbol{S}_{11}\boldsymbol{S}_{13})(\boldsymbol{S}_{22}\boldsymbol{S}_{24}) \big]
$$

and

$$
H_{\text{int}}^{4h} = - \frac{Q}{8} \big[(\boldsymbol{S}_{14}\boldsymbol{S}_{23} + \boldsymbol{S}_{24}\boldsymbol{S}_{13})(\boldsymbol{S}_{32}\boldsymbol{S}_{41} + \boldsymbol{S}_{31}\boldsymbol{S}_{42}) +
$$
$$
+ (\boldsymbol{S}_{34}\boldsymbol{S}_{43} + \boldsymbol{S}_{44}\boldsymbol{S}_{33})(\boldsymbol{S}_{12}\boldsymbol{S}_{21} + \boldsymbol{S}_{11}\boldsymbol{S}_{22}) \big];
$$
$$
H_{\text{int}}^{4v} = - \frac{Q}{8} \big[(\boldsymbol{S}_{14}\boldsymbol{S}_{32} + \boldsymbol{S}_{12}\boldsymbol{S}_{34})(\boldsymbol{S}_{23}\boldsymbol{S}_{41} + \boldsymbol{S}_{21}\boldsymbol{S}_{43}) +
$$
$$
+ (\boldsymbol{S}_{24}\boldsymbol{S}_{42} + \boldsymbol{S}_{22}\boldsymbol{S}_{44})(\boldsymbol{S}_{13}\boldsymbol{S}_{31} + \boldsymbol{S}_{11}\boldsymbol{S}_{33}) \big].
$$
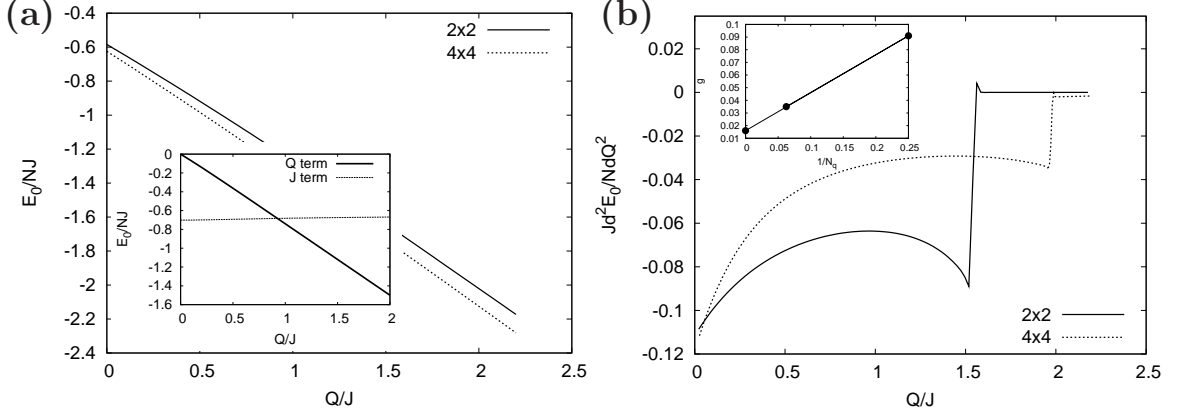
Figure 2.9: (a) Main panel: GSE as a function of Q/J for plaquettes [case (i)] and 4×4 spin clusters [case (ii)]. Inset: contributions to the GSE from the J and Q terms in (2.12) for a 4×4 spin cluster with periodic boundary conditions; the unimportant term $-NQ/8$ is omitted. (b) Second-order derivative $d^2 E_0/NdQ^2$ (main panel) as a function of Q/J for cases (i) and (ii). The discontinuity at $Q/J \sim 1.61$ (2×2) and $Q/J \sim 2.0$ (4×4) indicates a second-order phase transition point. The inset shows the extrapolation of the jump $g = Jd^2 E_0/NdQ^2|_{Q_c-0}^{Q_c+0}$ to $N_q \to \infty$.

It is convenient to work in the basis which diagonalizes the Q-independent part of $H_\square$ in Eq. (2.15) as done in Sec. 2.2. The matrix elements, which appear in Eq. (2.14),

$$\left(H_{\text{int}}^2\right)_{a_1 a_2}^{a_1' a_2'} \equiv \langle a_1' a_2' | H_{\text{int}}^2 | a_1 a_2 \rangle; \quad \left(H_{\text{int}}^{4h,v}\right)_{a_1 a_2; a_3 a_4}^{a_1' a_2'; a_3' a_4'} \equiv \langle a_1' a_2'; a_3' a_4' | H_{\text{int}}^{4h,v} | a_1 a_2; a_3 a_4 \rangle,$$

can now be computed using the angular momentum addition theorems. The staggered magnetization (along the z-axis) within a plaquette can be computed using Eq. (2.7), while the function Ψ can be written in the plaquette representation as:

$$\text{Re}\Psi = \frac{1}{N} \sum_i \left[\boldsymbol{S}_{i1}\boldsymbol{S}_{i2} + \boldsymbol{S}_{i3}\boldsymbol{S}_{i4} \right] - \frac{1}{N} \sum_i \left[\boldsymbol{S}_{i2}\boldsymbol{S}_{i+\hat{x},1} + \boldsymbol{S}_{i4}\boldsymbol{S}_{i+\hat{x},3} \right]; \quad (2.16)$$

$$\text{Im}\Psi = \frac{1}{N} \sum_i \left[\boldsymbol{S}_{i1}\boldsymbol{S}_{i3} + \boldsymbol{S}_{i2}\boldsymbol{S}_{i4} \right] - \frac{1}{N} \sum_i \left[\boldsymbol{S}_{i3}\boldsymbol{S}_{i+\hat{y},1} + \boldsymbol{S}_{i4}\boldsymbol{S}_{i+\hat{y},2} \right].$$

In these equations indices i and $\hat{x}$ denote sites and basis vectors of the plaquette lattice.

(ii) 4×4 spin clusters

The coarse grained lattice obtained by choosing the 4×4 cluster as a degree of freedom is shown in Fig. 2.8(b). Each spin operator carries three indices: label of a cluster, label of a plaquette within this cluster, and the position within this plaquette. Writing down the cluster self-energy and the inter-cluster interactions is a straightforward but tedious task, which can be accomplished along the lines presented in the previous subsection. Here we give only the final expression for Ψ; spin expectation values, necessary for the staggered magnetization, are presented in Appendix A. The function Ψ can be written as:

$$
\begin{aligned}
\mathrm{Re}\Psi = & \frac{1}{N}\sum_i \big(\boldsymbol{S}_{i11}\boldsymbol{S}_{i12} + \boldsymbol{S}_{i13}\boldsymbol{S}_{i14} + \boldsymbol{S}_{i31}\boldsymbol{S}_{i32} + \boldsymbol{S}_{i33}\boldsymbol{S}_{i34} + \boldsymbol{S}_{i21}\boldsymbol{S}_{i22} + \boldsymbol{S}_{i23}\boldsymbol{S}_{i24} + \\
& + \boldsymbol{S}_{i41}\boldsymbol{S}_{i42} + \boldsymbol{S}_{i43}\boldsymbol{S}_{i44} - \boldsymbol{S}_{i12}\boldsymbol{S}_{i21} - \boldsymbol{S}_{i14}\boldsymbol{S}_{i23} - \boldsymbol{S}_{i32}\boldsymbol{S}_{i41} - \boldsymbol{S}_{i34}\boldsymbol{S}_{i43}\big) - \\
& - \frac{1}{N}\sum_i \big[\boldsymbol{S}_{i22}\boldsymbol{S}_{i+\hat{x},11} + \boldsymbol{S}_{i24}\boldsymbol{S}_{i+\hat{x},13} + \boldsymbol{S}_{i42}\boldsymbol{S}_{i+\hat{x},31} + \boldsymbol{S}_{i44}\boldsymbol{S}_{i+\hat{x},33}\big]; \quad\quad (2.17) \\
\mathrm{Im}\Psi = & \frac{1}{N}\sum_i \big(\boldsymbol{S}_{i11}\boldsymbol{S}_{i13} + \boldsymbol{S}_{i12}\boldsymbol{S}_{i14} + \boldsymbol{S}_{i21}\boldsymbol{S}_{i23} + \boldsymbol{S}_{i22}\boldsymbol{S}_{i24} + \boldsymbol{S}_{i31}\boldsymbol{S}_{i33} + \boldsymbol{S}_{i32}\boldsymbol{S}_{i34} + \\
& + \boldsymbol{S}_{i41}\boldsymbol{S}_{i43} + \boldsymbol{S}_{i42}\boldsymbol{S}_{i44} - \boldsymbol{S}_{i13}\boldsymbol{S}_{i31} - \boldsymbol{S}_{i14}\boldsymbol{S}_{i32} - \boldsymbol{S}_{i23}\boldsymbol{S}_{i41} - \boldsymbol{S}_{i24}\boldsymbol{S}_{i42}\big) - \\
& - \frac{1}{N}\sum_i \big[\boldsymbol{S}_{i33}\boldsymbol{S}_{i+\hat{y},11} + \boldsymbol{S}_{i34}\boldsymbol{S}_{i+\hat{y},12} + \boldsymbol{S}_{i43}\boldsymbol{S}_{i+\hat{y},21} + \boldsymbol{S}_{i44}\boldsymbol{S}_{i+\hat{y},22}\big].
\end{aligned}
$$

2.4.3 Results

We can now proceed with solution of the HMF equations. The physical quantities that we want to compute in the first place are the GSE and the staggered magnetization. In Fig. 2.9(a) we present GSE for both cluster sizes considered above. All energies monotonically decrease with increasing Q/J as a consequence of the negative sign in front of the last term in Eq. (2.12). At some critical value of $Q = Q_c$ the system undergoes a phase transition from the Néel state at small Q to a spin-disordered state at $Q > Q_c$. This transition can be seen either from the second derivative of the GSE,
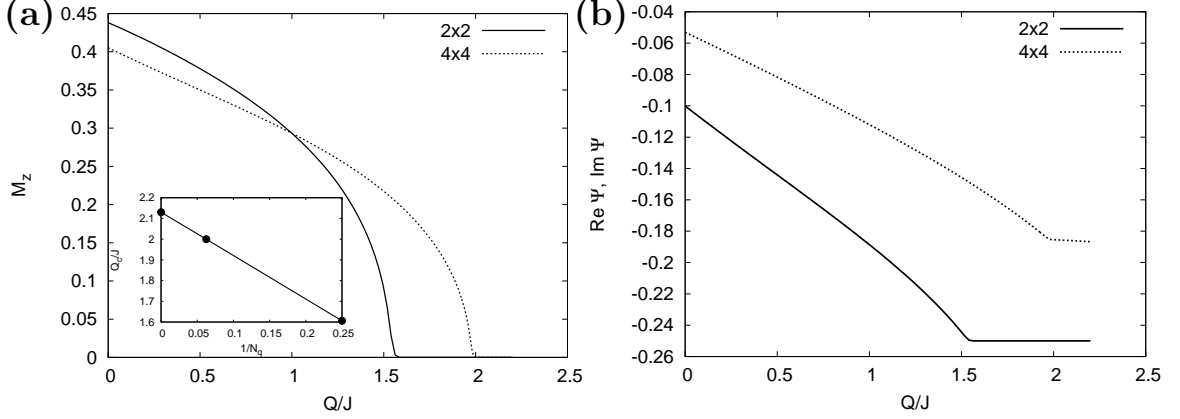
Figure 2.10: (a) Staggered magnetization (main panel) as a function of Q/J. The values of Q_c are: $Q_c/J = 1.61$ for case (i) and $Q_c/J = 2.00$ for case (ii). The inset shows the scaling of Q_c. (b) The "order parameter" Ψ for the two cases, studied in this paper. Notice the coincidence of curves for ReΨ and ImΨ. For $Q \geqslant Q_c$ this implies the plaquette nature of the quantum paramagnetic state.

d^2E_0/NdQ^2 (shown in Fig. 2.9(b)) or from the staggered magnetization as a function of Q/J (presented in Fig. 2.10(a)). Using these plots one obtains the numerical values $Q_c/J = 1.61$ for plaquettes and $Q_c/J = 2.00$ for 4×4 clusters. Although the jump $g = Jd^2E_0/NdQ^2|_{Q_c-0}^{Q_c+0}$ is numerically small, it remains finite: $g \to 0.016$, if extrapolated to the thermodynamic limit, based on these two points (see the inset to Fig. 2.9(b)). The finite-size scaling of the critical point itself, presented in the inset in Fig. 2.10(a), shows that $\lim_{N_q \to \infty} Q_c/J = 2.13$. We note that due to few data points, the finite-size scalings presented here are qualitative, and are intended to provide only an estimate for the extrapolated quantities in the thermodynamic limit.

Let us now discuss the symmetries of the various phases. The AF state, which occurs for $Q < Q_c$, is known to preserve the lattice rotational symmetry C_4, and spontaneously breaks the spin $SU(2)$ symmetry. The nature of the paramagnetic phase stabilized for $Q \geqslant Q_c$ can be unveiled by computing expectation values of the function Ψ given by Eqs. (2.16) and (2.17) for cases (i) and (ii), respectively. Although Ψ is an integral quantity, it is sufficient for the purpose of discriminating between

plaquettized and dimerized ground states. Namely, a plaquette phase preserves the four-fold lattice rotational symmetry, meaning that

$$\mathrm{Re}\Psi = \mathrm{Im}\Psi, \tag{2.18}$$

while in a dimerized state this equality does not hold. In Fig. 2.10(b) we present plots of $\mathrm{Re}\Psi$ and $\mathrm{Im}\Psi$. The equality (2.18) is satisfied throughout the phase diagram. This fact is not surprising in the antiferromagnetic phase, but in the paramagnetic region it presents a strong evidence against any type of dimerized ground states. Although such states were allowed in the process of minimization, the C_4-symmetric states always had lower energy. In fact, the ground state in the non-magnetic region is a plaquette paramagnet, with each plaquette being in its singlet ground state. However, due to the tensor nature of interactions in (2.12) these plaquettes are coupled, contrary to the case of the J_1-J_2 model. Finally we note that extrapolation to $N_q \to \infty$ shows that $\mathrm{Re}\Psi, \mathrm{Im}\Psi \to -0.04$, suggesting that the lattice translational invariance is being recovered in the thermodynamic limit.

2.4.4 Discussion

In agreement with previous works [52, 78, 79] our calculations demonstrate that the Hamiltonian (2.12) exhibits a phase transition point separating the Néel-ordered state from a paramagnetic phase with broken translational invariance. Besides establishing the existence of a phase transition, we were also able to unveil the nature of the paramagnetic phase and show that a *correlated plaquette state* is favored over a columnar dimer state which, although not conclusively, seems to be preferred in previous calculations [52]. These findings are summarized in the $J > 0$ part in Fig. 2.11.

However, despite qualitative agreement, there is a quantitative discrepancy in the
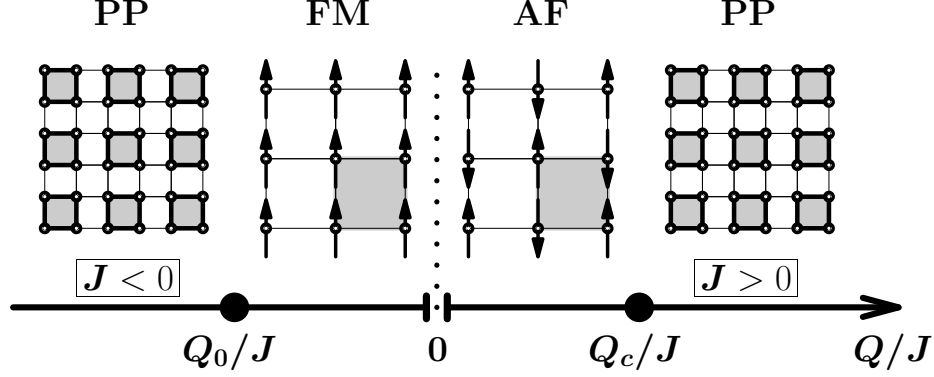
Figure 2.11: HMF phase diagram of the J-Q model. The AF phase with broken $SU(2)$ symmetry and the singlet paramagnetic state are separated by a second-order quantum phase transition at $Q_c/J \approx 2$. The point $Q_0/J \approx -1.3$ indicates a first-order transition between the FM and singlet phases. The non-magnetic phase breaks the lattice translational symmetry and is a *plaquette paramagnet* (PP). The PP regions at $J < 0$ and $J > 0$ are adiabatically connected by changing J (Q/J) through zero (infinity), i.e. there is no direct FM-to-AF transition.

numerical value of Q_c. The value obtained in the present paper, $Q_c/J \sim 2$ is much smaller than the one presented in [52] ($Q_c/J \sim 25$). Although we cannot provide a rigorous explanation for this discrepancy, we would like to make the following qualitative remark to support our result. The variational wavefunction (2.4), physically being a low-density ansatz, generally leads to an underestimation of the four-boson scattering terms in Eq. (2.13). In order to understand how significant this error is and check that the results presented in Figs. 2.9 and 2.10 are reasonable, we used data from the exact diagonalization of 4×4 spin clusters to compare magnitudes of the terms proportional to J and Q, in Eq. (2.12). On physical grounds one would expect a phase transition to occur when these terms become comparable. The inset in Fig. 2.9(a) presents the two contributions and their dependence on Q/J. Of course, the crossing point at $Q/J \sim 1$ does not determine the critical value Q_c, but it provides a clue on where the phase transition may occur. Since the system is gapped in the paramagnetic phase, one can argue that the size 4×4 is large enough to describe the thermodynamic limit. Indeed, QMC data for $Q/J = 10$ indicates that the GSE

converges very rapidly with increasing system size [81]. Also, QMC calculations, performed [81] for systems up to 16×16 sites, indicate that the magnitude of the above crossing point stays of order unity, even for large system sizes.

Our conclusions raise another important question regarding the nature of the phase transition. We find it to be of the Landau type. Although finite-size scaling of the GSE second derivative displays a finite jump as $N_q \rightarrow \infty$, there is no way to rigorously prove that it remains finite in the thermodynamic limit. Thus, the possibility of a first order transition at Q_c (claimed in [82]) cannot be completely excluded.

So far we have studied the physically interesting AF case $J > 0$. However, the ferromagnetic (FM) situation ($J < 0$) can be handled in complete analogy. The quantum phase transition, separating the FM and singlet phases is first-order – it manifests itself as a crossing of GSE of the two phases – and occurs[3] at $Q_0/J \approx -1.3$. Thus, the paramagnetic phase displays *two* instabilities, ferro- and antiferromagnetic. The complete phase diagram of the J-Q model is shown in Fig. 2.11.

2.5   Appendix A: Superplaquette degree of freedom for the J_1-J_2 model

In this Appendix we present details of the HMF calculation which uses the 4×4 superplaquette (shown in Fig. 2.12) as an elementary degree of freedom. It turns out that the full angular momentum basis is inconvenient, so we use the 2×2 plaquette product states in order to perform the mean-field calculations. Each spin is charac-

---

[3]Because this transition is first-order, its location is only weakly sensitive to the system size. The values of the transition point, Q_0, obtained from exact diagonalization (ED) and HMF agree very well:

Q_0/J	2×2	4×4
ED	-1.0	-1.19
HMF	-1.32	-1.26

terized by two indices: the plaquette number $i = 1 \ldots 4$ and an index $n = 1 \ldots 4$, which specifies a vertex in the plaquette. The $M = 0$ sector of the superplaquette Hilbert space is spanned by the states:

$$|A\rangle = \prod_{i=1}^{4}{}' |a_i\rangle,$$

where prime indicates the constraint $\sum_{i=1}^{4} M_i = 0$. Using these states, we can write down matrix elements, like $\langle a'_1 \ldots a'_4 | \boldsymbol{S}_{in} \boldsymbol{S}_{jn'} | a_1 \ldots a_4 \rangle$, in the compact form:

$$\langle A' | \boldsymbol{S}_{in} \boldsymbol{S}_{jn'} | A \rangle = \left(\sigma_{nn'}\right)^{a'_i a'_j}_{a_i a_j} \prod_{l \neq i,j} \delta_{a'_l a_l} \qquad (2.19)$$

with the symmetric matrices $\left(\sigma_{nm}\right)^{a'_i a'_j}_{a_i a_j} = \left(\sigma_{mn}\right)^{a'_j a'_i}_{a_j a_i} = \left(\sigma_{nm}\right)^{a_i a_j}_{a'_i a'_j}$ defined as:

$$\left(\sigma_{nn'}\right)^{a'_i a'_j}_{a_i a_j} = \sum_{K,M} (-1)^{L_i + L'_j + K} \langle L'_i M'_i L'_j M'_j | L'_i L'_j K M \rangle \langle L_i M_i L_j M_j | L_i L_j K M \rangle \times$$

$$\times \begin{Bmatrix} L'_i & L'_j & K \\ L_j & L_i & 1 \end{Bmatrix} \langle \lambda'_i \| S_n \| \lambda_i \rangle \langle \lambda'_j \| S_{n'} \| \lambda_j \rangle,$$

The Hamiltonian of a single superplaquette consists of two parts: a diagonal one involving only 2×2 plaquette contributions, and a non-diagonal part which accounts for the plaquette interactions. The former is written down straightforwardly as a matrix:

$$\left(H_{\mathrm{d}}\right)_{A'A} = \prod_i \delta_{a'_i a_i} \sum_i \epsilon_{a_i},$$

where ϵ_a is the plaquette self-energy, Eq. (2.1). The non-diagonal part has the

66

operator form:

$$H_{\mathrm{nd}} = J_1\big[(\boldsymbol{S}_{14} + \boldsymbol{S}_{41})(\boldsymbol{S}_{23} + \boldsymbol{S}_{32}) + \boldsymbol{S}_{12}\boldsymbol{S}_{21} + \boldsymbol{S}_{13}\boldsymbol{S}_{31} + \boldsymbol{S}_{34}\boldsymbol{S}_{43} + \boldsymbol{S}_{24}\boldsymbol{S}_{42}\big] +$$

$$+ J_2\big[\boldsymbol{S}_{12}\boldsymbol{S}_{23} + \boldsymbol{S}_{14}\boldsymbol{S}_{21} + \boldsymbol{S}_{23}\boldsymbol{S}_{42} + \boldsymbol{S}_{41}\boldsymbol{S}_{24} + \boldsymbol{S}_{34}\boldsymbol{S}_{41} + \boldsymbol{S}_{32}\boldsymbol{S}_{43} +$$

$$+ \boldsymbol{S}_{31}\boldsymbol{S}_{14} + \boldsymbol{S}_{13}\boldsymbol{S}_{32} + \boldsymbol{S}_{14}\boldsymbol{S}_{41} + \boldsymbol{S}_{32}\boldsymbol{S}_{23}\big].$$

Let us now proceed with the plaquette interaction terms. Each superplaquette has 4 nearest and 4 next-nearest neighbors. Within each neighboring superplaquette we enumerate 2×2 plaquettes by the indices 5, 6, 7, 8, so that $1 \to 5$, $2 \to 6$, $3 \to 7$ and $4 \to 8$. Enumeration of vertices within a plaquette stays the same. In this manner we have the symmetrized NN,

$$H_1 = \frac{J_1}{4}\big[\boldsymbol{S}_{11}(\boldsymbol{S}_{73} + \boldsymbol{S}_{62}) + \boldsymbol{S}_{12}\boldsymbol{S}_{74} + \boldsymbol{S}_{13}\boldsymbol{S}_{64} + \boldsymbol{S}_{31}\boldsymbol{S}_{82} + \boldsymbol{S}_{34}\boldsymbol{S}_{52} + \boldsymbol{S}_{33}(\boldsymbol{S}_{84} + \boldsymbol{S}_{51}) +$$

$$+ \boldsymbol{S}_{21}\boldsymbol{S}_{83} + \boldsymbol{S}_{24}\boldsymbol{S}_{53} + \boldsymbol{S}_{22}(\boldsymbol{S}_{84} + \boldsymbol{S}_{51}) + \boldsymbol{S}_{43}\boldsymbol{S}_{61} + \boldsymbol{S}_{42}\boldsymbol{S}_{71} + \boldsymbol{S}_{44}(\boldsymbol{S}_{73} + \boldsymbol{S}_{62})\big] +$$

$$+ \frac{J_2}{4}\big[\boldsymbol{S}_{11}(\boldsymbol{S}_{74} + \boldsymbol{S}_{64}) + \boldsymbol{S}_{12}(\boldsymbol{S}_{73} + \boldsymbol{S}_{83}) + \boldsymbol{S}_{13}(\boldsymbol{S}_{62} + \boldsymbol{S}_{82}) + \boldsymbol{S}_{21}(\boldsymbol{S}_{74} + \boldsymbol{S}_{84})$$

$$+ \boldsymbol{S}_{22}(\boldsymbol{S}_{53} + \boldsymbol{S}_{83}) + \boldsymbol{S}_{24}(\boldsymbol{S}_{51} + \boldsymbol{S}_{71}) + \boldsymbol{S}_{31}(\boldsymbol{S}_{84} + \boldsymbol{S}_{64}) + \boldsymbol{S}_{33}(\boldsymbol{S}_{82} + \boldsymbol{S}_{52}) +$$

$$+ \boldsymbol{S}_{34}(\boldsymbol{S}_{51} + \boldsymbol{S}_{61}) + \boldsymbol{S}_{42}(\boldsymbol{S}_{73} + \boldsymbol{S}_{53}) + \boldsymbol{S}_{43}(\boldsymbol{S}_{62} + \boldsymbol{S}_{52}) + \boldsymbol{S}_{44}(\boldsymbol{S}_{71} + \boldsymbol{S}_{61})\big],$$

and NNN,

$$H_2 = \frac{J_2}{4}\big[\boldsymbol{S}_{11}\boldsymbol{S}_{84} + \boldsymbol{S}_{22}\boldsymbol{S}_{73} + \boldsymbol{S}_{33}\boldsymbol{S}_{62} + \boldsymbol{S}_{44}\boldsymbol{S}_{51}\big],$$

superplaquette interactions. Using Eq. (2.19), one can easily construct matrix elements of H_{nd} and $H_{1,2}$, which are required to obtain the HF equation of the type (2.5).

Having computed the single-superplaquette ground state wavefunction $R_A^0 =$
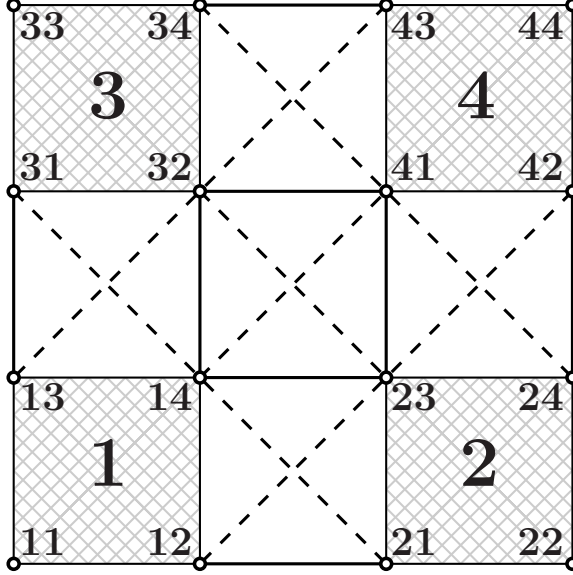
Figure 2.12: The 4×4 superplaquette degree of freedom. Each spin carries two indices: a 2×2 plaquette number and a coordinate within this plaquette.

$R^0_{a_1 a_2 a_3 a_4}$, we can use it to determine the spin polarizations:

$$\langle \text{HF}|S^z_{1n}|\text{HF}\rangle = \left(S^z_n\right)_{a'_1 a_1} R^0_{a'_1 a_2 a_3 a_4} R^0_{a_1 a_2 a_3 a_4};$$

$$\vdots$$

$$\langle \text{HF}|S^z_{4n}|\text{HF}\rangle = \left(S^z_n\right)_{a'_4 a_4} R^0_{a_1 a_2 a_3 a'_4} R^0_{a_1 a_2 a_3 a_4},$$

where $\left(S^z_n\right)_{a'a}$ is given by Eq. (2.7).

2.6 Appendix B: Fluctuation corrections to HMF theory of the J_1-J_2 model

In this Appendix we discuss fluctuation corrections to the HMF theory presented in Sec. 2.2. A natural way to achieve this goal is to perform a superfluid-type mean-field approximation. As a result one can obtain the collective spectrum and corrections to the GSE and magnetization. The structure of the superfluid mean-field is similar

to the Fetter-Bogoliubov approach to inhomogeneous Bose liquids [59]. Although we shall present results only for the 2×2 plaquette degree of freedom, it can equally be applied to the 4×4 superplaquette case.

2.6.1 General formulation

Let us return to the original Schwinger boson Hamiltonian (2.3) and explicitly separate out the condensate mode in the γ_{ia}-operators: $\gamma_{ia} = g_a + \beta_{ia}$. The condensation will occur in a certain superposition of the single-plaquette states. The real-valued multiplet g_a plays the role of a condensate wavefunction (CWF) [59]. Here it is chosen to be spatially homogeneous, but inhomogeneous phases can also be included. The CWF is normalized to the condensate fraction $\sum_a g_a^2 = n_0$. The non-condensate bosonic operators β_{ia} describe fluctuation corrections to the HF solution. If they are neglected we naturally return to the results of Sec. 2.2.

The superfluid mean-field approximation amounts to enforcing the Schwinger boson constraint on average:

$$n_0 + \frac{1}{N_\square} \sum_{i,a} \langle \beta_{ia}^\dagger \beta_{ia} \rangle = 1,$$

neglecting fluctuations in the condensate channel, and retaining only terms quadratic in β in the Hamiltonian (2.3):

$$H = N_\square \left[\frac{1}{2} \left(\mu n_0 + \sum_a \epsilon_a g_a^2 \right) - \mu n_0 \right] + \tag{2.20}$$

$$+ \sum_{i,a} (\epsilon_a - \mu) \beta_{ia}^\dagger \beta_{ia} + 4 \sum_{i,\sigma} \left(H_{\text{int}}^\sigma \right)_{a_1 a_2}^{a_1' a_2'} g_{a_2'} g_{a_2} \beta_{ia_1'}^\dagger \beta_{ia_1} +$$

$$+ \sum_{\sigma, \langle ij \rangle_\sigma} \left(H_{\text{int}}^\sigma \right)_{a_1 a_2}^{a_1' a_2'} \left[g_{a_1'} g_{a_2'} (\beta_{ia_1}^\dagger \beta_{ja_2}^\dagger + \beta_{ia_1} \beta_{ja_2}) + 2 g_{a_1} g_{a_2'} \beta_{ia_1'}^\dagger \beta_{ja_2} \right],$$

where $\langle ij \rangle_\sigma$ is defined after Eq. (2.3) and matrix elements of H_{int}^σ are given by Eq.
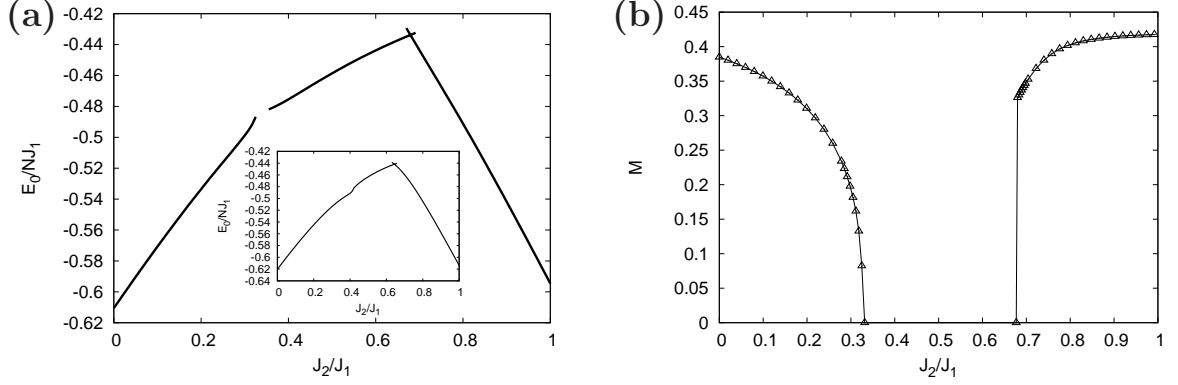
Figure 2.13: (a) Ground state energy for the self-consistent solution (main panel) and after the first iteration (inset). The absence of points in the main panel around J_2^{c1} is due to bad convergence in the simulation. (b) Self-consistently computed staggered magnetization, M_{stag}, for $J_2 \leq J_2^{c1}$ and columnar magnetization along the x-direction, $M_{\text{col}}(x)$, for $J_2 \geq J_2^{c2}$.

(2.2).

The CWF g_a is determined by the HF equation (2.5) with ε_n replaced with the chemical potential μ (the Gross-Pitaevskii equation). Eq. (2.5) defines the chemical potential[4] and guarantees the disappearance of linear terms in β from the Hamiltonian of Eq. (2.20). Quadratic terms in Eq. (2.20) represent fluctuation corrections to the HF results and constitute the focus of our analysis below.

The next step is to transform the quadratic part (H_2) of the Hamiltonian in Eq. (2.20) into momentum space:

$$H_2 = \sum_{\boldsymbol{k},a}(\epsilon_a - \mu)\beta_{\boldsymbol{k}a}^\dagger \beta_{\boldsymbol{k}a} + \sum_{\boldsymbol{k},\sigma}\left(H_{\text{int}}^\sigma\right)_{a_1 a_2}^{a_1' a_2'}\big\{\Theta_{\boldsymbol{k}}^\sigma\big[g_{a_1'}g_{a_2'}\big(\beta_{\boldsymbol{k}a_1}^\dagger \beta_{-\boldsymbol{k}a_2}^\dagger + \beta_{\boldsymbol{k}a_1}\beta_{\boldsymbol{k}a_2}\big)+$$

$$+ 2g_{a_1}g_{a_2'}\beta_{\boldsymbol{k}a_1'}^\dagger \beta_{\boldsymbol{k}a_2}\big] + 4g_{a_2'}g_{a_2}\beta_{\boldsymbol{k}a_1'}^\dagger \beta_{\boldsymbol{k}a_1}\big\},$$

where $\Theta_{\boldsymbol{k}}^\sigma = (\cos k_x + \cos k_y, 2\cos k_x \cos k_y)$ and $\boldsymbol{k}$ is defined within the plaquette Brillouin zone (i.e. there are $N_\square$ $\boldsymbol{k}$-states). This Hamiltonian can be diagonalized by

---

[4]It is clear that when $n_0 = 1$, $g_a = R_a^0$ and $\mu = \varepsilon_0$.
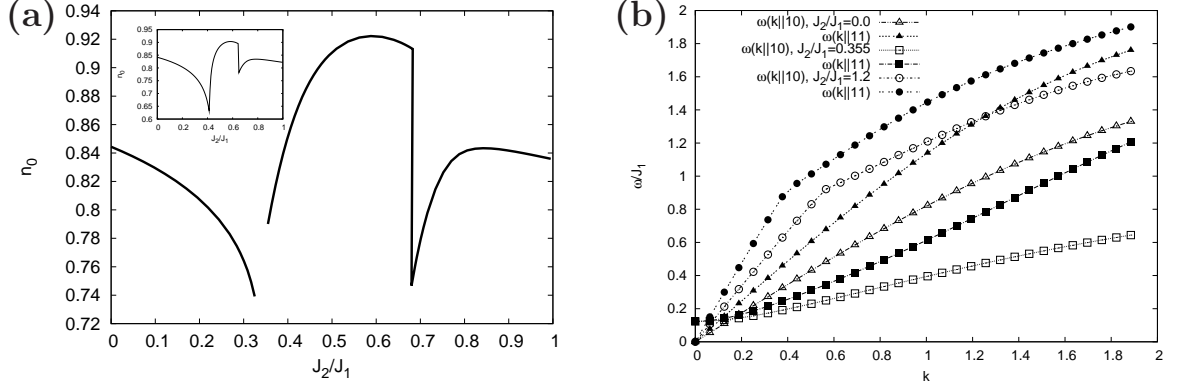
Figure 2.14: (a) Condensate fraction for the self-consistent solution (main panel) and after the first iteration (inset). Notice the shift of quantum phase transition points $J_2^{c1,2}$. (b) The lowest excitation branch $\omega_1(\boldsymbol{k})$ along the [10] and [11] directions in the plaquette Brillouin zone, for three values of J_2/J_1 chosen in different phases.

the Bogoliubov transformation:

$$\alpha_{\boldsymbol{k}\nu} = \sum_a \left(u_{\boldsymbol{k}a}^\nu \beta_{\boldsymbol{k}a} - v_{\boldsymbol{k}a}^\nu \beta_{-\boldsymbol{k}a}^\dagger\right); \quad \alpha_{-\boldsymbol{k}\nu}^\dagger = \sum_a \left(-v_{\boldsymbol{k}a}^\nu \beta_{\boldsymbol{k}a} + u_{\boldsymbol{k}a}^\nu \beta_{-\boldsymbol{k}a}^\dagger\right),$$

to a new set of bosonic operators $\alpha_{\boldsymbol{k}\nu}$, which represent quasiparticle excitations and annihilate the new ground state: $\alpha_{\boldsymbol{k}\nu}|\Psi_0\rangle = 0$. Of course, only positive quasiparticle energies, labeled by ν, have physical meaning. However, in order to obtain closure relations for the wavefunction $\left(u_{\boldsymbol{k}a}^\nu, v_{\boldsymbol{k}a}^\nu\right)$ (which is, obviously, even in $\boldsymbol{k}$), we need to include zero-energy eigenvectors as well [83].

This completeness relation has the form (valid for *all* wavevectors):

$$\sum_\nu \left(u_{\boldsymbol{k}a}^\nu u_{\boldsymbol{k}b}^\nu - v_{\boldsymbol{k}a}^\nu v_{\boldsymbol{k}b}^\nu\right) = \delta_{ab}; \quad \sum_\nu \left(u_{\boldsymbol{k}a}^\nu v_{\boldsymbol{k}b}^\nu - v_{\boldsymbol{k}a}^\nu u_{\boldsymbol{k}b}^\nu\right) = 0.$$

The amplitudes $u_a^\nu(\boldsymbol{k})$ and $v_a^\nu(\boldsymbol{k})$ are determined from Bogoliubov equations:

$$U_{ab}^N(\boldsymbol{k})u_{\boldsymbol{k}b}^\nu + U_{ab}^A(\boldsymbol{k})v_{\boldsymbol{k}b}^\nu = \omega_\nu(\boldsymbol{k})u_{\boldsymbol{k}a}^\nu;$$

$$U_{ab}^A(\boldsymbol{k})u_{\boldsymbol{k}b}^\nu + U_{ab}^N(\boldsymbol{k})v_{\boldsymbol{k}b}^\nu = -\omega_\nu(\boldsymbol{k})v_{\boldsymbol{k}a}^\nu, \tag{2.21}$$

where we have introduced symmetric matrices:

$$U_{ab}^N(\boldsymbol{k}) = \frac{1}{2}(\epsilon_a - \mu)\delta_{ab} + \sum_\sigma \left(H_{\mathrm{int}}^\sigma\right)_{a_2 b}^{aa_1} \Theta_{\boldsymbol{k}}^\sigma g_{a_1} g_{a_2} + 2\sum_\sigma \left(H_{\mathrm{int}}^\sigma\right)_{ba_2}^{aa_1} g_{a_1} g_{a_2}; \qquad (2.22)$$

$$U_{ab}^A(\boldsymbol{k}) = \sum_\sigma \left(H_{\mathrm{int}}^\sigma\right)_{ab}^{a_1 a_2} \Theta_{\boldsymbol{k}}^\sigma g_{a_1} g_{a_2}.$$

It follows from Eq. (2.21) that at each $\boldsymbol{k}$ the quasiparticle amplitudes obey the orthogonality conditions:

$$\sum_a \left(u_{\boldsymbol{k}a}^\nu u_{\boldsymbol{k}a}^{\nu'} - v_{\boldsymbol{k}a}^\nu v_{\boldsymbol{k}a}^{\nu'}\right) = \delta_{\nu\nu'}; \quad \sum_a \left(u_{\boldsymbol{k}a}^\nu v_{\boldsymbol{k}a}^{\nu'} - v_{\boldsymbol{k}a}^\nu u_{\boldsymbol{k}a}^{\nu'}\right) = 0.$$

For any value of $\boldsymbol{k}$ Bogoliubov's equations (2.21) always have at least two zero eigenvalues, which correspond to the zero-norm eigenvector $u = -v = g$.

The quasiparticle energy equals $2\omega_\nu(\boldsymbol{k})$ and the GSE, condensate fraction and spin polarization are expressed in terms of $u_{\boldsymbol{k}a}^\nu$ and $v_{\boldsymbol{k}a}^\nu$ as:

$$\frac{E_0}{N} = \frac{1}{8}\left(\mu n_0 + \sum_a \epsilon_a g_a^2\right) + \frac{1}{4}\mu(1 - n_0) - \frac{2}{N}{\sum_{\boldsymbol{k},\nu,a}}' \omega_\nu(\boldsymbol{k})\left(v_{\boldsymbol{k}a}^\nu\right)^2;$$

$$n_0 = 1 - \frac{1}{N_\square}{\sum_{\boldsymbol{k},\nu,a}}' \left(v_{\boldsymbol{k}a}^\nu\right)^2; \qquad (2.23)$$

$$\langle S_{in}^z\rangle = \left(S_n^z\right)_{a'a}\left[g_{a'} g_a + \frac{1}{N_\square}{\sum_{\boldsymbol{k},\nu}}' v_{\boldsymbol{k}a'}^\nu v_{\boldsymbol{k}a}^\nu\right].$$

In this expression $\boldsymbol{k}$-summations are extended over the plaquette Brillouin zone and ν-summations over positive eigenvalues of Eq. (2.21), as indicated by the primes.

2.6.2 Results for the symmetric plaquette covering

The condensate fraction n_0 should be determined self-consistently. The approximation is reasonable if $n_0 \sim 1$. Close to the phase transition points this is not true, since fluctuations are very large. But deep in each phase the approximation works

reasonably well, because n_0 turns out to be ~ 0.9. Results of numerical solution of Eqs. (2.21) and (2.23) for the symmetric covering of the lattice with 2×2 plaquettes are shown in Figs. 2.13 and 2.14. The system size is 100×100 plaquettes and periodic boundary conditions are assumed. Main panels in Figs. 2.13 and 2.14 correspond to the self-consistent solution and their insets give results after the first iteration, which is equivalent to solving the time-dependent Gross-Pitaevskii equation [83]. Due to bad convergence close to the transition points (see, for instance, Fig. 2.13(a)) the values of J_2^{c1} and J_2^{c2} were determined by extrapolation: $J_2^{c1} \approx 0.33 J_1$ and $J_2^{c2} \approx 0.65 J_1$. The large shift of J_2^{c1} compared to the HF value is due to fluctuations in the β-channel, which reduces the nominal value of the magnetization in the Néel phase down to $M(J_2 = 0) \approx 0.37$ (see Fig. 2.13(b)) and causes a great suppression of the condensate, as shown in Fig. 2.14(a).

However, the most interesting quantity to observe is the gap in the excitation spectrum. Due to the homogeneity of the plaquette lattice, it occurs at $\boldsymbol{k} = 0$ and is shown in Fig. 2.5. Technically one may show that its very existence reflects the nature of the ground state in the paramagnetic phase. Indeed, introducing linear combinations of the amplitudes u and v: $\varphi = u + v$ and $\chi = u - v$, Bogoliubov's Eq. (2.21) can be rewritten in the form: $(U^N + U^A)(U^N - U^A)\chi = \omega^2 \chi$. In the non-magnetic phase the condensation occurs in the lowest plaquette state $|1100\rangle$: $g_a = \sqrt{n_0}\delta_{a,1100}$ and the chemical potential coincides with its energy: $\mu = \epsilon_{1100}$. Moreover, the matrix $\sum_\sigma \left(H_{\text{int}}^\sigma\right)_{b,1100}^{a,1100}$ vanishes. Writing down the remaining matrices in (2.22) at $\boldsymbol{k} = 0$, it is easy to see that there exists only one vector χ, which is annihilated by $(U^N - U^A)$. Outside the intermediate region this simple situation is not valid and there exist three eigenvectors χ, which correspond to $\omega^2 = 0$. One of them is the condensate mode and should be discarded. The other two give doubly degenerate Goldstone modes in the Néel and columnar phases. Here the self-consistent field determined by g_a breaks the spin-rotational symmetry of the original Hamiltonian.

However, since the CWF g_a belongs to the $M = 0$ subspace, the generator S_z remains an integral of motion. Thus, there should be two Goldstone modes associated with rotations around the x and y axes [83].

Our approximation correctly describes the excitation spectrum only at small $\boldsymbol{k}$. However, this is more than enough to observe that the collective modes are of the spin-wave type in the Néel and columnar phases, while in the paramagnetic phase the excitation band is parabolic. These conclusions are summarized in Fig. 2.14(b), where we show the lowest branch $\omega_1(\boldsymbol{k})$ along two directions $\boldsymbol{k}\|[10]$ and $\boldsymbol{k}\|[11]$ for three values of J_2/J_1, chosen in different phases.

Chapter 3

Superconductivity in strongly repulsive fermions

In this chapter we address the question of whether it is possible to realize a super-conducting phase in a *strongly repulsive* fermion system. By studying the repulsive two-dimensional Hubbard model, defined on a lattice made of weakly coupled clusters, we analytically show that:

- Lattice frustration enhances local hole pairing;

- Magnetic fluctuations establish a robust superconducting phase;

- There exists an "optimal frustration" for which $d_{x^2-y^2}$-wave superconductivity is stabilized for any value of $U \gg t$;

We also extend the HMF method to hard-core boson systems.

3.1 Introduction

One of long-standing fundamental questions in condensed-matter physics is whether it is possible to realize a superconducting (SC) state in a system consisting only of electrons subject to a strong Coulomb repulsion, and if so what is the minimal set of necessary physical assumptions. As we already mentioned in Sec. 1.1.3 an early attempt to provide an answer was made by Kohn and Luttinger [23], who proposed a weak-coupling Bardeen-Cooper-Schrieffer (BCS) –like mechanism. While their idea was never confirmed experimentally, there exist numerous *strongly* correlated systems whose SC behavior occurs without any obvious pairing "glue" (such as phonons) between the electrons. Examples are high-T_c cuprates and heavy fermion compounds. The current consensus asserts that superconductivity in these materials has an unconventional, i.e. non-BCS, character [85]. Understanding the microscopic origin of this intriguing phenomenon remains a challenge. Here we address the above question by performing a controlled derivation of the SC ground state (GS) for a *strongly-repulsive* Hubbard model with spatially modulated transfer integrals.

One possible way of stabilizing a Cooper pair condensate in a repulsive system is to introduce microscopic inhomogeneities. Indeed, the nanoscale spin and charge modulations observed in scattering [86], ARPES [87] and STM [88] experiments, seem to be ubiquitous in high-T_c materials [89] and often accompany the emergence of the SC state. Theoretically it has been argued that these inhomogeneities are quite relevant for the superconductivity [90, 91] and seem to assist the Cooper pairing. This was demonstrated in [90, 92] by using exact diagonalization of strongly interacting models in finite lattices. In [93] the authors studied the Hubbard model on a checkerboard lattice, composed of weakly coupled 2×2 plaquettes, and showed that the SC phase can be stabilized in a relatively narrow interval of the on-site repulsion U. A similar problem was considered earlier in [94]. Another ingredient, whose importance for superconductivity was largely overlooked, is the range of the transfer integrals beyond

nearest-neighbors (NN). The next-NN (NNN) hopping (t') was shown to enhance $d_{x^2-y^2}$-like pairing correlations in the t-t'-J model on finite clusters [95]. Physically its main qualitative effect is the possible *frustration* of the kinetic-energy term: the smallest closed paths in the lattice are triangles instead of squares.

Below we explicitly demonstrate how *local* kinetic-energy *frustration* can stabilize the SC state in a *strongly repulsive* two-dimensional Hubbard model. The lattice, on which the model is defined, is presented in Fig. 3.1 panels (a) and (b). It consists of weakly-coupled tetrahedra, i.e. plaquettes with frustrated hoppings along the diagonals. We show that a $d_{x^2-y^2}$–wave SC phase exists for *arbitrarily* strong repulsion U. In fact, the problem can be treated analytically in the strong-coupling regime.

Our motivation to study this system is not purely academic. Advances in experimental methods of preparation and manipulation of ultracold fermion atoms in optical lattices provide a controlled way to test these theoretical ideas. For example, in recent experiments [96, 8] the observation of a Mott state with ^{40}K atoms was reported. An experiment aimed to find d-wave superconductivity in a checkerboard Hubbard model was proposed in [97].

3.2 Tetrahedral Hubbard model

3.2.1 General formulation

Let us consider the repulsive Hubbard model:

$$H = -\sum_{\langle ij \rangle, \sigma} t_{ij} \big(c_{i\sigma}^\dagger c_{j\sigma} + \text{h.c.} \big) + U \sum_i n_{i\uparrow}^e n_{i\downarrow}^e, \qquad (3.1)$$

defined on the lattice, Fig. 3.1(a), in terms of fermionic (creation) operators $c_{i\sigma}^\dagger$. Here $\langle ij \rangle$ denotes links connecting sites i and j, $\sigma = \{\uparrow, \downarrow\}$ is the electron spin, and $n_{i\sigma}^e = c_{i\sigma}^\dagger c_{i\sigma}$. The amplitudes t_{ij} take four possible values: (i) t for links $\langle 12 \rangle$, $\langle 13 \rangle$,
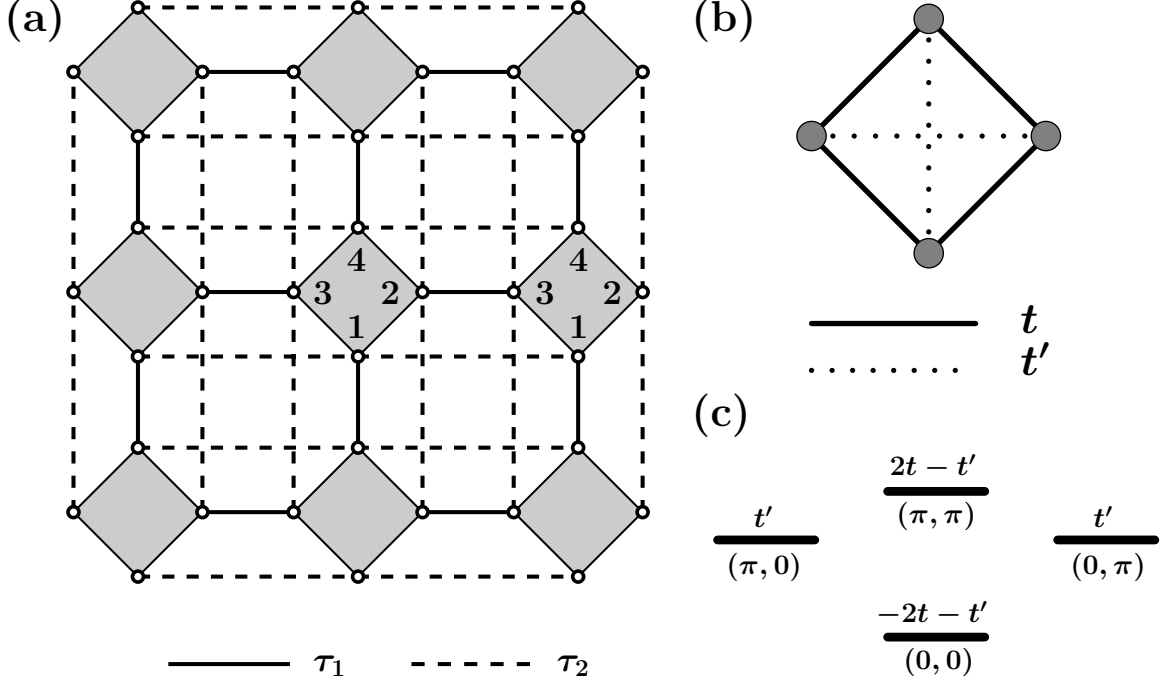
Figure 3.1: (a) Tetrahedral lattice topology. The interplaquette hopping amplitudes are: NN τ_1 (solid lines) and NNN τ_2 (dashed lines). We only consider the case $\tau_2 \leqslant \tau_1$. (b) A frustrated plaquette (tetrahedron) with NN (solid line) and NNN (dotted line) hoppings. (c) Single-electron states on the plaquette in panel (b). Numbers in parentheses denote $\boldsymbol{k}$-components.

$\langle 24 \rangle$ and $\langle 34 \rangle$; (ii) t' for the diagonals $\langle 14 \rangle$ and $\langle 23 \rangle$; (iii) τ_1 for NN links, connecting two plaquettes; (iv) τ_2 for NNN interplaquette links.

We will consider the case $\tau_{1,2} \ll t, t', U$, which allows for a controlled perturbative expansion of the Hamiltonian (3.1). To demonstrate the existence of a robust SC phase, we derive a low-energy effective model accurate to second order in $\tau_{1,2}$. In general this is doable only numerically. However, in the limit $t, t' \ll U$ we can keep only lowest-order terms in t_{ij}/U, and thus provide a closed form for the effective Hamiltonian (EH). The stability of the Cooper pair condensate can be tuned by changing the ratio t'/t. There is an "optimal" value of this ratio, which ensures a finite energy gap (hole binding energy) between the plaquette states with one and two holes for all finite U.
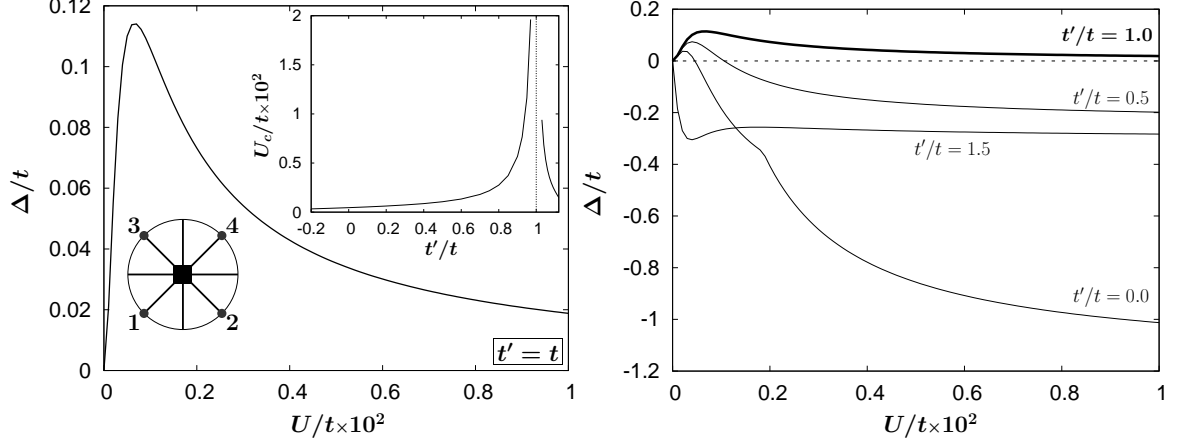
Figure 3.2: Left panel: Hole binding energy $\Delta(U)$ in the maximally frustrated case $t' = t$. The asymptotic behavior is: $\Delta(U \gg t) \approx 2t^2/U$ and $\Delta(U \ll t) \approx U^2/32t$. Upper inset: Critical value $U_c(t')$ [$\Delta(U_c) = 0$]. Lower inset: Group C_{4v}. Numbers indicate plaquette vertices. The black square denotes four-fold axis C_4, horizontal and vertical lines – primary symmetry planes σ_v, diagonals – secondary planes σ_v'. Right panel: Hole binding energy $\Delta(U)$ for several values of NNN hopping t'.

3.2.2 Single-plaquette states

The Hubbard Hamiltonian on a single plaquette can be diagonalized exactly [94] by using representations of the crystallographic group C_{4v} [98] (see the lower inset in the left panel in Fig. 3.2). Details of this simple, but lengthy calculation are presented in Appendix A at the end of this chapter; here we only use the relevant results.

Our main quantity of interest is the hole binding energy $\Delta = 2\epsilon_0(3) - \epsilon_0(2) - \epsilon_0(4)$, where $\epsilon_0(N_e)$ is the GS for a given number of electrons N_e. Positive values of Δ correspond to binding of two holes. In general Δ is positive only in a finite range of U. At some critical value $U_c(t')$ (Fig. 3.2, right panel and upper inset in the left panel), it changes sign and remains negative as $U \to \infty$. There is a special ratio, $t'/t = 1$, at which U_c diverges and Δ stays *positive* for any value of U (left panel of Fig. 3.2). This results from the maximal frustration of the single-hole kinetic energy. The GS energy for 4 electrons (zero holes), $\epsilon_0(4) \to 0$ for $U \to \infty$ because the particles cannot move. On the other hand in this limit $\epsilon_0(2) = 2\epsilon_0(3)$, which means that there is no kinetic-

$$\epsilon_0(3) - \epsilon_0(4) = J \qquad\qquad \epsilon_0(2) - \epsilon_0(4) = J$$
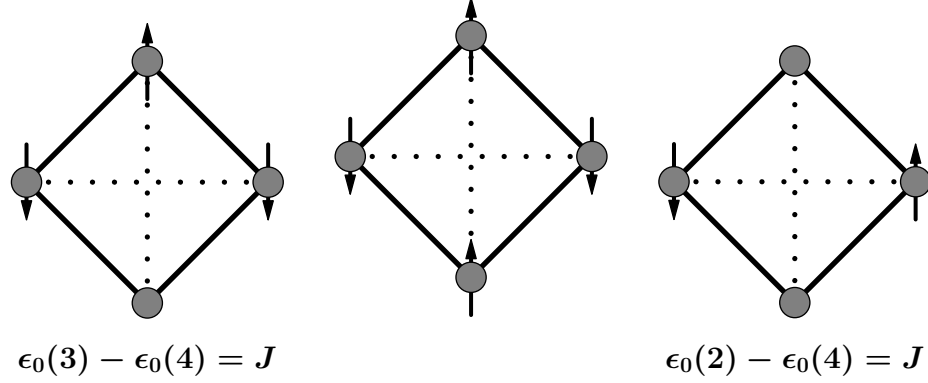
Figure 3.3: Magnetic mechanism of hole binding in an isolated plaquette. Shown are plaquettes with three (left), four (center) and two (right) electrons. The arrows denote electron spins. When $t' = t$ and $t/U \ll 1$, the GS at half filling is degenerate (see Chap. 1.1.2). NNN hopping leads to the frustrating exchange interaction $J' = 4t^2/U$ for small t/U. The magnetic energy costs of removing one and two electrons from the half-filled plaquette are the same, leading to $\Delta_M = J$.

energy gain for creating two holes on different plaquettes; i.e. the single-hole kinetic energy is optimally frustrated. The exchange interaction $J = 4t^2/U$ that appears for finite $t/U \ll 1$ leads to pairing ($\Delta > 0$) because the magnetic configuration of two plaquettes with one hole in each of them is more frustrated than the configuration with two holes in the same plaquette (see Fig. 3.3). This leads to a positive value of $\Delta_M = J$. Corrections coming from the kinetic energy of holes, reduce this value by $J/2$, resulting in the hole binding energy of $\Delta = J/2$.

From now on we will only consider the maximally frustrated point $t'/t = 1$. Then the symmetry group $\mathcal{G}$ of the single-plaquette Hamiltonian is larger than C_{4v} (symmetry group for arbitrary t'/t) and contains all the independent permutations of any pair of vertices of the plaquette. This symmetry translates into a GS degeneracy at half-filling. There are two $SU(2)$-singlet states: one transforming as the identity representation of C_{4v}, A_1 (s-wave), and the other – as B_1 ($d_{x^2-y^2}$-wave) [4]. These states are connected by symmetry operations from the factor group $\mathcal{G}/C_{4v}$. The two-electron GS is also a singlet and belongs to the identity representation of $\mathcal{G}$. The $N_e = 3$ GS has $S = 1/2$ and is six-fold degenerate.

General expressions for these eigenstates are quite cumbersome. However, to the lowest order in t/U we can consider only states without doubly occupied sites. Hence we have the GS for $N_e = 2$: $|\Omega_2\rangle = (1/2\sqrt{3}) \sum_{\langle ij \rangle} s_{ij}^\dagger |0\rangle$ with the summation extended over all links of a plaquette; and for $N_e = 4$: $|\Omega_4^{s,d}\rangle = \mathcal{N}_{s,d}(s_{13}^\dagger s_{24}^\dagger \pm s_{12}^\dagger s_{34}^\dagger)|0\rangle$. In these expressions $s_{ij}^\dagger$ is a singlet creation operator, $s_{ij}^\dagger = c_{i\uparrow}^\dagger c_{j\downarrow}^\dagger - c_{i\downarrow}^\dagger c_{j\uparrow}^\dagger$, $|0\rangle$ is the empty state and $\mathcal{N}_s = -1/2$, $\mathcal{N}_d = 1/2\sqrt{3}$. Finally, we introduce operators P_{ij}, which permute sites i and j. In the basis $\{|\Omega_4^s\rangle, |\Omega_4^d\rangle\}$, P_{12} and P_{13} have the form: $P_{12,13} = -\sigma^z/2 \pm \sqrt{3}\sigma^x/2$ with σ^α ($\alpha = x, z$) Pauli matrices. We will use this expression to determine symmetries of the effective model.

3.2.3 Effective low-energy theory

The low-energy spectrum of decoupled plaquettes has a gap Δ to single-hole ($N_e = 3$ on each plaquette) states. Here we consider the effect of finite hopping amplitudes $\tau_{1,2}$ by assuming that $0 \leqslant \tau_{1,2} \ll \Delta \sim t^2/U \ll t \ll U$. The second inequality allows us to treat interplaquette hoppings perturbatively. The fourth one allows us to exclude states with doubly occupied sites, i.e. use as a basis the states $|\Omega_2\rangle$ and $|\Omega_4^{s,d}\rangle$. Finally, the third inequality constrains the choice of the virtual states: only states that belong to the $N_e = 3$ GS sextet contribute to lowest order. We will also assume that $\tau_2 \leqslant \tau_1$.

The second-order EH can be symbolically written as:

$$H_{\text{eff}} = \mathcal{P}^{(0)} H_\tau (1 - \mathcal{P}^{(0)}) \frac{1}{E_0 - H^{(0)}} (1 - \mathcal{P}^{(0)}) H_\tau \mathcal{P}^{(0)},$$

where $H^{(0)}$ describes a set of noninteracting plaquettes in (3.1), E_0 is its GS energy, H_τ denotes plaquette interactions, and $\mathcal{P}^{(0)}$ is a projector onto the subspace with $N_e = 2$ or 4 on each plaquette. Next we associate the product of the two-electron plaquette GS with the vacuum: $|\text{vac}\rangle = \prod_x |\Omega_2\rangle_x$ and each member of the four-electron GS

doublet on plaquette x – with a hard-core boson: $|\Omega_4^\alpha\rangle_x = b_{x\alpha}^\dagger|\Omega_2\rangle_x$, where $\alpha = s$ or d represents the pseudospin index. The algebra generated by $b_{x\sigma}$ was discussed in Ref. [99]. Thus, the effective low-energy theory given by H_{eff} describes a system of two-flavor hard-core bosons, propagating in the coarse-grained plaquette lattice of Fig. 3.1(a). In terms of these boson operators we have:

$$
H_{\text{eff}} = \sum_{\langle xy\rangle,\alpha\beta} t_{\alpha\beta}^{\text{eff}}\left(b_{x\alpha}^\dagger b_{y\beta} + b_{y\beta}^\dagger b_{x\alpha}\right) - \mu\sum_{x,\alpha} n_{x\alpha}+ \tag{3.2}
$$
$$
+ \sum_{\langle xy\rangle,\alpha\beta} V_{\alpha\beta}^{\text{eff}}\left[(1-n_x)b_{y\alpha}^\dagger b_{y\beta} + (1-n_y)b_{x\alpha}^\dagger b_{x\beta}\right],
$$

where $\langle xy\rangle$ denotes NN plaquettes, $t_{\alpha\beta}^{\text{eff}}$ are corresponding hopping amplitudes, $V_{\alpha\beta}^{\text{eff}}$ – density-density and local spin-flip interactions, $n_{x\alpha} = b_{x\alpha}^\dagger b_{x\alpha}$ and $n_x = n_{xs} + n_{xd}$, and μ is the chemical potential. The virtual processes leading to t^{eff} and V^{eff} are schematically shown in panel (a) in Fig. 3.4. Direct interactions between pseudospins, like Heisenberg terms, are not present to lowest order in Δ/t and t/U. For details regarding the derivation of Eq. (3.2) and following expressions, we direct the reader to Appendix B at the end of this chapter.

Some general properties of t^{eff} and V^{eff} can be established by symmetry arguments. First, the Hamiltonian (3.1) is invariant under reflections in the planes which include τ_1 links, e.g. the plane connecting sites 2 and 3 in Fig. 3.1(a). The states $|\Omega_2\rangle$ and $|\Omega_4^s\rangle$ are symmetric under this operation, while the d-wave state $|\Omega_4^d\rangle$ is antisymmetric. Consequently the off-diagonal matrix elements of t_{sd}^{eff} and V_{sd}^{eff} vanish: $t_{\alpha\beta}^{\text{eff}} = t_{\alpha\alpha}^{\text{eff}}\delta_{\alpha\beta}$, $V_{\alpha\beta}^{\text{eff}} = V_{\alpha\alpha}^{\text{eff}}\delta_{\alpha\beta}$. This result is independent of the assumptions made regarding the relative magnitude of $\tau_{1,2}$, U and t.

Another observation concerns the diagonal elements of t^{eff} and V^{eff} in the special cases $\tau_2 = \tau_1$ and $\tau_2 = 0$. In the first case we consider the two plaquettes with numbered sites, shown in Fig. 3.1(a), and perform simultaneous permutations of vertices $1 \leftrightarrow 2$ on the left plaquette and $1 \leftrightarrow 3$ on the right one. Each operation is a symme-

try of the single-plaquette Hamiltonian. Their combination amounts to interchanging the τ_1 and τ_2 links, which is now a symmetry of the connecting Hamiltonian. Using the relation $P_{12,13}|\Omega_2\rangle = |\Omega_2\rangle$, it is easy to show that for $\tau_1 = \tau_2$: $t_{ss}^{\text{eff}} = -t_{dd}^{\text{eff}}$ and $V_{ss}^{\text{eff}} = V_{dd}^{\text{eff}}$. In the case $\tau_2 = 0$, when the plaquettes are connected by only one τ_1 link, the second-order virtual hopping of an electron can only proceed through an intermediate state, whose energy is of order U. Therefore, in the approximation formulated above t^{eff} must vanish. On the contrary, V^{eff} is not associated with the net electron transfer and remains finite.

A direct calculation yields the precise form of the coefficients t^{eff} and V^{eff}:

$$t_{\alpha\beta}^{\text{eff}} = -\left(\tau_1^2/6\Delta\right)\text{diag}\left\{r_\tau(2r_\tau + 1),\ -3r_\tau\right\}; \tag{3.3}$$

$$V_{\alpha\beta}^{\text{eff}} = -\left(\tau_1^2/48\Delta\right)\text{diag}\left\{9 + 8r_\tau + 16r_\tau^2,\ 9 + 24r_\tau^2\right\}$$

with $r_\tau = \tau_2/\tau_1$. Clearly, in the two special cases discussed above – $r_\tau = 1$ and 0 – the EH (3.2) becomes pseudospin symmetric. The second case is irrelevant for the purposes of studying the SC state, while the first one, $r_\tau = 1$, is quite instructive. In this case we can use the Perron-Frobenius theorem to prove that there exists a pseudospin-polarized GS [100]. The Hamiltonian can then be written only in terms of spinless bosons (say b_{xd}) and maps onto the spin-1/2 XXZ model in a magnetic field μ via the Matsubara-Matsuda transformation [101]. The phase diagram of this model contains Néel, canted XY-antiferromagnetic, and fully polarized states that are immediately identified with the density-wave (DW), Bose-Einstein condensate (BEC) of Cooper pairs, and Mott phases, respectively. The DW and BEC states are separated by a 1st order quantum phase transition.
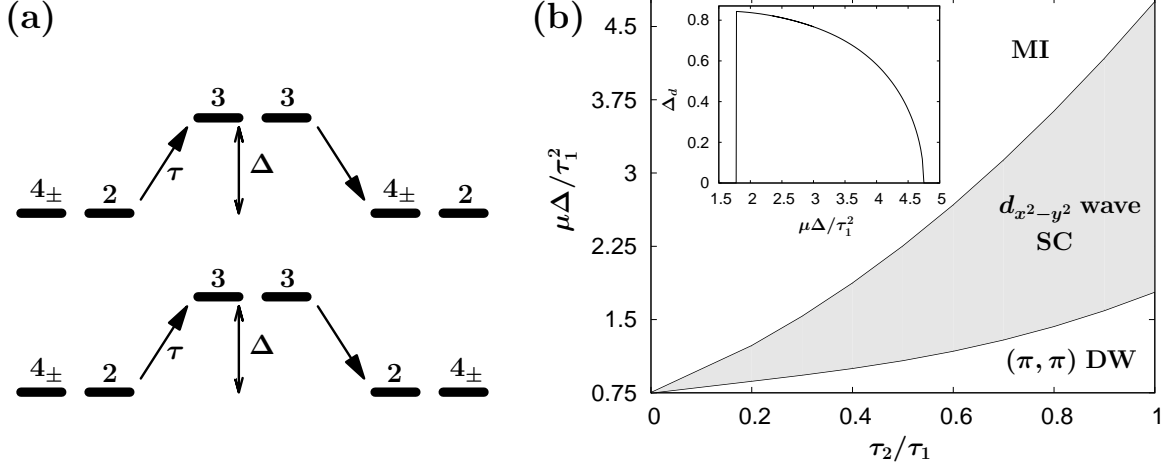
Figure 3.4: (a) Lowest order virtual processes which contribute to the coefficients $V_{\alpha\beta}^{\text{eff}}$ (top) and $t_{\alpha\beta}^{\text{eff}}$ (bottom) in Eq. (3.2). (b) Low-energy phase diagram of the Hubbard model Eq. (3.1). Phases are: s-wave density wave (DW) with wavevector (π, π); d-wave SC, which corresponds to a BEC of b_d; Mott insulating (MI) phase with $\langle n_x \rangle = 1$. The DW – SC phase transition is 1st order; the SC – MI transition is 2nd order. The inset shows $\Delta_d \sim \langle b_{xd} \rangle$ for $r_\tau = 1$.

3.3 Results

3.3.1 Phase diagram of the low-energy model

We do not expect the physics to change qualitatively for $0 < r_\tau < 1$. It is known that the usual mean-field approximation yields satisfactory results for $r_\tau = 1$ when compared to Monte-Carlo simulations [102]. Thus, we anticipate that the rest of the phase diagram along the r_τ axis can be described within a simple variational approach. We employ the HMF method explained in Chap. 2 which includes short-range quantum fluctuations and, as a limit, contains the semiclassical spin-wave ansatz (see Appendix C for details). The resulting phase diagram obtained using 2×2 site clusters (in the plaquette lattice) is presented in Fig. 3.4(b). For any finite $0 < r_\tau < 1$ the system exhibits the same three phases, as in the case $r_\tau = 1$. The SC and DW phases are again separated by a 1st order transition. The transition between SC and Mott phases is 2nd order. In the Mott state there is exactly one boson per site; i.e. the

electron filling is 1/2. In this phase the pseudospin polarization is undefined, as the Hamiltonian (3.2) becomes spin-independent. Interestingly the DW phase is of an s-wave nature, because the expectation value of the kinetic energy vanishes, while density-density interactions favor the s-wave pseudospin polarization.

The SC state has a $d_{x^2-y^2}$-wave symmetry. The structure of the "Cooper pair" can be determined by observing that $b_d = \mathcal{D}/3 - (1/4)(s_{14} + s_{23})\big(|\updownarrow\updownarrow\rangle\langle\updownarrow\updownarrow| - |\leftrightarrow\rangle\langle\leftrightarrow|\big)$, where $|\updownarrow\updownarrow\rangle = s^\dagger_{13}s^\dagger_{24}|0\rangle$, $|\leftrightarrow\rangle = s^\dagger_{12}s^\dagger_{34}|0\rangle$ and $\mathcal{D} = s_{13} + s_{24} - s_{12} - s_{34}$ (see the lower inset of Fig. 3.2). Hence, despite the apparent complexity of the SC phase it can still be characterized by a familiar d-wave order parameter $\Delta_d = \langle\mathcal{D}\rangle$, shown in the inset of Fig. 3.4(b) for $r_\tau = 1$. As r_τ decreases, the height of the SC dome gradually diminishes and disappears at $r_\tau = 0$. Thus, for any $0 < r_\tau < 1$ there is an interval of μ where the SC phase is stabilized. This conclusion becomes rigorous in the dilute limit of particles or holes by virtue of the inequality $|t^{\text{eff}}_{dd}| > |t^{\text{eff}}_{ss}|$, valid for $r_\tau < 1$ [see Eq. (3.3)].

3.3.2 Possible application to optical lattices

Before closing this chapter we would like to address the possibility to test our theory in experiments, involving cold atoms in optical lattices. In particular, we are going to discuss potential realizations of the "maximally" frustrated 2×2 plaquette optical lattice. A related proposal to build a square optical lattice with NNN hoppings was discussed in [103]. It was concluded that the maximal value of the NNN hopping (relative to the NN amplitude) that can be achieved is close to one-half: $t'/t = 0.5$. Thus, the experimental realization of the interesting case $t'/t = 1$ seems to face serious challenges. In the present section we present a theoretical proposal aimed to circumvent this difficulty. Our argument builds upon ideas developed in [103].

We start by constructing a 2D optical lattice consisting of isolated 2×2 plaquettes. This can be accomplished by superimposing two laser beams along the orthogonal x
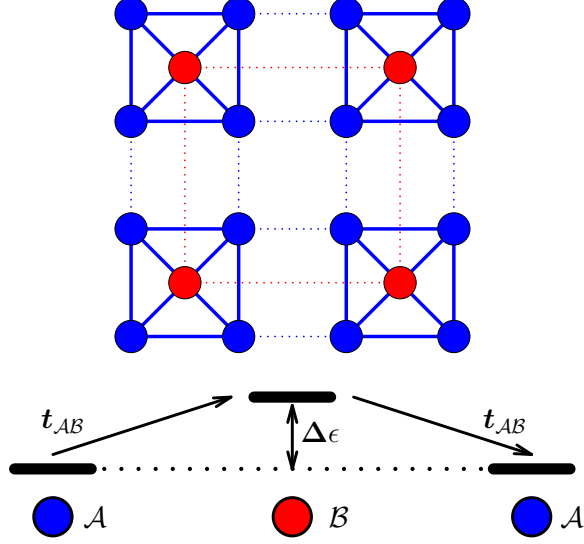
Figure 3.5: Upper panel: Optical lattice proposed in the text. Blue (red) circles denote sites in the sublattice $\mathcal{A}$ ($\mathcal{B}$). Thick blue lines represent *equal* $\mathcal{A}$-$\mathcal{A}$ intraplaquette hoppings through the central $\mathcal{B}$ site; the direct $\mathcal{A}$-$\mathcal{A}$ hopping is suppressed. Lower panel: Indirect hopping process between the $\mathcal{A}$ sites.

and y directions

$$V_0(x,y) = v(x) + v(y). \tag{3.4}$$

Along each direction the potential $v(\xi)$ is a combination

$$v(\xi) = f_2(\xi) - \eta f_1(\xi),$$

where $f_k(\xi) = \cos\frac{2\pi k\xi}{\lambda}$, and λ is the optical wavelength. By varying the parameter η, the interplaquette hopping can be made much smaller than the intraplaquette one. We will denote the lattice thus created as $\mathcal{A}$.

Next we build another 2D lattice $\mathcal{B}$ on top of the first one with twice the period. The corresponding optical potential, $V_1(x,y)$, is chosen so that its minima concide with the centers of plaquettes. The resulting two-lattice construction is shown schematically in Fig. 3.5. The separation $\Delta\epsilon$ between GS in $\mathcal{A}$- and $\mathcal{B}$-type quantum wells can be controlled by tuning parameters in V_0 and V_1. Due to the large $\mathcal{B}$ lattice

constant we can neglect the direct $\mathcal{B}$-$\mathcal{B}$ hopping and consider only the interlattice processes, $t_{\mathcal{AB}}$.

The transfer of a fermion between two $\mathcal{A}$ type sites can now occur either directly, or via a 2nd order process through the central $\mathcal{B}$ site. The amplitude of the direct hopping can be estimated as

$$t_{\mathcal{AA}} \sim t_{\mathcal{AA}}^0 \, e^{-(a/a_0)^{p_0}}, \tag{3.5}$$

where the spatial separation between minima a, the prefactor $t_{\mathcal{AA}}^0$, the characteristic length a_0, and power p_0 depend on details of the potential; of course, they are not mutually independent. The interlattice hopping can similarly be written as

$$t_{\mathcal{AB}} \sim t_{\mathcal{AB}}^0 \, e^{-(a/\sqrt{2}a_1)^{p_1}},$$

with parameters having the same interpretation as in $t_{\mathcal{AA}}$. Therefore, the 2nd order (indirect) hopping process has an amplitude ($\Delta\epsilon \gg t_{\mathcal{AB}}$)

$$\tilde{t}_{\mathcal{AA}} = -\frac{t_{\mathcal{AB}}^2}{\Delta\epsilon} \sim -\frac{\left(t_{\mathcal{AB}}^0\right)^2}{\Delta\epsilon} e^{-2(a/\sqrt{2}a_1)^{p_1}}. \tag{3.6}$$

Our key assumption is that the direct hopping (3.5) can be made smaller than the 2nd order amplitude (3.6), i.e. $t_{\mathcal{AA}} < \tilde{t}_{\mathcal{AA}}$. This can be achieved by increasing either a_1/a_0 or a/a_0. We note that a_0 and a_1 are determined by the curvature of the minima of $V_0(x,y)$ and $V_1(x,y)$. In particular, since lattice $\mathcal{A}$ has a higher density of minima (four per unit cell) than lattice $\mathcal{B}$ (one minimum per unit cell), these minima are steeper than the ones of lattice $\mathcal{B}$. Therefore, the ratio a_1/a_0 must be larger than one. Once the condition $t_{\mathcal{AA}} < \tilde{t}_{\mathcal{AA}}$ is satisfied the fermion can tunnel between *any* two $\mathcal{A}$ sites within a plaquette only through the central $\mathcal{B}$ site. Clearly the amplitudes for all these indirect processes coincide, i.e. $t' \sim t$.
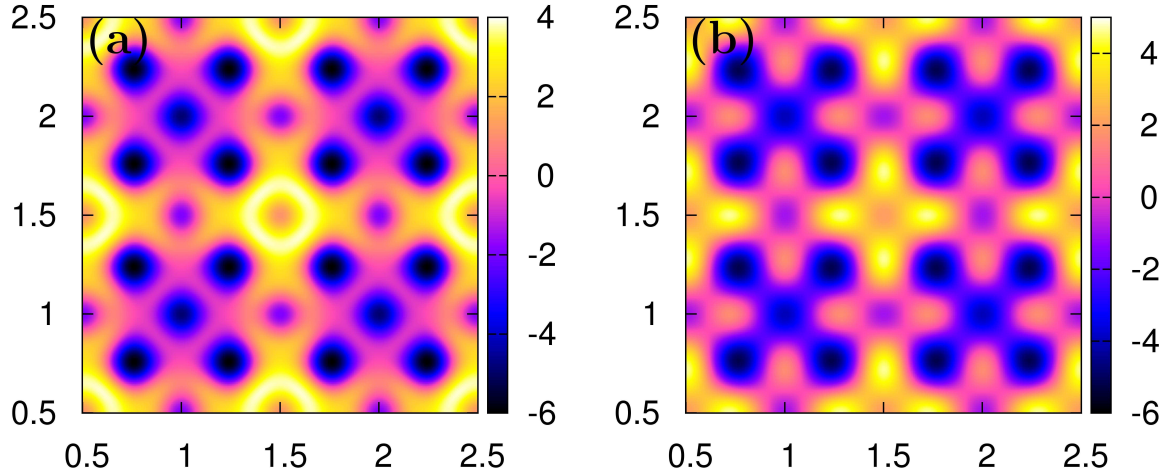
Figure 3.6: Optical potentials Eq. (3.7): (a) $V^{(a)}$ with $(\eta, \nu) = (1.5, 1.3)$. (b) $V^{(b)}$ with $(\eta, \nu) = (1.5, 3.0)$.

Let us consider a couple of example optical potentials, which may be used to realize this regime:

$$V^{(a)} = \sum_{\xi=x,y} v(\xi) - \nu\big[\big(1 + f_2(x-y)\big)\big(1 + f_2(x+y)\big) - 1\big];$$

$$V^{(b)} = \sum_{\xi=x,y} v(\xi) - \nu f_2(x) f_2(y), \tag{3.7}$$

where all distances are measured in the units of the optical wavelength, i.e. $\lambda = 1$. Color maps of these functions are shown in Fig. 3.6.

3.4 Discussion

Our phase diagram (Fig. 3.4(b)) was obtained in the strong-coupling limit $t/U \ll 1$, where one can derive the effective model of Eqs. (3.2), (3.3). The EH becomes increasingly complicated for intermediate couplings $U \sim t$, because of the large number of virtual transitions. In this regime the existence of d-wave superconductivity in the nonfrustrated Hubbard model was argued in [93] based on a first-order EH, treated within a mean-field approximation, and in the weak-coupling regime $U \ll t$ in [26].

Therefore, we expect the SC phase to persist for $U \sim t$ in our frustrated case as well. However, regardless of the magnitude of U, the SC state is quite sensitive to the presence of longer-range repulsions. For instance, an interaction of the form $\sum V_{ij} n_i^e n_j^e$ with $V_{ij} = V$ for all links within the plaquette, will suppress the local hole binding if $V \geqslant V_c = 0.114t$. For $V < V_c$ the SC phase is stable only in a finite interval of U around $U \sim 7t$.

Our theory highlights the importance of kinetic energy frustration for stabilizing the SC state. Locally, pairing competes against the kinetic energy and can be increased by frustrating the latter. This principle guides the choice of the *elementary unit*, e.g., tetrahedron. The *connectivity* of the lattice, built from these blocks is another essential ingredient. Here we used the lattice of Fig. 3.1(a) to demonstrate the existence of the SC state in a physically transparent way. However, we also considered the usual checkerboard lattice [93]. In this case the relation between coefficients in the EH is such that the phase-separated state can suppress superconductivity in a certain region of the phase diagram. The importance of the lattice topology is further illustrated by the case $\tau_2 = 0$. Without the interplaquette hopping (3.3), the global phase coherence can be established only in higher orders in $1/U$, leading to a quite fragile SC state.

We believe that the lattice of Figs. 3.1(a) and 3.5 can be realized using ideas of Refs. [97, 103]. Our effective strong-coupling model can be easily extended to the currently experimentally realizable regime $t'/t \lesssim 0.5$ under the condition $t \ll U < U_c$, which can still be fulfilled for $t'/t = 0.5$ because $U_c \approx 11t$ (see inset of Fig. 3.2). The resulting phase diagram is qualitatively the same as the one shown in Fig. 3.4(b). Thus, our results can be tested in future cold atom experiments.

Table 3.1: Character table of C_{4v}, see also Fig. 3.2 and [4]

C_{4v}	1	C_2	$2C_4$	$2\sigma_v$	$2\sigma'_v$
A_1	1	1	1	1	1
A_2	1	1	-1	1	-1
A_3	1	1	-1	-1	1
A_4	1	1	1	-1	-1
E	2	-2	0	0	0

3.5   Appendix A: Single-plaquette states

The Hubbard model on a 2×2 plaquette with NN (t) and NNN (t') hoppings is given by (see also Fig. 3.1):

$$H_{2\times 2} = T(t, t') + V = -t \sum_{\sigma} \left[\left(c_{1\sigma}^\dagger + c_{4\sigma}^\dagger \right) \left(c_{2\sigma} + c_{3\sigma} \right) + \text{h.c.} \right] -$$

$$- t' \sum_{\sigma} \left(c_{1\sigma}^\dagger c_{4\sigma} + c_{2\sigma}^\dagger c_{3\sigma} + \text{h.c.} \right) + U \sum_{i=1}^{4} n_{i\uparrow} n_{i\downarrow}. \tag{3.8}$$

Note that we do not impose periodic boundary conditions. In the general case $t \neq t'$, this Hamiltonian is invariant under transformations from the group C_{4v}, whose character table [4] is shown in Tab. 3.1. Therefore, the Hilbert space breaks into sectors, corresponding to irreducible representations of this group. At the maximally frustrated point $t = t'$ there is an additional symmetry associated with permutations of every pair of sites. It will allow us to reduce the dimension of each of the above sectors even further and give analytical expressions for the GS energies and wavefunctions for $N_e = 2$, 3 and 4 electrons.

Throughout this section the following notations will be widely used:

$$\{ij\} = c_{i\uparrow}^\dagger c_{j\downarrow}^\dagger - c_{i\downarrow}^\dagger c_{j\uparrow}^\dagger; \quad [ij] = c_{i\uparrow}^\dagger c_{j\downarrow}^\dagger + c_{i\downarrow}^\dagger c_{j\uparrow}^\dagger; \quad (ij) = c_{i\uparrow}^\dagger c_{j\downarrow}^\dagger.$$

3.5.1 General case $t \neq t'$

(i) Two holes: $N_e = 2$

The GS is a spin singlet. There are ten singlet states: four have only doubly occupied sites, and remaining six states contain exactly one electron per site. The corresponding representations, D_4 and D_6, are reducible in C_{4v} and can be decomposed as:

	1	C_2	$2C_4$	$2\sigma_v$	$2\sigma'_v$	
D_4	4	0	0	0	2	$A_1 + A_3 + E$
D_6	6	2	0	2	2	$2A_1 + A_2 + A_3 + E$

The basis functions of 1D representations are given by:

$$|\psi_1\rangle \equiv |\psi_{A_1}^1\rangle = \frac{1}{2}\sum_{i=1}^{4}(ii)|0\rangle;$$

$$|\psi_2\rangle \equiv |\psi_{A_1}^2\rangle = \frac{1}{2}(\{14\} + \{23\})|0\rangle;$$

$$|\psi_3\rangle \equiv |\psi_{A_1}^3\rangle = \frac{1}{\sqrt{8}}(\{12\} + \{13\} + \{24\} + \{34\})|0\rangle;$$

$$|\psi_{A_2}\rangle = \frac{1}{\sqrt{8}}(\{12\} - \{13\} - \{24\} + \{34\})|0\rangle;$$

$$|\psi_{A_3}^1\rangle = \frac{1}{2}\sum_{i=1}^{4}(-1)^i(ii)|0\rangle;$$

$$|\psi_{A_3}^2\rangle = \frac{1}{2}(\{14\} - \{23\})|0\rangle.$$

Clearly the interacting term V in the Hubbard Hamiltonian is diagonal in this basis. Matrix elements of the kinetic energy $T(t, t')$ between the states $|\psi_{1,2,3}\rangle$ are given by:

$$T = \begin{pmatrix} 0 & -2t' & -\sqrt{8}t \\ -2t' & 0 & -\sqrt{8}t \\ -\sqrt{8}t & -\sqrt{8}t & -2t' \end{pmatrix}$$

(ii) Half-filling: $N_e = 4$

The GS is again a singlet. In total there are 20 singlet states. Similarly to the previous subsection they can be decomposed into three groups depending on the site occupancy: only double (6 states), single and double (12 states) and only single (2 states). The corresponding decompositions are:

	1	C_2	$2C_4$	$2\sigma_v$	$2\sigma_v'$	
D_2	2	2	0	2	0	$A_1 + A_2$
D_6	6	2	0	2	2	$2A_1 + A_2 + A_3 + E$
D_{12}	12	0	0	0	2	$2A_1 + A_2 + 2A_3 + A_4 + 3E$

Again, we will consider only 1D representations for D_2 and D_6, and only A_1 and A_2 representations for D_{12}. The basis functions are:

$$|\psi_1\rangle \equiv |\psi_{A_1}^1\rangle = \frac{1}{\sqrt{2}}\left[(11)(44) + (22)(33)\right]|0\rangle;$$

$$|\psi_2\rangle \equiv |\psi_{A_1}^2\rangle = \frac{1}{2}\left[(11) + (44)\right]\left[(22) + (33)\right]|0\rangle;$$

$$|\psi_3\rangle \equiv |\psi_{A_1}^3\rangle = \frac{1}{2}\{14\}\{23\}|0\rangle;$$

$$|\psi_4\rangle \equiv |\psi_{A_1}^4\rangle = \frac{1}{\sqrt{8}}\left[((11) + (44))\{23\} + ((22) + (33))\{14\}\right]|0\rangle;$$

$$|\psi_5\rangle \equiv |\psi_{A_1}^5\rangle = \frac{1}{4}\big[((11) + (33))\{24\} + ((11) + (22))\{34\}+$$

$$+ ((22) + (44))\{13\} + ((33) + (44))\{12\}\big]|0\rangle;$$

$$|\psi_{A_2}^1\rangle = \frac{1}{2}\left[(11) - (44)\right]\left[(22) - (33)\right]|0\rangle;$$

$$|\psi_{A_2}^2\rangle = \frac{1}{2\sqrt{3}}\left[2((13)(42) + (31)(24)) - [14][23]\right]|0\rangle;$$

$$|\psi_{A_2}^3\rangle = \frac{1}{4}\big[((11) + (33))\{24\} + ((22) + (44))\{13\}-$$

$$- ((11) + (22))\{34\} - ((33) + (44))\{12\}\big]|0\rangle;$$

$$|\psi_{A_3}\rangle = \frac{1}{\sqrt{2}}\left[(11)(44) - (22)(33)\right]|0\rangle.$$

The matrix elements of $T(t, t')$ in the basis $|\psi_{1...5}\rangle$ have the form:

$$T = \begin{pmatrix} 0 & 0 & 0 & 0 & -\sqrt{8}t \\ 0 & 0 & 0 & -\sqrt{8}t' & -2t \\ 0 & 0 & 0 & -\sqrt{8}t' & 2t \\ 0 & -\sqrt{8}t' & -\sqrt{8}t' & 0 & 0 \\ -\sqrt{8}t & -2t & 2t & 0 & 0 \end{pmatrix}$$

(iii) One hole: $N_e = 3$

In this sector the GS has both finite spin and momentum. In the absence of the second-neighbor hopping t' the spin of the GS is $1/2$ for small U/t [104] and $3/2$ for U/t above some critical value, in accordance with Nagaoka's theorem [105]. When $t' \neq 0$, it turns out than the GS always has spin $1/2$. In general the states with momentum $q_1 = (0, \pi)$ or $q_2 = (\pi, 0)$ have lower energy that the state with $q_3 = (\pi, \pi)$, and form a 2D vector representation of C_{4v}. However, in the maximally frustrated case $t = t'$ all three of these states become degenerate. Therefore, below we only compute matrix elements of $T(t, t')$ between states with spin $1/2$ and momentum q_3, which belong to the antisymmetric representation A_3 (see Tab. 3.1).

In the subspace without doubly occupied sites there are twelve $S_z = 1/2$ states. They form a representation which decomposes as $2A_1 + A_2 + 2A_3 + A_4 + 3E$. However, only eight of them correspond to $S = 1/2$, and the representation is reduced as:

	1	C_2	$2C_4$	$2\sigma_v$	$2\sigma_v'$	
D_8	8	0	0	0	0	$A_1 + A_2 + A_3 + A_4 + 2E$

The subspace with doubly occupied sites is twelve-dimensional and all states have spin $1/2$. The corresponding representation is isomorphic to D_{12} of the half-filled case considered above.

The basis functions for 1D representations with $S_z = 1/2$ are:

$$|\psi_1\rangle \equiv |\psi_{A_3}^1\rangle = \frac{1}{\sqrt{8}}\left[\{14\}(c_{2\uparrow}^\dagger + c_{3\uparrow}^\dagger) - \{23\}(c_{1\uparrow}^\dagger + c_{4\uparrow}^\dagger)\right]|0\rangle;$$

$$|\psi_2\rangle \equiv |\psi_{A_3}^2\rangle = \frac{1}{2}\left[(c_{4\uparrow}^\dagger(11) + (44)c_{1\uparrow}^\dagger) - (c_{3\uparrow}^\dagger(22) + (33)c_{2\uparrow}^\dagger)\right]|0\rangle;$$

$$|\psi_3\rangle \equiv |\psi_{A_3}^3\rangle = \frac{1}{\sqrt{8}}\left[((11) + (44))(c_{2\uparrow}^\dagger + c_{3\uparrow}^\dagger) - ((22) + (33))(c_{1\uparrow}^\dagger + c_{4\uparrow}^\dagger)\right]|0\rangle;$$

$$|\psi_{A_1}^1\rangle = \frac{1}{\sqrt{8}}\left[\{14\}(c_{2\uparrow}^\dagger + c_{3\uparrow}^\dagger) + \{23\}(c_{1\uparrow}^\dagger + c_{4\uparrow}^\dagger)\right]|0\rangle;$$

$$|\psi_{A_1}^2\rangle = \frac{1}{2}\left[(c_{4\uparrow}^\dagger(11) + (44)c_{1\uparrow}^\dagger) + (c_{3\uparrow}^\dagger(22) + (33)c_{2\uparrow}^\dagger)\right]|0\rangle;$$

$$|\psi_{A_1}^3\rangle = \frac{1}{\sqrt{8}}\left[((11) + (44))(c_{2\uparrow}^\dagger + c_{3\uparrow}^\dagger) + ((22) + (33))(c_{1\uparrow}^\dagger + c_{4\uparrow}^\dagger)\right]|0\rangle;$$

$$|\psi_{A_2}^1\rangle = \frac{1}{\sqrt{6}}\left[c_{2\uparrow}^\dagger c_{3\uparrow}^\dagger(c_{1\downarrow}^\dagger - c_{4\downarrow}^\dagger) - \frac{1}{2}[23](c_{1\uparrow}^\dagger - c_{4\uparrow}^\dagger)+\right.$$

$$\left. + c_{1\uparrow}^\dagger c_{4\uparrow}^\dagger(c_{2\downarrow}^\dagger - c_{3\downarrow}^\dagger) - \frac{1}{2}[14](c_{2\uparrow}^\dagger - c_{3\uparrow}^\dagger)\right]|0\rangle;$$

$$|\psi_{A_2}^2\rangle = \frac{1}{\sqrt{8}}\left[((11) - (44))(c_{2\uparrow}^\dagger - c_{3\uparrow}^\dagger) + ((22) - (33))(c_{1\uparrow}^\dagger - c_{4\uparrow}^\dagger)\right]|0\rangle;$$

$$|\psi_{A_4}^1\rangle = \frac{1}{\sqrt{6}}\left[c_{2\uparrow}^\dagger c_{3\uparrow}^\dagger(c_{1\downarrow}^\dagger - c_{4\downarrow}^\dagger) - \frac{1}{2}[23](c_{1\uparrow}^\dagger - c_{4\uparrow}^\dagger)-\right.$$

$$\left. - c_{1\uparrow}^\dagger c_{4\uparrow}^\dagger(c_{2\downarrow}^\dagger - c_{3\downarrow}^\dagger) + \frac{1}{2}[14](c_{2\uparrow}^\dagger - c_{3\uparrow}^\dagger)\right]|0\rangle;$$

$$|\psi_{A_4}^2\rangle = \frac{1}{\sqrt{8}}\left[((11) - (44))(c_{2\uparrow}^\dagger - c_{3\uparrow}^\dagger) - ((22) - (33))(c_{1\uparrow}^\dagger - c_{4\uparrow}^\dagger)\right]|0\rangle.$$

The matrix elements of $T(t, t')$ in the basis $|\psi_{1,2,3}\rangle$ have the form:

$$T = \begin{pmatrix} -(t + t') & \sqrt{2}t & -(t + 2t') \\ \sqrt{2}t & t' & -\sqrt{2}t \\ -(t + 2t') & -\sqrt{2}t & -(t + t') \end{pmatrix}$$

Finally, we list basis function for the 2D representations E with $S_z = 1/2$:

$$\begin{cases} |\psi_{E_1}^1\rangle = \frac{1}{2}\{14\}\big(c_{2\uparrow}^\dagger - c_{3\uparrow}^\dagger\big)|0\rangle; \\ |\psi_{E_1}^2\rangle = \frac{1}{2}\{23\}\big(c_{1\uparrow}^\dagger - c_{4\uparrow}^\dagger\big)|0\rangle. \end{cases}$$

$$\begin{cases} |\psi_{E_2}^1\rangle = \frac{1}{\sqrt{3}}\big[c_{1\uparrow}^\dagger c_{4\uparrow}^\dagger\big(c_{2\downarrow}^\dagger + c_{3\downarrow}^\dagger\big) - \frac{1}{2}[14]\big(c_{2\uparrow}^\dagger + c_{3\uparrow}^\dagger\big)\big]|0\rangle; \\ |\psi_{E_2}^2\rangle = \frac{1}{\sqrt{3}}\big[c_{2\uparrow}^\dagger c_{3\uparrow}^\dagger\big(c_{1\downarrow}^\dagger + c_{4\downarrow}^\dagger\big) - \frac{1}{2}[23]\big(c_{1\uparrow}^\dagger + c_{4\uparrow}^\dagger\big)\big]|0\rangle. \end{cases}$$

$$\begin{cases} |\psi_{E_3}^1\rangle = \frac{1}{\sqrt{2}}\big[(11)c_{4\uparrow}^\dagger - (44)c_{1\uparrow}^\dagger\big]|0\rangle; \\ |\psi_{E_3}^2\rangle = \frac{1}{\sqrt{2}}\big[(22)c_{3\uparrow}^\dagger - (33)c_{2\uparrow}^\dagger\big]|0\rangle. \end{cases}$$

$$\begin{cases} |\psi_{E_4}^1\rangle = \frac{1}{2}\big(c_{2\uparrow}^\dagger + c_{3\uparrow}^\dagger\big)\big[(11) - (44)\big]|0\rangle; \\ |\psi_{E_4}^2\rangle = \frac{1}{2}\big(c_{1\uparrow}^\dagger + c_{4\uparrow}^\dagger\big)\big[(22) - (33)\big]|0\rangle. \end{cases}$$

$$\begin{cases} |\psi_{E_5}^1\rangle = \frac{1}{2}\big(c_{2\uparrow}^\dagger - c_{3\uparrow}^\dagger\big)\big[(11) + (44)\big]|0\rangle; \\ |\psi_{E_5}^2\rangle = \frac{1}{2}\big(c_{1\uparrow}^\dagger - c_{4\uparrow}^\dagger\big)\big[(22) + (33)\big]|0\rangle. \end{cases}$$

3.5.2 Maximally frustrated case $t = t'$

The set of basis functions, presented in the previous subsection can be further reduced at the maximally frustrated point. Below we determine the GS in each N_e-sector.

(i) Two holes: $N_e = 2$

The 3×3 Hamiltonian matrix is block-diagonalized to 2×2 and 1×1 blocks. The 2D subspace is spanned by the wavefunctions:

$$|1\rangle = |\psi_1\rangle; \quad |2\rangle = \sqrt{\frac{1}{3}}\big(|\psi_2\rangle + \sqrt{2}|\psi_3\rangle\big).$$

The Hamiltonian matrix,

$$H_2 = \begin{pmatrix} U & -2\sqrt{3}t \\ -2\sqrt{3}t & -4t \end{pmatrix}.$$

95

has the following eigenvalues:

$$E_\pm = -2t + U/2 \pm \sqrt{(4t)^2 + 2tU + (U/2)^2}.$$

The GS energy is $\epsilon(2) = E_-$.

The remaining state, $\sqrt{2/3}\big(|\psi_2\rangle - 1/\sqrt{2}|\psi_3\rangle\big)$, represents the 1D subspace with eigenvalue $2t$.

(ii) Half-filling: $N_e = 4$

The five dimensional GS subspace is reduced to subspaces of dimensions 3 and 2. The 3D subspace is generated by the states:

$$|1\rangle = \sqrt{\frac{2}{3}}\left(|\psi_1\rangle - \frac{1}{\sqrt{2}}|\psi_2\rangle\right); \quad |2\rangle = |\psi_3\rangle; \quad |3\rangle = \sqrt{\frac{2}{3}}\left(|\psi_4\rangle - \frac{1}{\sqrt{2}}|\psi_5\rangle\right).$$

The Hamiltonian matrix can be written as:

$$H_3 = \begin{pmatrix} 2U & 0 & 2t \\ 0 & 0 & -2\sqrt{3}t \\ 2t & -2\sqrt{3}t & U \end{pmatrix}.$$

Eigenvalues of this matrix are given by:

$$E_k/2t = g + 2\sqrt{\frac{g^2 + 4}{3}} \cos\frac{\phi(g) - 2\pi(k - 1/2)}{3},$$

$$\phi(g) = \operatorname{arctg}\sqrt{\frac{1}{g^2}\left(\frac{g^2 + 4}{3}\right)^3 - 1},$$

where $g = U/2t$. The GS corresponds to $k = 2$: $\epsilon(4) = E_2$.

The 2D subspace is spanned by symmetric functions:

$$|1\rangle = \frac{1}{\sqrt{3}}\big(|\psi_1\rangle + \sqrt{2}|\psi_2\rangle\big); \quad |4\rangle = \frac{1}{\sqrt{3}}\big(|\psi_4\rangle + \sqrt{2}|\psi_5\rangle\big).$$

The Hamiltonian matrix,

$$H_2 = \begin{pmatrix} 2U & -4t \\ -4t & U \end{pmatrix}$$

has eigenvalues

$$\varepsilon = \frac{3}{2}U \pm \sqrt{(4t)^2 + (U/2)^2},$$

which describe excited states.

(iii) One hole: $N_e = 3$

In this case, there is no reduction of the basis due to higher symmetry. Using the notations introduced above we can write the Hamiltonian matrix as:

$$H_3 = \begin{pmatrix} -2t & \sqrt{2}t & -3t \\ \sqrt{2}t & t+U & -\sqrt{2}t \\ -3t & -\sqrt{2}t & -2t+U \end{pmatrix}.$$

The eigenvalues have the form:

$$E_k/t = -1 + \frac{4}{3}g + 4\sqrt{\left(\frac{2g}{3}\right)^2 + \frac{2g}{3} + \frac{16}{3}} \cos \frac{\phi(g) - 2\pi(k-1/2)}{3},$$

$$\phi(g) = \text{arctg}\sqrt{4\frac{\left[(2g/3)^2 + 2g/3 + 16/3\right]^3}{\left[4(2g/3) + 3(2g/3)^2 + 2(2g/3)^3\right]^2} - 1}.$$

Again the lowest eigenvalue is given by $k = 2$: $\epsilon(3) = E_2$.

(iv) Asymptotics

Now it is easy to analyze asymptotic behavior of the above-obtained GS energies:

- Weak coupling, $g \ll 1$:

$$\epsilon(2)/t \approx -6 + \frac{g}{2} - \frac{3g^2}{32}, \quad \epsilon(4)/t \approx -4 + \frac{3g}{2} - \frac{13g^2}{32}, \quad \epsilon(3)/t \approx -5 + g - \frac{6g^2}{32};$$

97

- Strong coupling, $g \gg 1$:

$$\epsilon(2)/t \approx -4 - \frac{6}{g}, \quad \epsilon(4)/t \approx -\frac{6}{g}, \quad \epsilon(3)/t \approx -2 - \frac{11}{2g}.$$

These expressions provide us with asymptotic behavior of the hole binding energy $\Delta = 2\epsilon(3) - \epsilon(2) - \epsilon(4)$ (see Fig. 3.2):

$$\Delta/t \approx \begin{cases} g^2/8 = U^2/32t^2; & U \ll t; \\ 1/g = 2t/U; & U \gg t. \end{cases}$$

3.6 Appendix B: Low-energy model for $t = t'$

Now we will use the results of Appendix A to construct an effective low-energy *bosonic* model (3.2) for the full lattice shown in Fig. 3.1(a).

When plaquettes are decoupled, there is a gap Δ to fermionic (single-hole) states. Thus, before deriving the effective model we need to know the number of even-N_e single-plaquette states in the gap. By diagonalizing the Hamiltonian (3.8) numerically, we find that in the sector $N_e = 2$ the GS is non-degenerate for $U \neq 0$ and all excited states reside above the gap.

In contrast, for $N_e = 4$ the GS is always two-fold degenerate. This degeneracy is apparent if one considers not only the A_1-type, but also A_2-type states. There are three of them, presented in the previous Appendix. The Hamiltonian matrix written in the basis of these states:

$$H_3^{A_2} = \begin{pmatrix} 2U & 0 & -2t \\ 0 & 0 & -2\sqrt{3}t \\ -2t & -2\sqrt{3}t & U \end{pmatrix},$$

has the same eigenvalues as H_3 already diagonalized above[1].

The Hamiltonian (3.1) can be decomposed into the single-plaquette ($H_\square$) and inter-plaquette (H_τ) parts:

$$H = \sum H_\square + H_\tau,$$

where H_τ contains an energy scale τ. We will focus on the case $\tau \ll \Delta$. In general the effective model has to be derived numerically: however in the limit $U \gg t$ this calculation can be performed analytically. Since $\Delta \sim t^2/U \ll t$ only terms of the order τ^2/Δ have to be kept and only states, which do not contain doubly occupied sites, have to be considered.

The effective Hamiltonian has a symbolic form:

$$H_{\text{eff}} = \mathcal{P} H_\tau \left(1 - \mathcal{P}\right) \frac{1}{E - H} \left(1 - \mathcal{P}\right) H_\tau \mathcal{P},$$

where $\mathcal{P}$ is the projector onto the subspace spanned by a product of half- and quarter-filled GS ($|\Omega_{N_e}\rangle$) on each plaquette. In the large-U limit these states are given by:

$$|\Omega_2\rangle = \frac{1}{\sqrt{12}} \left(\{14\} + \{23\} + \{12\} + \{13\} + \{24\} + \{34\}\right)|0\rangle;$$

$$|\Omega_4^s\rangle = \frac{1}{2}\{14\}\{23\}|0\rangle;$$

$$|\Omega_4^d\rangle = \frac{1}{\sqrt{12}} \left(2 c_{1\uparrow}^\dagger c_{4\uparrow}^\dagger c_{2\downarrow}^\dagger c_{3\downarrow}^\dagger + 2 c_{1\downarrow}^\dagger c_{4\downarrow}^\dagger c_{2\uparrow}^\dagger c_{3\uparrow}^\dagger - [14][23]\right)|0\rangle.$$

The states Ω_4^s and Ω_4^d belong to A_1 and A_2, respectively, and have s-wave and $d_{x^2-y^2}$-wave symmetries. The only allowed second-order virtual transitions are shown in Fig. 3.4(a): $2\,4_A \to 3\,3 \to 2\,4_{A'}$; $2\,4_A \to 3\,3 \to 4_{A'}\,2$ with $A = s$ or d. The virtual

---

[1] We note, that in general, $H_3^{A_2}$ does not depend on t'. At half-filling for $t' = 0$ the GS is given by its lowest eigenvalue. The fact that in the non-frustrated case the GS transforms like A_2 (and not A_1) is easy to understand using the first-order perturbation theory in U. The secular equation yields the zero-order GS in the form:

$$|\psi^{(0)}\rangle \sim c_{q_0\uparrow}^\dagger c_{q_0\downarrow}^\dagger \left(c_{q_1\uparrow}^\dagger c_{q_1\downarrow}^\dagger - c_{q_2\uparrow}^\dagger c_{q_2\downarrow}^\dagger\right)|0\rangle \sim c_{q_0\uparrow}^\dagger c_{q_0\downarrow}^\dagger \left(\{12\} + \{34\} - \{13\} - \{24\}\right)|0\rangle$$

with $q_0 = (0,0)$, $q_1 = (0,\pi)$ and $q_2 = (\pi,0)$. Clearly, this state belongs to A_2.

single-hole states are constructed from the $N_e = 3$ representations A_3 and E_1–E_5 as follows:

$$|\Omega_3^{1\sigma}\rangle = \frac{1}{\sqrt{8}}\Big[\{14\}\big(c_{2\sigma}^\dagger + c_{3\sigma}^\dagger\big) - \{23\}\big(c_{1\sigma}^\dagger + c_{4\sigma}^\dagger\big)\Big]|0\rangle;$$

$$|\Omega_3^{2\sigma}\rangle = \frac{1}{2}\Big[c_{2\sigma}^\dagger c_{3\sigma}^\dagger\big(c_{1\bar\sigma}^\dagger + c_{4\bar\sigma}^\dagger\big) + \frac{s_\sigma}{2}\{14\}\big(c_{2\sigma}^\dagger - c_{3\sigma}^\dagger\big) - \frac{1}{2}[23]\big(c_{1\sigma}^\dagger + c_{4\sigma}^\dagger\big)\Big]|0\rangle;$$

$$|\Omega_3^{3\sigma}\rangle = \frac{1}{2}\Big[c_{1\sigma}^\dagger c_{4\sigma}^\dagger\big(c_{2\bar\sigma}^\dagger + c_{3\bar\sigma}^\dagger\big) + \frac{s_\sigma}{2}\{23\}\big(c_{1\sigma}^\dagger - c_{4\sigma}^\dagger\big) - \frac{1}{2}[14]\big(c_{2\sigma}^\dagger + c_{3\sigma}^\dagger\big)\Big]|0\rangle,$$

where $\sigma(\bar\sigma) =\uparrow,\downarrow\ (\downarrow,\uparrow)$ and $s_{\uparrow,\downarrow} = \pm 1$. This phase appears in $\Omega_3^{2\sigma}$ and $\Omega_3^{3\sigma}$ because of symmetry properties of the Clebsch-Gordan coefficients. The transition matrix elements of the fermion operators are computed straightforwardly:

- Transition $|\Omega_2\rangle \to |\Omega_3\rangle$:

$$c_{i\sigma}^\dagger|\Omega_2\rangle = \frac{1}{\sqrt{12}}\sum_{j<l}{}'\{jl\}c_{i\sigma}^\dagger|0\rangle = \sum_{l=1}^{3}\langle\Omega_3^{l\sigma}|c_{i\sigma}^\dagger|\Omega_2\rangle|\Omega_3^{l\sigma}\rangle,$$

where the prime indicates absence of the i-the term in the sum. We have row-wise:

$$\langle\Omega_3^{l\sigma}|c_{1\sigma}^\dagger|\Omega_2\rangle = \left\{-\frac{1}{\sqrt{6}},\ 0,\ \frac{s_\sigma}{\sqrt{3}}\right\}; \quad \langle\Omega_3^{l\sigma}|c_{2\sigma}^\dagger|\Omega_2\rangle = \left\{\frac{1}{\sqrt{6}},\ \frac{s_\sigma}{\sqrt{3}},\ 0\right\};$$

$$\langle\Omega_3^{l\sigma}|c_{3\sigma}^\dagger|\Omega_2\rangle = \left\{\frac{1}{\sqrt{6}},\ -\frac{s_\sigma}{\sqrt{3}},\ 0\right\}; \quad \langle\Omega_3^{l\sigma}|c_{4\sigma}^\dagger|\Omega_2\rangle = \left\{-\frac{1}{\sqrt{6}},\ 0,\ -\frac{s_\sigma}{\sqrt{3}}\right\}.$$

- Transition $|\Omega_4^s\rangle \to |\Omega_3\rangle$:

$$c_{i\sigma}|\Omega_4^s\rangle = \frac{s_\sigma}{2}c_{(C_2 i),\bar\sigma}^\dagger\sum_{j<l}{}'\{jl\}|0\rangle = \sum_{l=1}^{3}\langle\Omega_3^{l\bar\sigma}|c_{i\sigma}|\Omega_4^s\rangle|\Omega_3^{l\bar\sigma}\rangle.$$

Here $C_2 i$ denotes a site opposite with respect to i, i.e. $(1,4)$ and $(2,3)$ (see Fig. 3.1(a)), and the prime means that indices i and $C_2 i$ are not included in the sums, which therefore contain only one term each. The matrix elements are

100

given by:

$$\langle\Omega_3^{l\bar\sigma}|c_{1\sigma}|\Omega_4^s\rangle = \left\{-\frac{s_\sigma}{\sqrt{8}},\ 0,\ \frac{1}{4}\right\};\quad \langle\Omega_3^{l\bar\sigma}|c_{2\sigma}|\Omega_4^s\rangle = \left\{\frac{s_\sigma}{\sqrt{8}},\ \frac{1}{4},\ 0\right\};$$

$$\langle\Omega_3^{l\bar\sigma}|c_{3\sigma}|\Omega_4^s\rangle = \left\{\frac{s_\sigma}{\sqrt{8}},\ -\frac{1}{4},\ 0\right\};\quad \langle\Omega_3^{l\bar\sigma}|c_{4\sigma}|\Omega_4^s\rangle = \left\{-\frac{s_\sigma}{\sqrt{8}},\ 0,\ -\frac{1}{4}\right\}.$$

- Transition $|\Omega_4^d\rangle \to |\Omega_3\rangle$:

$$c_{i\sigma}|\Omega_4^d\rangle = \frac{1}{\sqrt{12}}{\sum_{j<l}}'\left(c^\dagger_{(C_2i),\sigma}c^\dagger_{j\bar\sigma}c^\dagger_{l\bar\sigma} - c^\dagger_{(C_2i),\bar\sigma}[jl]\right)|0\rangle = \sum_{l=1}^{3}\langle\Omega_3^{l\bar\sigma}|c_{i\sigma}|\Omega_4^d\rangle|\Omega_3^{l\bar\sigma}\rangle,$$

where notations are the same as above. The matrix elements have the form:

$$\langle\Omega_3^{l\bar\sigma}|c_{1\sigma}|\Omega_4^d\rangle = \left\{0,\ \frac{\sqrt{3}}{4},\ 0\right\};\quad \langle\Omega_3^{l\bar\sigma}|c_{2\sigma}|\Omega_4^d\rangle = \left\{0,\ 0,\ \frac{\sqrt{3}}{4}\right\};$$

$$\langle\Omega_3^{l\bar\sigma}|c_{3\sigma}|\Omega_4^d\rangle = \left\{0,\ 0,\ -\frac{\sqrt{3}}{4}\right\};\quad \langle\Omega_3^{l\bar\sigma}|c_{2\sigma}|\Omega_4^d\rangle = \left\{0,\ -\frac{\sqrt{3}}{4},\ 0\right\}.$$

We are now in position to actually compute the second-order effective Hamiltonian H_{eff}. As already discussed in the main text we identify an Ω_2-type plaquette with the local vacuum state, $|0\rangle_i$, and an Ω_4^α-type cluster with the one boson state, $|1_\alpha\rangle_i = b^\dagger_{i\alpha}|0\rangle_i$, where $\alpha = s$ or d denotes the boson flavor. In general, there are two types of processes: boson hopping and four-boson interactions. Both may involve a flavor change. Since the two half-filled GS have different symmetries under a $\pi/4$ rotation, the amplitudes which describe a flavor change will depend on direction: there will be a phase difference of π between them. On the contrary, the diagonal matrix elements are "isotropic". Here we shall compute H_{eff} only for the tetrahedral lattice.

Let us consider the two plaquettes with numbered sites in Fig. 3.1(a) and denote the one on the left as plaquete 1 and the right one – as plaquette 2. The amplitudes corresponding to the hopping and exchange processes, shown in Fig. 3.4(a), can be computed as follows.

- Exchange: $2_1 4_2 \rightarrow 3_1 3_2 \rightarrow 2_1 4_2'$

    The first transition is realized by the operator:

    $$T_1 = -\tau_1 \sum_\sigma c^\dagger_{1,2\sigma} c_{2,3\sigma} - \tau_2 \sum_\sigma \left(c^\dagger_{1,1\sigma} c_{2,1\sigma} + c^\dagger_{1,4\sigma} c_{2,4\sigma} \right),$$

    while the second transition is effected by the conjugate $T_2 = T_1^\dagger$. In these expressions the three indices denote respectively the plaquette, a site within this plaquette, and the spin. Using the above-computed matrices of c-operators we have:

    $$T_1 |\Omega_2\rangle_1 |\Omega_4^s\rangle_2 = -\frac{1}{4\sqrt{3}} \Bigg\{ (\tau_1 + 2\tau_2) \left[|\Omega_3^{1\uparrow}\rangle_1 |\Omega_3^{1\downarrow}\rangle_2 - |\Omega_3^{1\downarrow}\rangle_1 |\Omega_3^{1\uparrow}\rangle_2 \right] - $$
    $$- \tau_1 \left[|\Omega_3^{2\uparrow}\rangle_1 |\Omega_3^{2\downarrow}\rangle_2 - |\Omega_3^{2\downarrow}\rangle_1 |\Omega_3^{2\uparrow}\rangle_2 \right] + $$
    $$+ 2\tau_2 \left[|\Omega_3^{3\uparrow}\rangle_1 |\Omega_3^{3\downarrow}\rangle_2 - |\Omega_3^{3\downarrow}\rangle_1 |\Omega_3^{3\uparrow}\rangle_2 \right] - $$
    $$- \frac{\tau_1}{\sqrt{2}} \left[|\Omega_3^{1\uparrow}\rangle_1 |\Omega_3^{2\downarrow}\rangle_2 + |\Omega_3^{1\downarrow}\rangle_1 |\Omega_3^{2\uparrow}\rangle_2 \right] + $$
    $$+ \sqrt{2}\tau_1 \left[|\Omega_3^{2\uparrow}\rangle_1 |\Omega_3^{1\downarrow}\rangle_2 + |\Omega_3^{2\downarrow}\rangle_1 |\Omega_3^{1\uparrow}\rangle_2 \right] \Bigg\}$$

    and

    $$T_1 |\Omega_2\rangle_1 |\Omega_4^d\rangle_2 = -\frac{1}{4} \Bigg\{ -\frac{\tau_1}{\sqrt{2}} \left[|\Omega_3^{1\uparrow}\rangle_1 |\Omega_3^{3\downarrow}\rangle_2 + |\Omega_3^{1\downarrow}\rangle_1 |\Omega_3^{3\uparrow}\rangle_2 \right] - $$
    $$- \tau_1 \left[|\Omega_3^{2\uparrow}\rangle_1 |\Omega_3^{3\downarrow}\rangle_2 - |\Omega_3^{2\downarrow}\rangle_1 |\Omega_3^{3\uparrow}\rangle_2 \right] + $$
    $$+ 2\tau_2 \left[|\Omega_3^{3\uparrow}\rangle_1 |\Omega_3^{2\downarrow}\rangle_2 - |\Omega_3^{3\downarrow}\rangle_1 |\Omega_3^{2\uparrow}\rangle_2 \right] \Bigg\}.$$

    Using these expressions we see that $V^{\text{eff}}_{s\leftarrow d} = V^{\text{eff}}_{d\leftarrow s} = 0$, while the diagonal matrix elements are given by the second line of Eq. (3.3).

- Hopping: $2_1 4_2 \rightarrow 3_1 3_2 \rightarrow 4_1' 2_2$

    The first process is defined by the same kinetic energy term T_1 as above. How-

ever, now the second transition is described by the same operator: $T_2 = T_1$. In order to compute t^{eff}, we need to establish how $T_1^\dagger$ acts on the final states:

$$T_1^\dagger |\Omega_4^s\rangle_1 |\Omega_2\rangle_2 = \frac{1}{4\sqrt{3}} \Big\{ -(\tau_1 + 2\tau_2) \big[|\Omega_3^{1\uparrow}\rangle_1 |\Omega_3^{1\downarrow}\rangle_2 - |\Omega_3^{1\downarrow}\rangle_1 |\Omega_3^{1\uparrow}\rangle_2 \big] +$$

$$+ \tau_1 \big[|\Omega_3^{2\uparrow}\rangle_1 |\Omega_3^{2\downarrow}\rangle_2 - |\Omega_3^{2\downarrow}\rangle_1 |\Omega_3^{2\uparrow}\rangle_2 \big] -$$

$$- 2\tau_2 \big[|\Omega_3^{3\uparrow}\rangle_1 |\Omega_3^{3\downarrow}\rangle_2 - |\Omega_3^{3\downarrow}\rangle_1 |\Omega_3^{3\uparrow}\rangle_2 \big] -$$

$$- \sqrt{2}\tau_1 \big[|\Omega_3^{1\uparrow}\rangle_1 |\Omega_3^{2\downarrow}\rangle_2 + |\Omega_3^{1\downarrow}\rangle_1 |\Omega_3^{2\uparrow}\rangle_2 \big] +$$

$$+ \frac{\tau_1}{\sqrt{2}} \big[|\Omega_3^{2\uparrow}\rangle_1 |\Omega_3^{1\downarrow}\rangle_2 + |\Omega_3^{2\downarrow}\rangle_1 |\Omega_3^{1\uparrow}\rangle_2 \big] \Big\}$$

and

$$T_1^\dagger |\Omega_4^d\rangle_1 |\Omega_2\rangle_2 = \frac{1}{4} \Big\{ \frac{\tau_1}{\sqrt{2}} \big[|\Omega_3^{3\uparrow}\rangle_1 |\Omega_3^{1\downarrow}\rangle_2 + |\Omega_3^{3\downarrow}\rangle_1 |\Omega_3^{1\uparrow}\rangle_2 \big] +$$

$$+ \tau_1 \big[|\Omega_3^{3\uparrow}\rangle_1 |\Omega_3^{2\downarrow}\rangle_2 - |\Omega_3^{3\downarrow}\rangle_1 |\Omega_3^{2\uparrow}\rangle_2 \big] -$$

$$- 2\tau_2 \big[|\Omega_3^{2\uparrow}\rangle_1 |\Omega_3^{3\downarrow}\rangle_2 - |\Omega_3^{2\downarrow}\rangle_1 |\Omega_3^{3\uparrow}\rangle_2 \big] \Big\}.$$

Again, it is easy to convince yourself that $t^{\text{eff}}_{s \leftarrow d} = t^{\text{eff}}_{d \leftarrow s} = 0$, and the diagonal hopping amplitudes are shown in the first line of Eq. (3.3).

3.7   Appendix C: HMF method for hard-core bosons

The application of the hierarchical mean-field method (HMF) developed in Chap. 2 to the boson Hamiltonian (3.2) is rather straightforward and is analogous to the way it was used for spin systems. The HMF scheme automatically includes simpler semiclassical approaches to multi-flavor hard-core boson systems [106].

Recall that the effective model (3.2) is defined on a square "superlattice", formed

by the tetrahedra (see Fig. 3.1(a)). Therefore, a natural cluster degree of freedom is a four-site square. The entire superlattice is covered by these blocks as shown in Fig. 2.1(b) (with $J_2 = 0$, of course). With the aid of Eq. (3.3) the Hamiltonian (3.2) can be written as:

$$H = -\sum_{\substack{\langle ij \rangle \\ \sigma=s,d}} t_\sigma \left(b_{i\sigma}^\dagger b_{j\sigma} + b_{j\sigma}^\dagger b_{i\sigma}\right) + (V_s + V_d)\sum_{\langle ij \rangle} n_i n_j -$$
$$- \frac{V_s - V_d}{2}\sum_{\langle ij \rangle}\left[(1 - n_i)S_j^z + (1 - n_j)S_i^z\right] - \mu\sum_i n_i = H_\square + H_{\text{int}},$$

where $V_\sigma = V_{\sigma\sigma}$, $t_\sigma = t_{\sigma\sigma}$, $S_i^z = n_{is} - n_{id}$, and $H_\square$ and H_{int} describe isolated clusters and intercluster interaction, respectively. Using the site numbering, shown in Fig. 2.1(b), we represent these two terms in the form (see Sec. 2.2):

$$H_\square = -\sum_\sigma t_\sigma \left[(b_{1\sigma}^\dagger + b_{4\sigma}^\dagger)(b_{2\sigma} + b_{3\sigma}) + (b_{2\sigma}^\dagger + b_{3\sigma}^\dagger)(b_{1\sigma} + b_{4\sigma})\right] +$$
$$+ \left(V_s + V_d\right)\left(n_1 + n_4\right)\left(n_2 + n_3\right) - \mu\left(n_1 + n_4 + n_2 + n_3\right) -$$
$$- \frac{V_s - V_d}{2}\left\{\left[(1 - n_1) + (1 - n_4)\right]\left(S_2^z + S_3^z\right) + \left[(1 - n_2) + (1 - n_3)\right]\left(S_1^z + S_4^z\right)\right\}$$

and

$$H_{\text{int}} = -\sum_\sigma \frac{t_\sigma}{4}\left[(b_{1\sigma}^\dagger b_{7\sigma} + \text{sym}) + (b_{2\sigma}^\dagger b_{8\sigma} + \text{sym}) + (b_{3\sigma}^\dagger b_{5\sigma} + \text{sym}) + (b_{4\sigma}^\dagger b_{6\sigma} + \text{sym}) +\right.$$
$$\left. + (b_{2\sigma}^\dagger b_{5\sigma} + \text{sym}) + (b_{4\sigma}^\dagger b_{7\sigma} + \text{sym}) + (b_{1\sigma}^\dagger b_{6\sigma} + \text{sym}) + (b_{3\sigma}^\dagger b_{8\sigma} + \text{sym})\right] +$$
$$+ \frac{V_s + V_d}{4}\left[(n_1 + n_4)(n_6 + n_7) + (n_2 + n_3)(n_5 + n_8)\right] -$$
$$- \frac{V_s - V_d}{8}\left\{\left[(1 - n_1)S_7^z + \text{sym}\right] + \left[(1 - n_2)S_8^z + \text{sym}\right] +\right.$$
$$+ \left[(1 - n_2)S_5^z + \text{sym}\right] + \left[(1 - n_4)S_7^z + \text{sym}\right] +$$
$$+ \left[(1 - n_3)S_5^z + \text{sym}\right] + \left[(1 - n_4)S_6^z + \text{sym}\right] +$$
$$\left. + \left[(1 - n_1)S_6^z + \text{sym}\right] + \left[(1 - n_3)S_8^z + \text{sym}\right]\right\},$$

where "sym" denotes terms with interchanged site indices, e.g. in the first line it means $b_{7\sigma}^{\dagger} b_{1\sigma}$, etc.

Following the prescription of Chap. 2, the state of the entire system is written as a direct product of single-cluster ground states:

$$|\text{GS}\rangle = \prod_{\text{cl}} |\psi_0\rangle = \prod_{\text{cl}} \left(\sum_a R_a |a\rangle \right),$$

where $\{|a\rangle,\ a = 1 \ldots 3^4\}$ is a basis in the Fock space of a cluster and R_a are variational parameters. Minimizing the expectation value $\langle \text{GS} | H_\square + H_{\text{int}} | \text{GS} \rangle$ with respect to these parameters, we arrive at the self-consistent equation similar to Eq. (2.5). Its numerical solution leads to the phase diagram shown in Fig. 3.4(b).

Chapter 4

Magneto-electric coupling in charge-frustrated multiferroics

In this chapter we discuss magneto-electric phenomena in charge-ordered multiferroic materials. By constructing a minimal effective model which incorporates lattice frustration, unscreened Coulomb and superexchange interactions, and spin-orbit effects, we show that:

- The order-from-disorder mechanism stabilizes a ferroelectric charge ordering;

- Double exchange and spin-orbit interactions lead to a multiferroic phase characterized by coupled collinear ferrimagnetism and ferroelectricity;

- This coupling is manifested in a finite magneto-electric coefficient, which is strongly enhanced around the ferrimagnetic transition temperature.

4.1 Introduction

Order-from-disorder is a fundamental physical mechanism through which an ordered ground state (GS) is selected out of a degenerate classical manifold by quantum or thermal fluctuations. This mechanism is best known in the theory of frustrated magnets [13], where the classical GS degeneracy is caused by lattice frustration or conflicting interactions. However, the order-from-disorder physics also manifests itself in itinerant systems, for instance in the double-exchange model [107]. Another class of systems where quantum and thermal fluctuations play a central role in stabilizing an ordered GS is the so-called charge-frustrated multiferroics, whose ferroelectric properties result from the charge-ordering, i.e. formation of the charge-density wave (CDW) [28, 108] state. A representative family of materials are the triangular lattice compounds RFe_2O_4 with R being a rare-earth element.

Out of this family, perhaps the most well-characterized member is the lutetium-based $LuFe_2O_4$ [30, 31]. As we already mentioned in Sec. 1.1.4, this material has a layered structure with three FeO triangular double layers (TLL) per tetragonal unit cell (see Fig. 1.5(a)). Since the nominal iron valence is $+2.5$, there are equal amounts of Fe^{2+} and Fe^{3+} ions within each TLL. In the temperature interval $320\,K \lesssim T \lesssim T_0 = 500\,K$ X-ray measurements indicate the presence of a two-dimensional commensurate CDW [30]. Below $T_{CO} \approx 320\,K$ the interplay between lattice frustration, Coulomb repulsion, and thermal fluctuation leads to a slightly ($\sim 8\%$) incommensurate charge ordering accompanied by the charge redistribution between individual layers [31, 109, 110, 111, 112]. Therefore, each TLL aquires a macroscopic electric polarization. At $T_N \approx 250\,K$ the ferrimagnetic (FiM) order emerges [113, 114] and the system becomes multiferroic. The pronounced anomaly in the electric polarization curve [31] around T_N (see Fig. 1.5(b)) suggests a significant coupling between the charge and magnetic orders [115]. Indeed, the electric control of magnetization was realized in [116], and the magnetic-field control of charge ordering was demonstrated in [117].

Discovery of these intriguing properties stimulated a surge of theoretical activity. The stability of charge ordering in LuFe$_2$O$_4$ and its coupling to magnetism was investigated in [118, 119] using *ab initio* and Monte-Carlo simulations, and in [120] within the Landau theory. In Refs. [121, 122] an effective model approach was used and it was demonstrated that emergence of the FiM order indeed strongly enhances the electric polarization, in agreement with experimental observations.

However, in the analysis of [121, 122] two important ingredients were missing. First, the authors neglected quantum fluctuations associated with charge transfer processes, which led to subtle stability of the CDW order at low temperatures. The importance of electron hopping terms in the model Hamiltonian was later highlighted in [108], where quantum fluctuations were shown to actually stabilize the "correct" charge structure. Second, the authors ignored the spin-orbit (SO) interaction in iron, and concluded that the Fe^{2+} ions possess an orbital degree of freedom which orders at low temperature. However, the single-atom SO coupling constant for Fe is quite sizable compared to both T_{CO} and T_N: $\Delta_{SO} \sim 0.0043\,Ry \sim 0.01\,eV \sim 100\,K$ [123]. The SO coupling lifts the orbital degeneracy of Fe^{2+} and causes the easy-axis magnetic anizotropy in LuFe$_2$O$_4$ [112].

In the present chapter we revisit the problem of charge ordering and magneto-electric phenomena in frustrated ferroelectrics. Using LuFe$_2$O$_4$ as a prototype, we present a theory of multiferroic behavior, which takes into account the Coulomb interaction, magnetic superexchange and spin-orbit effects, and focuses on the interplay between quantum fluctuations and geometric frustration. By identifying the relevant energy scales we derive a minimal multi-band effective model which includes coupled charge and spin degrees of freedom, and investigate its phase diagram. We show that order-from-disorder stabilizes a charge ordering with a finite electric polarization. Due to the double-exchange mechanism the onset of the FiM order leads to an anomaly in the temperature dependence of the electric polarization, qualitatively

similar to the observations of Ref. [31] (Fig. 1.5(b)). We also demonstrate that in this temperature region around T_N the electric polarization of the system is very sensitive to an external magnetic field.

4.2 Low-energy theory

In this section we shall formulate an effective model which contains basic physical ingredients, necessary to describe multiferroic properties of charge-frustrated materials. Although the present study is motivated by $LuFe_2O_4$, we emphasize that our main goal is illustration of the physical mechanism responsible for multiferroic properties of this and related compounds, and not fitting of the experimental data. Therefore, our presentation will ignore certain properties of $LuFe_2O_4$. For example, we focus on a single TLL, and disregard inter-TLL charge transfer and exchange coupling. This approximation is justified because of the large separation between two neighboring TLLs[1].

4.2.1 Energy scales

In each TLL there are equal amounts of iron ions Fe^{2+} and Fe^{3+} with electronic configurations $[Ar]3d^54s^0$ and $[Ar]3d^64s^0$, respectively. The atomic terms are determined using Hund's rules [4]: $^6S_{5/2}$ for Fe^{3+} and $^5D_4$ for Fe^{2+}. We consider the corresponding Coulomb energy scale, E_H, as a dominant energy scale in the problem.

An iron ion experiences a crystal field with the symmetry group D_{3d} ($R\bar{3}m$). Consequently the $3d$ shell is split into two doublets and one singlet [4]. The doublets have the symmetry $\{d_{x^2-y^2}, d_{xy}\} \sim Y_{2,\pm2}$ and $\{d_{xz}, d_{yz}\} \sim Y_{2,\pm1}$ (Y_{lm} are the spherical harmonics). The singlet transforms like $3z^2 - r^2 \sim Y_{1,0}$. The separation between these three groups of states, Δ_{cr}, is the second dominant energy in the problem.

---

[1] However, the inter-TLL coupling is relevant for stabilizing the observed three-dimensional anti-ferroelectric order [110] and spin structures [113] in $LuFe_2O_4$.

There seems to be an uncertainty regarding orbital symmetry of the ground state (GS) doublet. In [118] and [111] the lowest doublet is claimed to have $L = 2$ and $M_L = \pm 2$, i.e. $\{d_{x^2-y^2}, d_{xy}\}$. However, the X-ray absorption measurements presented in [112] indicate that the doublet is actually $\{d_{xz}, d_{yz}\}$ with $L = 2$ and $M_L = \pm 1$. This distinction is important, because in general the hopping of a d-electron between two Fe ions proceeds through the $2p$ shell of the neighboring oxygen atom, and the corresponding amplitude, of course, depends on the symmetry of the iron GS. Since we are not interested in close modelling of a particular material, below it is assumed that the GS doublet has a $\{d_{x^2-y^2}, d_{xy}\}$ symmetry. Moreover, we neglect the spin-orbit (SO) coupling in oxygen. Thus, in the process of hopping between two iron ions, the electron spin is preserved.

On the contrary, the SO interaction in Fe is quite large compared to the exchange interactions, as we already noted above. Since the Fe^{3+} term has $L = 0$ it remains unaffected by the SO coupling. However, the Fe^{2+} D-term will split. There are $2(2S+1) = 10$ states of the low-valence iron. Within this subspace the SO Hamiltonian, $H_{SO} = -\Delta_{SO}(\boldsymbol{L}\boldsymbol{S})$, has eigenvalues[2] $\epsilon_{M_S} = -M_L M_S \Delta_{SO}$ with $M_L = \pm 2$ and $M_S = -2 \ldots 2$. The lowest doublet has maximum absolute values of both M_L and M_S. Thus, the SO interaction lifts the orbital degeneracy of a Fe^{2+} ion, with the separaton between splitted states being $\sim \Delta_{SO}$. In order to simplify our analysis we only consider the two lowest Fe^{2+} states and ignore the rest. This assumption is justified if the bandwidth t is smaller than the SO splitting, which is certainly true in the insulating phase of $LuFe_2O_4$.

To summarize, there are three dominant energy scales in the problem: $E_H \gg \Delta_{cr} \gg \Delta_{SO}$. We also assume that all of these energies are large compared to the bandwidth, at least in the interesting part of the phase diagram, where $LuFe_2O_4$ is an insulator.

---

[2]Since the outer d-shell is more than half-filled, Δ_{SO} is positive.
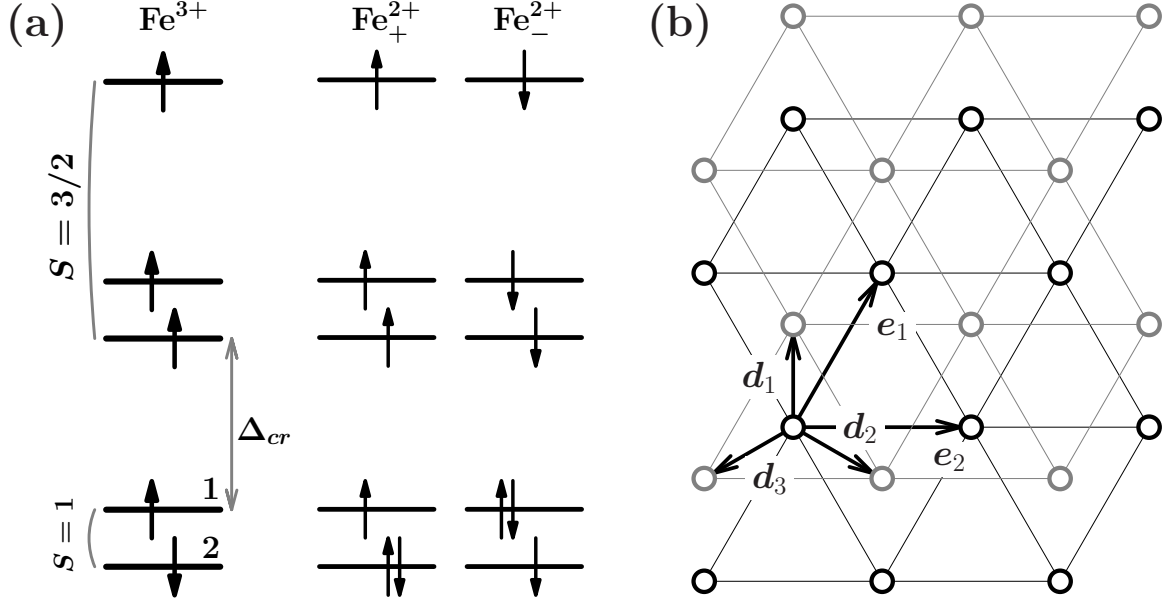
Figure 4.1: (a) The Fe $3d$ orbital, split by the crystal field (splitting Δ_{cr}). Left: $^{6}S_{5/2}$ Fe^{3+} term. High-energy core states have total spin $3/2$, while two lowest states combine into a $S = 1$ multiplet. Right: Two degenerate low-energy Fe^{2+} configurations. Degenerate states 1 and 2 have $M_L = \mp 2$. (b) Triangular double layer with $2N$ sites. Gray (black) color denotes the bottom (top) layer. Vectors $\boldsymbol{e}_{1,2}$ constitute the Bravais basis. Vectors $\boldsymbol{d}_i$ connect inter-layer NN sites and are defined as $\boldsymbol{d}_1 = \frac{1}{3}(2\boldsymbol{e}_1 - \boldsymbol{e}_2)$, $\boldsymbol{d}_2 = \frac{1}{3}(2\boldsymbol{e}_2 - \boldsymbol{e}_1)$ and $\boldsymbol{d}_3 = -\frac{1}{3}(\boldsymbol{e}_1 + \boldsymbol{e}_2)$. The z-axis is perpendicular to the TLL.

4.2.2 Local Hilbert space and degrees of freedom

The states of a Fe^{3+} ion with $S = 5/2$ can be classified according to the total spin projection and written using Clebsh-Gordan coefficients [56]:

$$\left|\frac{5}{2}, \pm\frac{5}{2}\right\rangle = \left|\frac{3}{2}, \pm\frac{3}{2}\right\rangle |1, \pm 1\rangle;$$

$$\left|\frac{5}{2}, \pm\frac{3}{2}\right\rangle = \sqrt{\frac{2}{5}}\left|\frac{3}{2}, \pm\frac{3}{2}\right\rangle |1, 0\rangle + \sqrt{\frac{3}{5}}\left|\frac{3}{2}, \pm\frac{1}{2}\right\rangle |1, \pm 1\rangle; \qquad (4.1)$$

$$\left|\frac{5}{2}, \pm\frac{1}{2}\right\rangle = \sqrt{\frac{1}{10}}\left|\frac{3}{2}, \pm\frac{3}{2}\right\rangle |1, \mp 1\rangle + \sqrt{\frac{3}{5}}\left|\frac{3}{2}, \pm\frac{1}{2}\right\rangle |1, 0\rangle + \sqrt{\frac{3}{10}}\left|\frac{3}{2}, \mp\frac{1}{2}\right\rangle |1, \pm 1\rangle.$$

with $S = 1$ states given by:

$$|1, -1\rangle = c_{1\downarrow}^{\dagger} c_{2\downarrow}^{\dagger} |0\rangle; \quad |1, 0\rangle = \frac{1}{\sqrt{2}}\left(c_{1\uparrow}^{\dagger} c_{2\downarrow}^{\dagger} + c_{1\downarrow}^{\dagger} c_{2\uparrow}^{\dagger}\right)|0\rangle; \quad |1, 1\rangle = c_{1\uparrow}^{\dagger} c_{2\uparrow}^{\dagger} |0\rangle, \qquad (4.2)$$

where operators $c^\dagger_{1,2\sigma}$ create an electron in the state 1 or 2 with spin $\sigma = \uparrow, \downarrow$ (see left panel in Fig. 4.1(a)) and $|0\rangle$ is the vacuum state. We shall denote the above six states as $\left|\mathrm{Fe}^{3+}_\alpha\right\rangle$ with $\alpha = -5/2 \ldots 5/2$. There are two low-energy degenerate configurations for the Fe^{2+} ion: with $M_S = \pm 2$, shown in the two right panels of Fig. 4.1(a). These will be denoted as $\left|\mathrm{Fe}^{2+}_\pm\right\rangle$. It follows that per site within a TLL there are $2 + 6 = 8$ states.

When choosing degrees of freedom which parametrize states within local Hilbert space it is important to take into account not only the local, i.e. generalized exclusion principle, but also the exchange statistics [101]. In other words, one should decide whether operator degrees of freedom, which belong to different sites, commute or anticommute. We remind that *physical* processes in our problem amount to hopping of a *real* electron between two iron ions. As a result of this process, the state and/or valence of an ion changes, but there is no transport of the ion as a whole. Hence, it is not straightforward to choose either fermionic, or bosonic language. Such choice, in general, depends on the approximation and desired physical observables. For instance, a bosonic language lends itself to a semiclassical approximation.

Since it is always easier to work with finite-dimensional Hilbert spaces, here we choose to represent states of both ions as Schwinger fermions [57]. First, we identify an empty site i with the local vacuum $|0\rangle_i$. The states of an Fe^{2+} ion then correspond to a pseudospin-1/2 Schwinger fermion $c_{i\zeta}$:

$$\left|\mathrm{Fe}^{2+}_\zeta\right\rangle_i = c^\dagger_{i\zeta}|0\rangle_i$$

with $\zeta = \pm$. The states of a spin-5/2 Fe^{3+} ion are represented by 6-flavored Schwinger fermions $f_{i\alpha}$:

$$\left|\mathrm{Fe}^{3+}_\alpha\right\rangle_i = f^\dagger_{i\alpha}|0\rangle_i.$$

Since each site must be occupied either by Fe^{2+} or Fe^{3+}, these operators obey the

constraint:

$$\sum_{\zeta=\pm} c_{i\zeta}^{\dagger}c_{i\zeta} + \sum_{\alpha=-5/2}^{5/2} f_{i\alpha}^{\dagger}f_{i\alpha} = 1. \tag{4.3}$$

4.2.3 Effective model

As we already mentioned, the physical processes involve hopping of a real electron between lowest $3d$ orbitals of the neighboring iron ions. In Fig. 4.1(a) these states are denoted as 1 and 2. For simplicity, we shall assume that amplitudes for the electron hopping $1\sigma \to 1\sigma$ and $1\sigma \to 2\sigma$ are identical and equal to t.

There are two types of *effective* low-energy processes: (i) charge transfer

$$\left|\mathrm{Fe}^{2+}\right\rangle_{i}\left|\mathrm{Fe}^{3+}\right\rangle_{j} \to \left|\mathrm{Fe}^{3+}\right\rangle_{i}\left|\mathrm{Fe}^{2+}\right\rangle_{j},$$

and (ii) various exchanges

$$\left|\mathrm{Fe}^{n+}\right\rangle_{i}\left|\mathrm{Fe}^{m+}\right\rangle_{j} \to \left|\mathrm{Fe}^{n+}\right\rangle_{i}\left|\mathrm{Fe}^{m+}\right\rangle_{j}$$

with n and m equal to 2 or 3. Derivation of the corresponding matrix elements is given in Appendix A at the end of this chapter. Here we just present the final expression for the effective Hamiltonian:

$$H_{\mathrm{eff}} = -\sum_{\substack{l,l'=1,2 \\ \langle ij \rangle, \zeta}} t_{ll'} \left[c_{l,i\zeta}^{\dagger}c_{l',j\zeta}\left(f_{l,i\frac{5\zeta}{2}}^{\dagger}f_{l',j\frac{5\zeta}{2}}^{\dagger} + \frac{1}{5}f_{l,i\frac{3\zeta}{2}}^{\dagger}f_{l',j\frac{3\zeta}{2}}^{\dagger} \right) - \right.$$
$$\left. - \frac{1}{\sqrt{5}}c_{l,i\zeta}^{\dagger}c_{l',j\bar{\zeta}}\left(f_{l,i\frac{3\zeta}{2}}^{\dagger}f_{l',j\frac{5\bar{\zeta}}{2}}^{\dagger} + f_{l,i\frac{5\zeta}{2}}^{\dagger}f_{l',j\frac{3\bar{\zeta}}{2}}^{\dagger} \right) + \mathrm{h.c.} \right] + \tag{4.4}$$
$$+ \sum_{\substack{l,l' \\ \langle ij \rangle}} \left[V_{ll'}n_{l,i}^{c}n_{l',j}^{c} + J_{ll'}^{33}\left(\boldsymbol{S}_{l,i}\boldsymbol{S}_{l',j} - S^{2}n_{l,i}^{f}n_{l',j}^{f} \right) - J_{ll'}^{22}s_{l,i}^{z}s_{l',j}^{z} + J_{ll'}^{23}\left(S_{l,i}^{z}s_{l',j}^{z} + s_{l,i}^{z}S_{l',j}^{z} \right) \right],$$

where l, $l' = 1,2$ label layers, $\bar{\zeta} = -\zeta$, $\langle ij \rangle$ denote inter- and intra-layer nearest-neighbor (NN) links, depending on the values of l and l' (see Fig. 4.1(b)), the sums

113

extend over all *links*, and $S = 5/2$.

In general, the model (4.4) has 10 independent parameters: $X_{ll'} = x\delta_{ll'} + x'\sigma^x_{ll'}$ with $X = \{t, V, J^{33}, J^{23}, J^{22}\}$, and x and x' being intra- and inter-layer couplings, respectively. The correlated hopping amplitudes, $t_{ll'}$, describe charge transfer processes. The V-term corresponds to an unscreened NN Coulomb repulsion $V_{ll'}$ between Fe^{2+} ions. The rest of the terms in Eq. (4.4) have a magnetic origin: $J^{33}_{ll'}$, the antiferromagnetic Heisenberg interactions between NN core Fe^{3+} spins $\boldsymbol{S}_{l,i} = \boldsymbol{S}_{\alpha'\alpha} f^\dagger_{l,i\alpha'} f_{l,i\alpha}$; $J^{23}_{ll'}$ and $J^{22}_{ll'}$, Ising-like NN terms between Fe^{3+} and Fe^{2+} spins $s^z_{l,i} = n^c_{l,i+} - n^c_{l',i-}$ (with $n^c_{l,i\zeta} = c^\dagger_{l,i\zeta} c_{l,i\zeta}$ and similarly for $n^f_{l,i\alpha}$). All J^{nm} are positive. As explained in Appendix A, signs of Fe^{2+}-Fe^{2+} and Fe^{2+}-Fe^{3+} exchange interactions are ferro- and antiferromagnetic, respectively. The Ising terms are a manifestation of the SO-related easy-axis magnetic anisotropy: the (real) spin at each Fe^{2+} site is ± 2 and cannot be flipped by a single electron transfer (thus, there are no XY-terms). The fractional coefficients in the hopping part of Eq. (4.4) (first two lines) appear because of the Clebsch-Gordan coefficients for combining spins 1 and 3/2 into the spin-5/2 Fe^{3+} core (see Eq. (4.1)). Finally, we note that the model, thus obtained, is physically very similar to the strong Hund coupling limit of the quantum Kondo lattice Hamiltonian, discussed in [124].

4.3   Mean-field approximation

The effective Hamiltonian (4.4) describes an interacting system of fermions, coupled to spin-5/2 degrees of freedom. In order to unveil its phase diagram, one has to resort to approximate techniques. Here we use a simple Hartree-Fock-like mean-field (MF) decoupling, which is nevertheless sufficient to capture the interplay between electric and magnetic orderings. This approximation is guided by experiments in $LuFe_2O_4$. In particular, we assume the observed periodicity of charge ordering in the GS. In

the reciprocal lattice basis, generated by $\{e_i\}$ (Fig. 4.1(b)), the ordering wavevector is given by:

$$\boldsymbol{Q}_0 = \left(\frac{2\pi}{3}, \frac{4\pi}{3}\right). \tag{4.5}$$

We note that in the limit, when only $V \neq 0$ in Eq. (4.4), there exist other degenerate GSs with a different set of $\boldsymbol{Q}$-vectors [122]. However, hopping terms and exchange interactions in (4.4) lift this degeneracy and select a GS with the wavevector (4.5) [108].

Let us define the Fourier-transformed operators as:

$$c_{l,i\zeta} = \frac{1}{\sqrt{N}} \sum_{\boldsymbol{k}} e^{i\boldsymbol{k}\boldsymbol{x}_i^l} c_{l,\boldsymbol{k}\zeta}$$

with N being the number of sites per layer (thus, there are $2N$ sites in a TLL). Then, our MF theory is parametrized by the following expectation values:

$$C_{\zeta'\zeta}^{l'l}(\boldsymbol{k}\boldsymbol{Q}) = \langle c_{l',\boldsymbol{k}\zeta'}^{\dagger} c_{l,\boldsymbol{k}+\boldsymbol{Q}\zeta} \rangle, \quad F_{\alpha'\alpha}^{l'l}(\boldsymbol{k}\boldsymbol{Q}) = \langle f_{l',\boldsymbol{k}\alpha'}^{\dagger} f_{l,\boldsymbol{k}+\boldsymbol{Q}\alpha} \rangle, \tag{4.6}$$

where $\boldsymbol{Q} = (0, \pm \boldsymbol{Q}_0)$ and $\langle \cdots \rangle$ denotes the thermal average $\langle A \rangle = \text{Tr}\, wA$ with w being the density matrix (Gibbs distribution). Note the absence of mixed averages of the form $\langle c_{l',\boldsymbol{k}\zeta'}^{\dagger} f_{l,\boldsymbol{k}+\boldsymbol{Q}\alpha} \rangle$. This guarantees that the physical picture, discussed below, remains unchanged, should a bosonic language have been chosen instead of a fermionic (i.e. $f_{l,i\alpha}$) one.

In terms of averages (4.6), the MF Hamiltonian for each fermion type can be written as:

$$H_{MF}^c = \sum_{\boldsymbol{k}\boldsymbol{Q}} \varphi_{l'\zeta',l\zeta}^c(\boldsymbol{k},\boldsymbol{Q}) c_{l',\boldsymbol{k}+\boldsymbol{Q}\zeta'}^{\dagger} c_{l,\boldsymbol{k}\zeta}, \quad H_{MF}^f = \sum_{\boldsymbol{k}\boldsymbol{Q}} \varphi_{l'\alpha',l\alpha}^f(\boldsymbol{k},\boldsymbol{Q}) f_{l',\boldsymbol{k}+\boldsymbol{Q}\alpha'}^{\dagger} f_{l,\boldsymbol{k}\alpha} \tag{4.7}$$

with

$$
\varphi^c_{l'\zeta',l\zeta}(\boldsymbol{k},\boldsymbol{Q}) = -\frac{t_{l'l}}{N}\sum_{\boldsymbol{q}}\Gamma^{l'l}_{\boldsymbol{k}-\boldsymbol{q}}\Bigg\{\delta_{\zeta'\zeta}\bigg[F^{ll'}_{\frac{5\zeta}{2}\frac{5\zeta}{2}}(\boldsymbol{q}\boldsymbol{Q}) + \frac{1}{5}F^{ll'}_{\frac{3\zeta}{2}\frac{3\zeta}{2}}(\boldsymbol{q}\boldsymbol{Q})\bigg]-
$$

$$
-\frac{\delta_{\zeta'\bar\zeta}}{\sqrt5}\bigg[F^{ll'}_{\frac{3\zeta}{2}\frac{5\bar\zeta}{2}}(\boldsymbol{q}\boldsymbol{Q}) + F^{ll'}_{\frac{5\zeta}{2}\frac{3\bar\zeta}{2}}(\boldsymbol{q}\boldsymbol{Q})\bigg]\Bigg\}+
$$

$$
+\frac{\delta_{l'l}}{N}\sum_{\boldsymbol{q},l''}\Gamma^{ll''}_{\boldsymbol{Q}}\Big\{\delta_{\zeta'\zeta}\big[V_{ll''}\delta_{\zeta_1\zeta_2} - J^{22}_{ll''}\sigma^z_{\zeta_1\zeta_2}\big]C^{l''l''}_{\zeta_1\zeta_2}(\boldsymbol{q}\boldsymbol{Q}) + J^{23}_{ll''}\sigma^z_{\zeta'\zeta}S^z_{\alpha'\alpha}F^{l''l''}_{\alpha'\alpha}(\boldsymbol{q}\boldsymbol{Q})\Big\}-
$$

$$
-\frac{1}{N}\sum_{\boldsymbol{q}}\Gamma^{l'l}_{\boldsymbol{k}-\boldsymbol{q}}\big[V_{l'l}\delta_{\zeta\zeta_1}\delta_{\zeta'\zeta_2} - J^{22}_{l'l}\sigma^z_{\zeta\zeta_1}\sigma^z_{\zeta'\zeta_2}\big]C^{ll'}_{\zeta_1\zeta_2}(\boldsymbol{q}\boldsymbol{Q}),
$$

and

$$
\varphi^f_{l'\alpha',l\alpha}(\boldsymbol{k},\boldsymbol{Q}) = -\frac{t_{l'l}}{N}\sum_{\boldsymbol{q},\zeta}\Gamma^{l'l}_{\boldsymbol{k}-\boldsymbol{q}}\Bigg\{\delta_{\alpha'\alpha}\bigg[\delta_{\alpha\frac{5\zeta}{2}} + \frac{1}{5}\delta_{\alpha\frac{3\zeta}{2}}\bigg]C^{ll'}_{\zeta\zeta}(\boldsymbol{q}\boldsymbol{Q})-
$$

$$
-\frac{1}{\sqrt5}\big[\delta_{\alpha'\frac{5\bar\zeta}{2}}\delta_{\alpha\frac{3\zeta}{2}} + \delta_{\alpha'\frac{3\bar\zeta}{2}}\delta_{\alpha\frac{5\zeta}{2}}\big]C^{ll'}_{\zeta\bar\zeta}(\boldsymbol{q}\boldsymbol{Q})\Bigg\}+
$$

$$
+\frac{\delta_{l'l}}{N}\sum_{\boldsymbol{q},l''}\Gamma^{ll''}_{\boldsymbol{Q}}\Big\{J^{23}_{ll''}S^z_{\alpha'\alpha}\sigma^z_{\zeta'\zeta}C^{l''l''}_{\zeta'\zeta}(\boldsymbol{q}\boldsymbol{Q}) + J^{33}_{ll''}v^{\alpha'\alpha_1}_{\alpha\alpha_2}F^{l''l''}_{\alpha_1\alpha_2}(\boldsymbol{q}\boldsymbol{Q})\Big\}-
$$

$$
-\frac{J^{33}_{l'l}}{N}\sum_{\boldsymbol{q}}\Gamma^{l'l}_{\boldsymbol{k}-\boldsymbol{q}}v^{\alpha'\alpha_1}_{\alpha_2\alpha}F^{ll'}_{\alpha_1\alpha_2}(\boldsymbol{q}\boldsymbol{Q}),
$$

where we assume summation over repeated indices, and

$$
v^{\alpha'\beta'}_{\alpha\beta} = \boldsymbol{S}_{\alpha'\alpha}\boldsymbol{S}_{\beta'\beta} - S^2\delta_{\alpha'\alpha}\delta_{\beta'\beta},\quad \Gamma^{l'l}_{\boldsymbol{k}} = \sum_{\boldsymbol{d}_{l'l}}\Big(e^{i\boldsymbol{d}_{l'l}\boldsymbol{k}} + e^{-i\boldsymbol{d}_{ll'}\boldsymbol{k}}\Big),
$$

$\boldsymbol{d}_{ll} = \{\boldsymbol{e}_i\}$ and $\boldsymbol{d}_{12} = -\boldsymbol{d}_{21} = \{\boldsymbol{d}_i\}$ (see Fig. 4.1(b)).

The MF approximation replaces the exact local constraint (4.3) with a requirement to conserve an average particle number. Since there are equal amounts of Fe^{2+} and Fe^{3+} ions in a TLL, we have:

$$
\frac{1}{N}\sum_{l,i,\zeta}\langle n^c_{l,i\zeta}\rangle = \frac{1}{N}\sum_{l,i,\alpha}\langle n^f_{l,i\alpha}\rangle = 1.
$$

To satisfy this condition, we introduce two chemical potentials, μ_c and μ_f, into the MF Hamiltonian. The double site occupancy, which becomes possible at the MF level, is eliminated by adding local repulsion (Hubbard-like) terms between all fermion species, with a large value of U. Collecting all above contributions, the full MF Hamiltonian can be written as:

$$H_{MF} = H_{MF}^c + H_{MF}^f - \mu_c \sum_{l,i,\zeta} n_{l,i\zeta}^c - \mu_f \sum_{l,i,\alpha} n_{l,i\alpha}^f + U \sum_i \left(n_i^c n_i^c + n_i^f n_i^f + n_i^c n_i^f \right).$$

This Hamiltonian can now be diagonalized self-consistently on a finite TLL. Various observables are determined in terms of the converged averages (4.6). The primary quantity of interest for us is the electric polarization, defined as an absolute value of the inter-layer charge imbalance (z-axis points perpendicular to the TLL), i.e.:

$$P_z = \frac{1}{N} \left| \sum_{\boldsymbol{q},\zeta} \left[C_{\zeta\zeta}^{11}(\boldsymbol{q}0) - C_{\zeta\zeta}^{22}(\boldsymbol{q}0) \right] \right|. \tag{4.8}$$

4.4   Results

We performed numerical self-consistent diagonalization of H_{MF} in a $N \times N$ TLL with $N = 12$ and periodic boundary conditions in the xy plane[3]. This system size is sufficient to approximate the thermodynamic limit, because the characteristic CDW unit cell, shown in Fig. 1.5(c) has dimensions $\sqrt{3} \times \sqrt{3}$. In fact, quantities, like chemical potentials, do not show any size dependence for larger values of N. At all times, we keep the wavevector of the charge and spin density-wave equal to $\boldsymbol{Q}_0$.

The model (4.4) has a rich phase diagram, because of the large number of free parameters (see discussion after Eq. (4.4)), whose investigation is quite complicated and, for instance, requires relaxing the constraint on possible values of $\boldsymbol{Q}$. Some

---

[3]We note, that since our system is *not* periodic in the z-direction, only P_z is well-defined. Polarizations in the x and y directions are in general not uniquely defined and are quite tedious to compute (see [125] for details).

discussion along these lines can be found in [122]. Since in the present work we have a particular goal of understanding mechanism of the feedback, provided by magnetic order on the electric polarization, below we shall fix parameters in H_{eff} to certain physically sane values and study the temperature-dependent phase diagram of the model.

In units of the intra-layer hopping t, the parameters of H_{eff} are as follows (the primed quantities were defined after Eq. (4.4)):

$$
\begin{pmatrix}
t' \\
\{V, V'\} \\
\{J^{33}, J'^{33}\} \\
\{J^{22}, J'^{22}\} \\
\{J^{23}, J'^{23}\} \\
U
\end{pmatrix}
=
\begin{pmatrix}
1.0 \\
\{2.5, 3.0\} \\
\{0.017, 0.002\} \\
\{0.08, 0.06\} \\
\{0.03, 0.01\} \\
20.0
\end{pmatrix}
$$

Note, that smallness of J^{33} and J^{23} is compensated by the large value of $S = 5/2$. These parameters are chosen to be consistent with the data on LuFe_2O_4. For instance, in this material $V'/V \sim 1.2$ [122] and inter-layer exchanges are quite small, compared to the intra-layer ones [112]. However, we also checked that the general picture, presented below, survives slight variations in the above parameters (so the system is not fine-tuned).

4.4.1   Phase diagram

In the main panel of Fig. 4.2 we present the phase diagram of the system, featuring the electric polarization (4.8) as a function of temperature T. The inset in the same
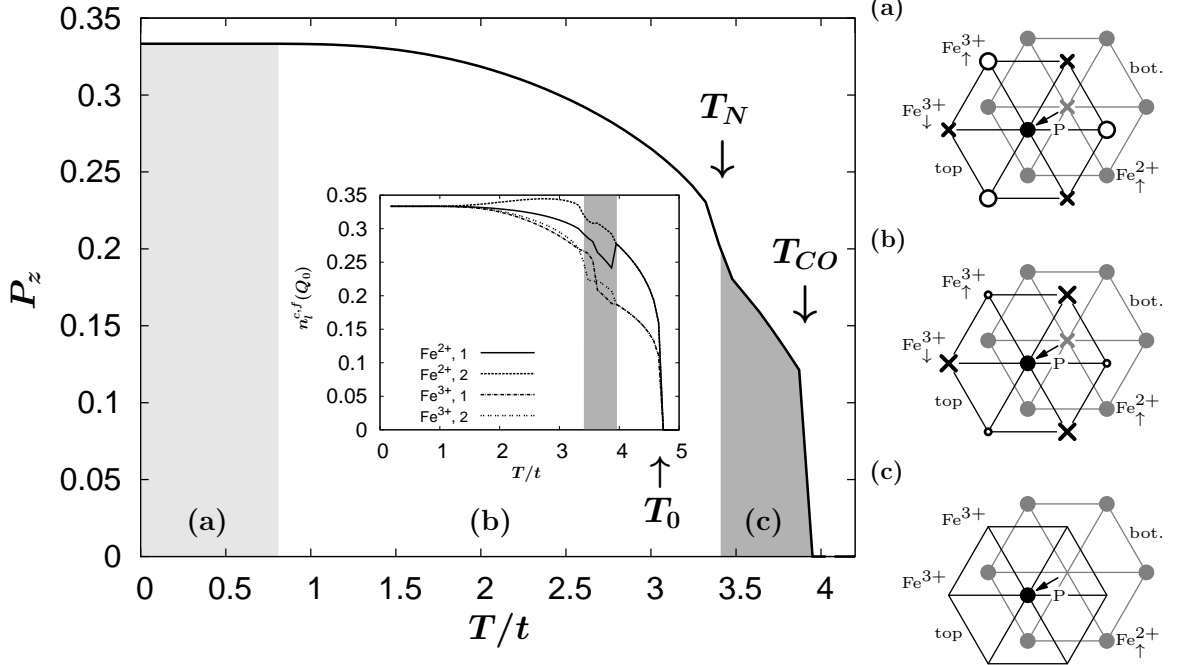
Figure 4.2: Polarization (4.8) as a function of temperature. Shaded regions mark different FiM phases: (a) Classical FiM with nominal values of spins at each site; (b) Modulated FiM with opposite, but unequal spins of Fe^{3+} ions in the honeycomb sublattice of the top layer; (c) Non-FiM phase. The corresponding spin patterns are shown schematically in the right panel, with the same notations as in Fig. 1.5(c). The size of crosses (circles) is proportional to magnitude of the local magnetization. Empty Fe^{3+}-sites in panel (c) indicate the absence of a definite spin direction. The inset shows T-dependence of the CDW order parameters (4.9). The phase transition at T_0 is accompanied by collapse of the ferromagnetism of Fe^{2+} spins.

figure shows T-dependence of the CDW order parameters (OP):

$$n_{l,\boldsymbol{Q}_0}^c = \frac{1}{N}\sum_{\boldsymbol{k},\zeta}\langle c_{l,\boldsymbol{k}\zeta}^\dagger c_{l,\boldsymbol{k}+\boldsymbol{Q}_0\zeta}\rangle, \quad n_{l,\boldsymbol{Q}_0}^f = \frac{1}{N}\sum_{\boldsymbol{k},\alpha}\langle f_{l,\boldsymbol{k}\alpha}^\dagger f_{l,\boldsymbol{k}+\boldsymbol{Q}_0\alpha}\rangle. \tag{4.9}$$

The state with a finite polarization is always characterized by a robust CDW order. On the contrary, due to the relative smallness of magnetic energy scales, in the same T-range the system exhibits several FiM instabilities, associated with ordering of the Fe^{3+} core spins. The corresponding phases are labelled as (a)–(c), and their magnetic structure is shown schematically in the right panel of the figure. The FiM state disappears at the Néel temperature, T_N. This transition is accompanied by a

pronounced feature in $P_z(T)$, which is qualitatively similar to the experimental curve, shown in Fig. 1.5(b). The physical origin of this behavior is easy to understand by looking at the structure of the effective Hamiltonian (4.4): absence of the Fe^{3+} spin order assists inter-layer hopping and removes correlation between Fe^{3+} and Fe^{2+} ions, due to the magnetic J^{23}-terms. Also, similar to experiments of Ref. [30, 110], the CDW disappears at a temperature T_0, which is somewhat higher than the charge-ordering temperature, T_{CO}, associated with the onset of P_z.

However, there exists an important discrepancy between experimental picture in $LuFe_2O_4$ and the results of our model calculations. Namely, the high-temperature *ferromagnetism* (FM) of the Fe^{2+} spins, which coexists and disappears (at $T = T_0$) simultaneously with the CDW state. We believe that this can be attributed to a combination of the Stoner effect (i.e. FM of a repulsive Fermi gas at the MF level) and the FM nature of the interactions J^{22}. Indeed, in our simulations we used the local on-cite repulsion U, which is the dominant energy scale in the problem. Since we describe an Fe^{2+} ion by a pseudospin-1/2 fermion variable, the system prefers to get rid of this scale by polarizing the c-type fermions. Thus, the above behavior appears to be an artifact of our MF approximation.

4.4.2   Magneto-electric coupling

Temperature dependence of the polarization, $P_z(T)$, discussed above, certainly implies a coupling between CDW and FiM orderings in the model (4.4). In order to make this statement quantitatively more precise, we computed the magneto-electric coefficient

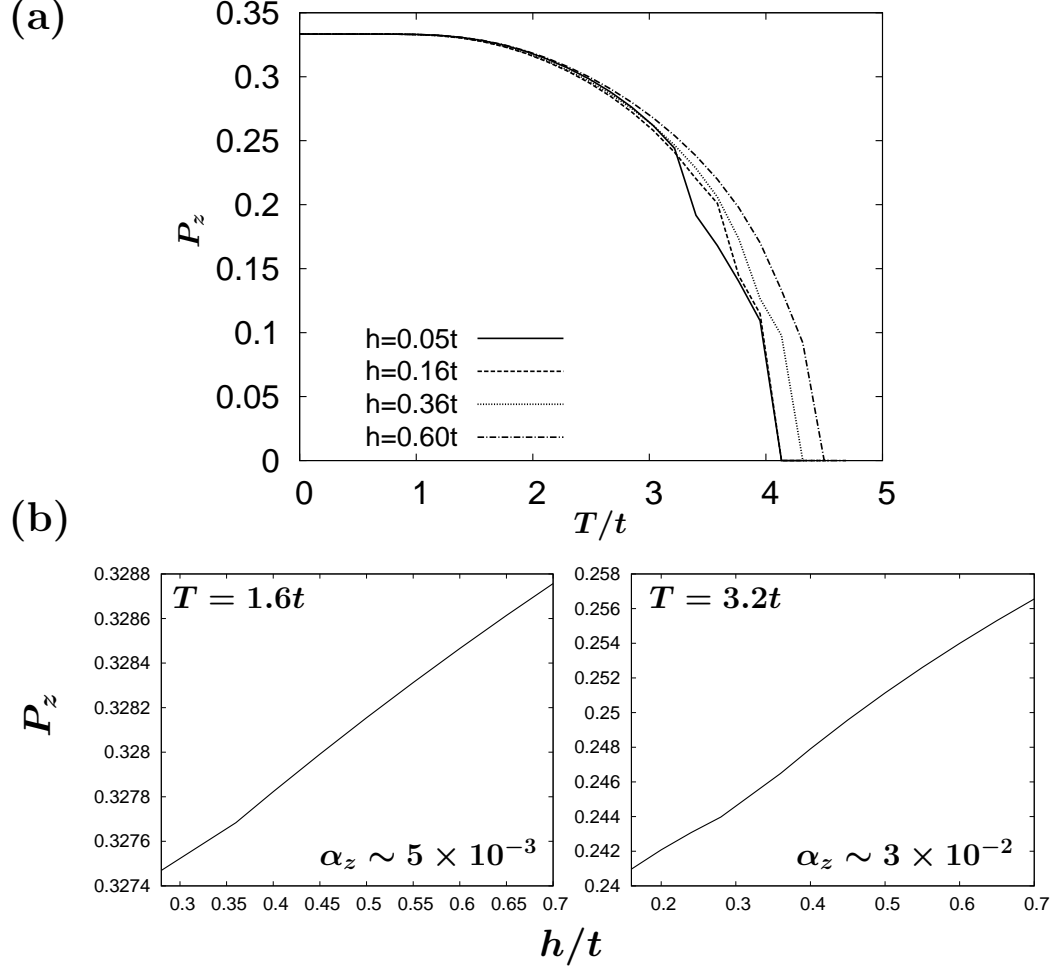$$\alpha_z = \frac{\partial P_z}{\partial h},$$

Figure 4.3: (a) Magnetic field dependence of the polarization. Notice the suppression of the anomaly around T_N in $P_z(T)$ with increasing h. (b) $P_z(h/t)$ for two values of T in the FiM and non-FiM regions, with corresponding magneto-electric coefficients.

i.e. the derivative of P_z with respect to an external Zeeman magnetic field[4], whose effect is described by the following correction to H_{eff} [122]:

$$\delta H_{\text{eff}} = -h \sum_{l,i} \big(S_{l,i}^z + s_{l,i}^z\big),$$

In particular, we would like to address the question regarding the most optimal temperature regime, which maximizes magneto-electric coupling.

---

[4]Because the state of the system is characterized by a non-zero CDW OP, the electron hopping is strongly suppressed and we can ignore orbital part of the magnetic field.

The results of this calculation are presented in Fig. 4.3. Since the polarization is caused by the charge ordering, the relevant energy scale is the NN Coulomb repulsion V. The magnetism is associated with much lower energies. This separation of scales leads to a weak dependence $P_z(h)$ at low temperatures. However, with increased temperature, the role of V is decreased. This fact allows for a more efficient manipulation of the polarization with an external magnetic field. For example, the ratio between two values of α_z, taken at $T_1 = 1.57t$ and $T_2 = 3.23t$, is $\alpha_z(T_2)/\alpha_z(T_1) \sim 10$. In other words, provided the model of Eq. (4.4) describes a real device, which employs the magneto-electric effect, one would like to operate this system in the temperature region (c) if Fig. 4.2. The possibility to manipulate the electric polarization with an applied magnetic field in the non-magnetic phase of $LuFe_2O_4$ (at room temperature) was demonstrated in [117].

4.5 Concluding remarks

Multiferroic materials with ferroelectricity due to charge-ordering are intriguing systems, demonstrating a subtle interplay between their electric and magnetic properties. Theoretical investigation of the related magneto-electic phenomena turns out to be quite challenging because of the importance of multiple bands in these systems and the large number of degrees of freedom, which need to be taken into account. Therefore, a combination of phenomenological and model methods is required, similar to the one employed in this chapter. Our approach relies on the separation of energy scales to identify degrees of freedom, relevant for the multiferroic behavior, and constructs a minimal effective model, which couples those degrees of freedom.

By studying such effective model, motivated by the multiferroic $LuFe_2O_4$, we demonstrated how frustration, associated with the triangular lattice geometry, non-local Coulomb repulsion, and spin-orbit interaction, first stabilize the commensurate

ferroelectric charge ordering and then a collinear ferrimagnetism, which coexists with ferroelectricity. In this multiferroic phase the double-exchange (Hund) mechanism provides a coupling between the corresponding order parameters.

This coupling manifests itself in a pronounced anomaly in the electric polarization P_z around Néel temperature. Our conclusions qualitatively agrees with pyroelectric current measurements in $LuFe_2O_4$, reported in [31]. The feedback on P_z, provided by the emerging magnetism around T_N, allows us manipulate the electric polarization with an applied magnetic field h. We have quantified this effect by computing the magneto-electric coefficient $\alpha_z = \partial P_z / \partial h$, which is strongly enhanced around T_N, compared to lower temperatures. The room-temperature magneto-electric effect in $LuFe_2O_4$ was experimentally demonstrated in [117].

Finally, we would like to make a remark regarding the necessary set of physical ingredients, which should be present, in order for a given system to exhibit a linear magneto-electric effect. From the discussion presented above, it follows that electron correlations and multiple bands are absolutely necessary to stabilize a multiferroic phase. However, in a recent work [126] it was argued that a linear magneto-electric coupling may be observed in non-correlated semiconductors ("topological insulators"), characterized by a very peculiar band structure[5]. While this conjecture was never confirmed experimentally, it remains an interesting direction for future investigation.

4.6 Appendix A: Low-energy effective processes

As we already mentioned, effective low-energy processes, described by the model (4.4), can be divided into two groups: (i) those involving a real charge transfer, and (ii) exchange interactions, associated with virtual electron transitions. Below we consider

---

[5]We note that the tight-binding model, defined on a TLL with nearest neighbor hoppings, describes a metal for all t and t'.
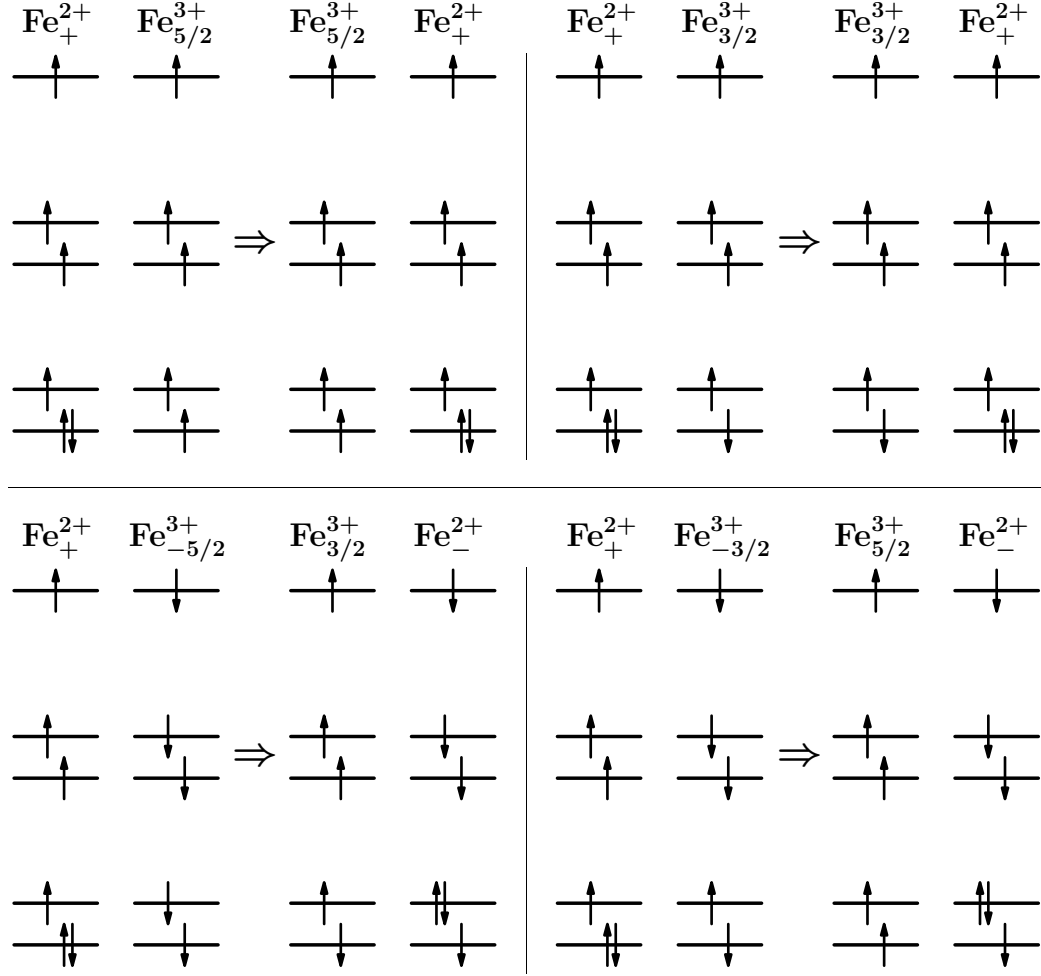
Figure 4.4: Possible channels for the electron transfer between Fe^{2+} and Fe^{3+} ions. Upper (Lower) panel shows pseudospin preserving (flipping) processes.

these groups separately.

(i) Matrix elements for charge transfer

The charge transfer occurs between a Fe^{2+} and a Fe^{3+} ion via hopping of the real electron between degenerate orbitals 1 and 2 (see Fig. 4.1(a)) of neighboring ions. Although the electron spin is conserved in the process, the pseudospin ζ, which describes the state of a Fe^{2+} ion, can flip. If we denote the corresponding matrix elements as $\tau_{\zeta'\zeta}$, then due to the time-reversal symmetry $\tau_{++} = \tau_{--}$ and $\tau_{+-} = \tau_{-+}$. A single-electron transfer can only change the spin projection of an ion by $\pm 1/2$. This
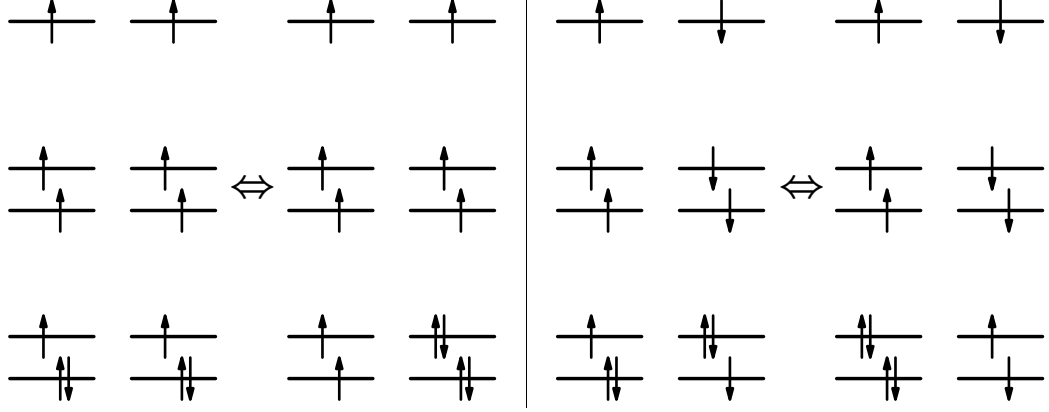
Figure 4.5: Virtual processes, leading to FM (left) and antiferromagnetic (right) exchange interactions between Fe^{2+} ions.

means that transitions involving $Fe^{3+}_{\pm 1/2}$ are prohibited[6]. The remaining channels are schematically shown in Fig. 4.4. The amplitudes of the processes, shown in this figure, are easily obtained using Eqs. (4.1) and (4.2):

- Pseudospin preserving transitions, $\tau_{++} = \tau_{--}$

$$\tau_{++}\big(5/2\big) = t, \quad \tau_{++}\big(3/2\big) = -t/5,$$

  where t is the hopping amplitude for the real electron and numbers in parentheses denote spin projections of the Fe^{3+} ion.

- Pseudospin flipping transitions, $\tau_{+-} = \tau_{-+}$

$$\tau_{+-}\big(-5/2\big) = \tau_{+-}\big(-3/2\big) = -t/\sqrt{5}.$$
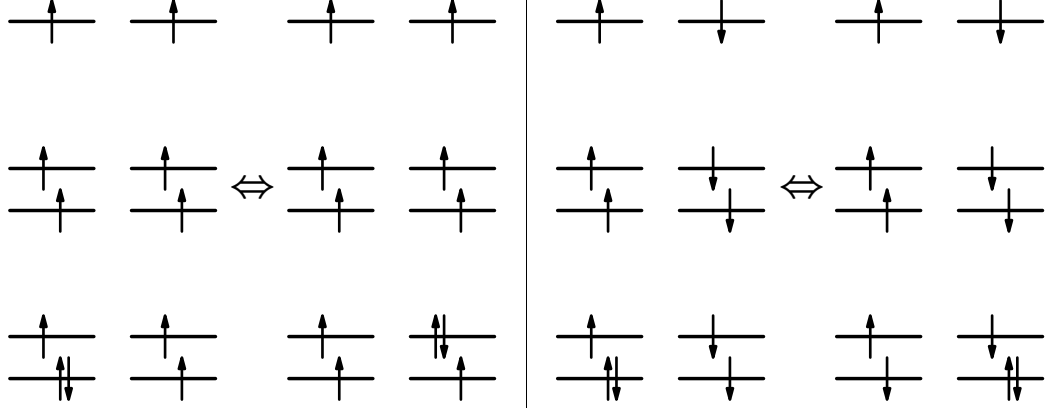
  Notations are the same as above.

Figure 4.6: Virtual processes, leading to FM (left) and antiferromagnetic (right) exchange interactions between Fe^{2+} and Fe^{3+} ions.

(ii) Exchange interactions

There are three types of NN exchange couplings: Fe^{2+}-Fe^{2+}, Fe^{3+}-Fe^{3+} and Fe^{2+}-Fe^{3+}, which appear because of the virtual electron hopping between *all* (i.e. not just lowest two) orbitals of the two ions. In general, all couplings have antiferro- and ferro-magnetic contributions. In Figs. 4.5 and 4.6 we show an example of each of these channels.

The "first-principle" derivation of $J_{ll'}^{nm}$ is quite tedious and requires the use of a *pd*-type model, which includes not only iron ions, but also oxygen $2p$ orbitals. A calculation along these lines was presented in [122].

Since here we are interested in the physical picture, corresponding to an interplay between electric and magnetic orders, we prefer to employ a simpler approach to obtaining $J_{ll'}^{nm}$. Namely, we use the low-temperature spin structures, which are calculated by fitting experimental data in $LuFe_2O_4$ [112, 113], in order to extract signs of $J_{ll'}^{nm}$, and treat their magnitudes as free parameters. In this way we conclude

---

[6]For instance, if an electron hops from Fe_+^{2+}, it leaves behind a Fe^{3+} core with $S^z = +5/2$ or $+3/2$. These states have zero overlap with $\left| Fe^{3+}_{\pm 1/2} \right\rangle$.

that: $J_{ll'}^{33}$ and $J_{ll'}^{23}$ are antiferromagnetic, and $J_{ll'}^{22}$ is FM, i.e.

$$J_{ll'}^{33}, \ J_{ll'}^{23} > 0; \quad J_{ll'}^{22} < 0.$$

This conclusion is also consistent with calculations of Naka *et al.* [122]. In the effective Hamiltonian (4.4), we have explicitly separated the negative sign from $J_{ll'}^{22}$.

Chapter 5

Conclusions

The interplay between lattice frustration and competing interactions leads to complex behavior, rich phase diagrams and a variety of physical phenomena even in relatively simple models. Studying these phenomena not only enhances our basic physics understanding, but also enables us to design systems and materials with novel properties. These studies, however, often face substantial theoretical challenges, whose origin is precisely the above complexity. In the present work we attempted to address some of those challenges.

In Chap. 2 we introduced a non-perturbative variational technique, the hierarchical mean-field method, which was subsequently applied to several models of frustrated quantum magnets. By using the exact diagonalization of finite clusters, the HMF approach treats different competing phases on an equal footing, thus providing an *unbiased* framework for investigating strongly interacting systems. As a consequence, one can use a single variational ground state wavefunction to describe the entire phase diagram of a system of interest. In Secs. 2.2 and 2.4 we used the HMF method to obtain zero-temperature phase diagrams of the J_1-J_2 and J-Q models. Both of these systems exhibit a quantum paramagnetic phase, whose structure has been under intense investigation in recent years. In our studies we unveiled the cor-

related plaquette nature of non-magnetic states in both models, therefore definitively ruling out possible dimer orderings, proposed in the previous works. In Sec. 2.3 we revisited the problem of magnetization plateaux in the Shastry-Sutherland model. These plateaux were observed in high magnetic field experiments in $SrCu_2(BO_3)_2$ and stimulated a lot of theoretical debates. We were able to derive a set of necessary stability conditions for a given plateau, which define a hierarchy of variational plateau wavefunctions.

Frustration and long-range order are usually thought of as mutually exclusive physical phenomena. Nevertheless, in some cases frustration can be employed to actually stabilize an ordered state. In Chap. 3 we illustrate this mechanism by studying superconductivity in the strongly repulsive Hubbard model on a specially "engineered" lattice, made of weakly-coupled clusters with frustrating second neighbor hoppings. Fine-tuning of these hopping amplitudes results in a ground-state degeneracy, which effectively eliminates the effect of fermion repulsion and allows magnetic fluctuations to establish a robust superconducting state. We also argued that this peculiar phenomenon can be observed in experiments involving cold atoms in optical lattices.

The key role of frustration in stabilizing an ordered state with fascinating properties was further demonstrated in Chap. 4, where we discussed magneto-electric phenomena in frustrated charge-ordered multiferroics. Motivated by experiments in $LuFe_2O_4$, we presented a theory of multiferroic behavior and magneto-electric effect, driven by the order-from-disorder and double exchange mechanisms. We explicitly showed how the coupling between electric and magnetic orders provides a means to manipulate, e.g. electric properties with an external magnetic field.

Our work will hopefully help in addressing an important question regarding the *systematic* manipulation of lattice frustration and strong correlations in a guided design of novel materials with highly non-trivial properties.

Bibliography

[1] J. Hubbard, Proc. Roy. Soc. **A276**, 238 (1963).

[2] J. Hubbard, Proc. Roy. Soc. **A277**, 237 (1964).

[3] J. Hubbard, Proc. Roy. Soc. **A281**, 401 (1964).

[4] L. D. Landau and E. M. Lifshitz, *Quantum Mechanics* (Pergamon Press, Oxford, 1977).

[5] J. M. Ziman, *Principles of the theory of solids* (Cambridge University Press, New York, 1972).

[6] N. Nagaosa, *Quantum field theory in strongly correlated electronic systems* (Springer, Berlin, 1999).

[7] J. Gonzalez *et al.*, *Quantum electron liquids and high-T_c superconductivity*, Chapters 6 and 7 (Springer, Berlin, 1995).

[8] U. Schneider *et al.*, Science **322**, 1520 (2008).

[9] N. Trivedi and D. M. Ceperley, Phys. Rev. **B40**, 2737 (1989).

[10] L. N. Bulaevskii *et al.*, Phys. Rev. **B78**, 024402 (2008).

[11] J. E. Hirsch, Phys. Rev. Lett. 59, 228 (1987).

[12] S. Trugman, Phys. Rev. **B37**, 1597 (1988).

[13] G. Misguich and C. Lhuillier in *Frustrated Spin Systems*, edited by H. T. Diep (World Scientific, Singapore, 2004).

[14] J. M. Luttunger and L. Tisza, Phys. Rev. **70**, 954 (1946).

[15] E. F. Shender, Sov. Phys. JETP **56**, 178 (1982).

[16] C. L. Henley, Phys. Rev. Lett. **62**, 2056 (1989).

[17] A. Moreo *et al.*, Phys. Rev. **B42**, 6283 (1990).

[18] P. Thalmeier *et al.*, Phys. Rev. **B77**, 104441 (2008).

[19] L. D. Landau, E. M. Lifshitz and L. P. Pitaevskii, *Statistical Physics*, part 2 (Butterworth-Heinemann, New-York, 1999).

[20] P. Chandra and B. Doucot, Phys. Rev. **B38**, 9335 (1988).

[21] L. N. Cooper, Phys. Rev. **104**, 1189 (1956).

[22] J. Bardeen, L. N. Cooper, and J. R. Schrieffer, Phys. Rev. **108**, 1175 (1957).

[23] W. Kohn and J. M. Luttinger, Phys. Rev. Lett. **15**, 524 (1965).

[24] V. V. Mineev and K. V. Samokhin, *Introduction to Unconventional Superconductivity* (Gordon and Breach, New York, 1999).

[25] P. W. Anderson and P. Morel, Phys. Rev. **123**, 1911 (1961).

[26] S. Raghu, S. A. Kivelson, and D. J. Scalapino, Phys. Rev. **B81**, 224505 (2010).

[27] D. I. Khomskii, J. Magn. Magn. Mater. **306**, 1 (2006).

[28] J. van den Brink and D. I. Khomskii, J. Phys.: Cond. Mat. **20**, 434217 (2008).

[29] D. I. Khomskii, Physics **2**, 20 (2009).

[30] Y. Yamada *et al.*, Phys. Rev. **B62**, 12167 (2000).

[31] N. Ikeda *et al.*, Nature **436**, 1136 (2005).

[32] L. D. Landau, L. P. Pitaevskii and E. M. Lifshitz, *Electrodynamics of Continuous Media*, (Butterworth-Heinemann, New-York, 1999).

[33] G. Ortiz and C. D. Batista, Phys. Rev. **B67**, 134301 (2003); in *Condensed Matter Theories*, vol. 18, M. de Llano et al. ed. (Nova Science Publishers, 2003).

[34] T. Maier *et al.*, Rev. Mod. Phys. **77**, 1027 (2005).

[35] L. Isaev, G. Ortiz and J. Dukelsky, Phys. Rev. **B79**, 024409 (2009).

[36] L. Isaev, G. Ortiz and J. Dukelsky, Phys. Rev. Lett. **103**, 177201 (2009).

[37] L. Isaev, G. Ortiz and J. Dukelsky, J. Phys.: Condens. Matter **22**, 016006 (2010).

[38] L. Isaev, G. Ortiz and J. Dukelsky, Phys. Rev. **B82**, 136401 (2010).

[39] L. Capriotti and S. Sorella, Phys. Rev. Lett. **84**, 3173 (2000).

[40] L. Capriotti *et al.*, Phys. Rev. Lett. **87**, 097201 (2001).

[41] M. S. L. du Croo de Jongh *et al.*, Phys. Rev. **B62**, 14844 (2000).

[42] R. Darradi *et al.*, Phys. Rev. **B78**, 214415 (2008).

[43] R. R. P. Singh *et al.*, Phys. Rev. **B60**, 7278 (1999).

[44] K. Takano *et al.*, Phys. Rev. Lett. **91**, 197202 (2003).

[45] V. Kotov *et al.*, Phys. Rev. **B60**, 14613 (1999).

[46] V. Lante and A. Parola, Phys. Rev. **B73**, 094427 (2006).

[47] N. Read and S. Sachdev, Phys. Rev. Lett. **66**, 1773 (1991).

[48] T. Senthil *et al.*, Phys. Rev. **B70**, 144407 (2004).

[49] L. D. Landau, E. M. Lifshitz and L. P. Pitaevskii, *Statistical Physics*, part 1 (Butterworth-Heinemann, New-York, 1999).

[50] E. Manousakis, Rev. Mod. Phys. **63**, 1 (1991).

[51] J. Sirker *et al.*, Phys. Rev. **B73**, 184420 (2006).

[52] A. W. Sandvik, Phys. Rev. Lett. **98**, 227202 (2007).

[53] C. D. Batista and S. A. Trugman, Phys. Rev. Lett. **93**, 217202 (2004).

[54] M. van den Bossche *et al.*, Eur. Phys. J. **B17**, 367 (2000).

[55] E. Altman and A. Auerbach, Phys. Rev. **B65**, 104508 (2002).

[56] A. R. Edmonds, *Angular Momentum in Quantum Mechanics* (Princeton University Press, Princeton, 1957).

[57] A. Auerbach, *Interacting Electrons and Quantum Magnetism* (Springer-Verlag, New York, 1994).

[58] N. Trivedi and D. M. Ceperley, Phys. Rev. **B40**, 2737 (1989).

[59] A. L. Fetter, Ann. Phys. **70**, 67 (1972).

[60] C. K. Majumdar and D. K. Ghosh, J. Math. Phys. **10**, 1388 (1969).

[61] K. Okamoto and K. Nomura, Phys. Lett. **A169**, 433 (1992).

[62] E. H. Lieb, T. D. Schultz and D. C. Mattis, Ann. Phys. **16**, 407 (1961).

[63] M. B. Hastings, Phys. Rev. **B69**, 104431 (2004).

[64] M. E. Fisher, Phys. Rev. **124**, 1664 (1961).

[65] J. Richter, J. Schulenburg and A. Honecker in *Quantum Magnetism*, U. Shollwöck, J. Richter, F. J. J. Farnel and R. F. Bishop eds. (Springer-Verlag, Berlin 2004).

[66] H. Kageyama *et al.*, Phys. Rev. Lett. **82**, 3168 (1999).

[67] K. Onizuka *et al.*, J. Phys. Soc. Jpn. **69**, 1016 (2000).

[68] K. Kodama *et al.*, Science **298**, 395 (2002).

[69] M. Takigawa *et al.*, J. Phys. Conf. Ser. **51**, 23 (2006).

[70] M. Takigawa *et al.*, Phys. Rev. Lett. **101**, 037202 (2008).

[71] S. E. Sebastian *et al.*, PNAS **105**, 20157 (2008).

[72] B. S. Shastry and B. Sutherland, Physica **108B**, 1069 (1981).

[73] S. Miyahara and K. Ueda, J. Phys.: Cond. Mat. **15**, R327 (2003).

[74] G. Misguich, T. Jolicoeur, and S. M. Girvin, Phys. Rev. Lett. **87**, 097203 (2001).

[75] S. Miyahara and K. Ueda, Phys. Rev. Lett. **82**, 3701 (1999); Phys. Rev. **B61**, 3417 (2000). T. Momoi and K. Totsuka, Phys. Rev. **B62**, 15067 (2000).

[76] J. Dorier, K. P. Schmidt, and F. Mila, Phys. Rev. Lett. **101**, 250402 (2008).

[77] A. Abendschein and S. Capponi, Phys. Rev. Lett. **101**, 227201 (2008).

[78] R. G. Melko and R. K. Kaul, Phys. Rev. Lett. **100**, 017203 (2008).

[79] R. K. Kaul and R. G. Melko, Phys. Rev. **B78**, 014417 (2008)

[80] S. Sachdev, Nature Physics **4**, 173 (2008).

[81] A. W. Sandvik and Jie Lou, private communication.

[82] F. J. Jiang, M. Nyfeler, S. Chandrasekharan and U. J. Wiese, J. Stat. Mech. (2008) P022009.

[83] J. P. Blaizot and G. Ripka, *Quantum theory of finite systems* (The MIT Press, Cambridge, 1986).

[84] L. Isaev, G. Ortiz and C. D. Batista, Phys. Rev. Lett. **105**, 187002 (2010).

[85] P. Monthoux, D. Pines, and G. G. Lonzarich, Nature **450**, 1177 (2007).

[86] J. M. Tranquada *et al.*, Nature **375**, 561 (1995).

[87] T. Valla *et al.*, Science **314**, 1914 (2006).

[88] W. D. Wise *et al.*, Nature Phys. **5**, 213 (2009).

[89] E. Dagotto, Science **309**, 257 (2005).

[90] J. Eroles *et al.*, Europhys. Lett. **50**, 540 (2000).

[91] S. A. Kivelson and E. Fradkin in *Treatise of High Temperature Sureconductivity*, J. R. Schrieffer and J. Brooks eds. (Springer-Verlag, Berlin, 2007).

[92] W. F. Tsai *et al.*, Phys. Rev. **B77**, 214502 (2008).

[93] H. Yao, W. F. Tsai, and S. A. Kivelson, Phys. Rev. **B76**, 161104 (2007).

[94] A. F. Barabanov, L. A. Maksimov, and A. V. Mikheyenkov, J. Phys.: Cond. Matter **1**, 10143 (1989).

[95] G. B. Martins *et al.*, Phys. Rev. **B64**, 180513 (2001).

[96] R. Jördens *et al.*, Nature **455**, 204 (2008).

[97] A. M. Rey *et al.*, Europhys. Lett. **87**, 60001 (2009).

[98] G. L. Bir and G. E. Pikus, *Symmetry and Strain-Induced Effects in Semiconductors*, Wiley, New York, 1974.

[99] C. D. Batista, G. Ortiz, and J. E. Gubernatis, Phys. Rev. **B65**, 180402 (2002).

[100] A. Fledderjohann *et al.*, Eur. Phys. J. **B43**, 471 (2005).

[101] C. D. Batista and G. Ortiz, Adv. in Phys. **53**, 1 (2004).

[102] G. G. Batrouni and R. T. Scalettar, Phys. Rev. Lett. **84**, 1599 (2000).

[103] L. Jiang *et al.*, Phys. Rev. A **79**, 022309 (2009).

[104] W. F. Tsai and S. A. Kivelson, Phys. Rev. **B73**, 214510 (2006).

[105] Y. Nagaoka, Phys. Rev. **147**, 392 (1966).

[106] E. Altman *et al.*, New J. Phys. **5**, 113 (2003).

[107] N. Shannon and A. V. Chubukov, J. Phys.: Cond. Mat. **14**, L235 (2002).

[108] S. Ishihara, J. Phys. Soc. Jpn. **79**, 011010 (2010).

[109] Y. Zhang *et al.*, Phys. Rev. Lett. **98**, 247602 (2007).

[110] M. Angst *et al.*, Phys. Rev. Lett. **101**, 227601 (2008).

[111] K. Kuepper *et al.*, Phys. rev. **B80**, 220409(R) (2009).

[112] K. T. Ko *et al.*, Phys. Rev. Lett. **103**, 207202 (2009).

[113] A. D. Christianson *et al.*, Phys. Rev. Lett. **100**, 107601 (2008).

[114] M. H. Phan *et al.*, J. Appl. Phys. **105**, 07E308 (2008).

[115] M. A. Subramanian *et al.*, Adv. Mater. **18**, 1737 (2006).

[116] C. Li *et al.*, Phys. Rev. **B79**, 172412 (2009).

[117] J. Wen *et al.*, Phys. Rev. **B80**, 020403(R) (2009).

[118] H. J. Xiang and M. H. Whangbo, Phys. Rev. Lett. **98**, 246403 (2007).

[119] H. J. Xiang *et al.*, Phys. Rev. **B80**, 132408 (2009).

[120] A. B. Harris and T. Yildirim, Phys. Rev. **B81**, 134417 (2010).

[121] A. Nagano *et al.*, Phys. Rev. Lett. **99**, 217202 (2007).

[122] M. Naka *et al.*, Phys. Rev. **B77**, 224441 (2008).

[123] M. Singh, C. S. Wang and J. Callaway, Phys. Rev. **B11**, 287 (1975).

[124] E. Müller-Hartmann and E. Dagotto, Phys. Rev. **B54**, R6819 (1996).

[125] G. Ortiz and R. M. Martin, Phys. Rev. **B49**, 14202 (1994).

[126] A. M. Essin, J. E. Moore, and D. Vanderbilt, Phys. Rev. Lett. **102**, 146805 (2009).

Curriculum Vita
Leonid Isaev

Education

- Indiana University, Bloomington, IN
  Ph. D. in Condensed Matter Physics; Advisor: Gerardo Ortiz
  Jan. 2006 – July 2011; GPA 4.0/4.0

- Ball State University, Muncie, IN
  M. S. in Physics; Advisors: Arkady Satanin and Yong Joe
  Aug. 2004 – Nov. 2005; GPA 3.86/4.00

- Nizhny Novgorod State University, Nizhny Novgorod, Russia
  B. S. in Theoretical Physics; Advisor: Alexander Protogenov
  Sep. 1999 – Jun. 2003; GPA 4.0/4.0

Professional experience

Long term

- Postdoctoral research associate (July 2011 – present)
  Department of Physics and Astronomy
  Louisiana State University, Baton Rouge, LA

- Research Assistant (Jan. 2006 – July 2011)
  Indiana University, Bloomington, IN

- Research Assistant (Aug. 2004 – Nov. 2005)
  Ball State University, Muncie, IN

- Research fellow (Sep. 2003 – May. 2004)
  Institute of Applied Physics of the Russian Academy of Sciences
  Nizhny Novgorod, Russia

Short term

- Student associate (summer 2007 and 2010)
  Center for nonlinear studies, LANL

- Center for nonlinear studies, LANL (Oct. – Nov. 2009)

Awards

- Outstanding graduate student theoretical research award (2009)
  Indiana University Bloomignton

- Young scientists support award (2004)
  "Dynasty" fund and Russian Academy of Sciences

Research interests

My current research focuses on understanding novel physical properties of strongly correlated quantum systems, including high-T_c superconductors, heavy fermion materials, frustrated magnets, multiferroics and ultracold atomic gases. The state of these systems and their response to external probes are determined by an interplay of quantum orders, such as superconductivity, Bose-Einstein condensation and various multiferroic orders. This circumstance makes it virtually impossible to study the complex phenomena, exhibited by such systems using conventional field-theoretical methods. Instead, new frameworks and techniques have to be developed and applied.

Another branch of my research focuses on the study of spectral and transport properties of nanoscale low dimensional systems, such as quantum dots and thin films, particularly on the effect of surface properties on the observable characteristics of these systems.

Computer skills

- Fortran, C, Unix shells, LaTeX

- Linux system administration

References

Available upon request

Publications

1. L. Isaev, Y. H. Moon and G. Ortiz, "Bulk-boundary correspondence in three dimensional topological insulators", arXiv:1103.0025, submitted to PRB

2. L. Isaev, G. Ortiz and C. D. Batista, "Superconductivity in strongly repulsive fermions: the role of the kinetic-energy frustration", Phys. Rev. Lett. **105**, 187002 (2010)

3. L. Isaev, G. Ortiz and J. Dukelsky, "Comment on "Quantum phase transition in the four-spin exchange antiferromagnet"", Phys. Rev. **B82**, 136401 (2010)

4. L. Isaev, G. Ortiz and J. Dukelsky, "Phase diagram of the Heisenberg antiferromagnet with four-spin interactions", J. Phys.: Condens. Matter **22**, 016006 (2010)

5. L. Isaev, G. Ortiz and J. Dukelsky, "Local physics of magnetization plateaux in the Shastry-Sutherland model", Phys. Rev. Lett. **103**, 177201 (2009)

6. L. Isaev, G. Ortiz and J. Dukelsky, "Hierarchical mean-field approach to the J_1-J_2 Heisenberg model on a square lattice", Phys. Rev. **B79**, 024409 (2009)

7. L. Isaev, A. M. Satanin and Y. S. Joe, "Optical properties of quantum dots produced from inverted-gap semiconductors", Semicond. Sci. Technol. **22**, 471 (2007)

8. Y. S. Joe, L. Isaev and A. M. Satanin, "Spin-splitting of electron subbands in semiconducting films with a variable band gap", Phys. Lett. **A369**, 140 (2007)

9. L. S. Isaev and A. P. Protogenov, "Charge-density distributions in doped antiferromagnetic insulators", Phys. Rev. **B69**, 012401 (2004)

10. L. S. Isaev and A. P. Protogenov, "Structures of order parameters in inhomogeneous phase states of strongly correlated systems", JETP **96**, 1140 (2003)

11. L. S. Isaev and A. P. Protogenov, "Structure of Multi-Meron Knot Action", in *Proceedings of the Workshop "Nonlinear Physics: Theory and Experiment II"*, M. J. Ablowitz *et al.* eds. (World Scientific, Singapore, 2003)